UNIVERSITAT POLITÈCNICA DE CATALUNYA BARCELONATECH

Chemical design and validation of Ca2+-releasing platforms to promote vascularization in tissue regeneration

Joan Martí Muñoz

Chemical design and validation of Ca^{2+}-releasing platforms to promote vascularization in tissue regeneration

Joan Martí Muñoz (PhD Candidate)

Dr. Oscar Castaño Linares (Thesis Director)

Biomaterials for Regenerative Therapies (Dr. Elisabeth Engel research group)

Institute for Bioengineering of Catalonia (IBEC)

Acknowledgments

This thesis would not have been the same without the contribution of many people and organizations, who I will try to name in this section. First, I would like to thank Dr. Oscar Castaño for his very kind supervision and guidance through all this thesis, as well as Dr. Elisabeth Engel and Prof. Josep A. Planell for giving me the opportunity to start this PhD in their research group. I also wanted to thank Dr. Soledad Pérez-Amodio for her help and guidance through all the biological experiments. I have a sincere gratitude for the current and former researchers who I had the pleasure to work with; Dr. Claudia Navarro, Irene Cano, Jesús Ordoño, Gerard Rubí, Sergi Rey, Dr. Miguel Ángel Mateos, Dr. Xavier Puñet, Dr. Aitor Sánchez, Dr. Riccardo Levato, Dr. Nadège Sachot, Dr. Arlyng González, Dr. Tiziano Serra, as well as all the master and graduate students who lead us a hand with our experiments, without all of you this thesis should not have been possible. Regarding the financial support I thank the Spanish Ministry (MINECO, MAT2011-29778-C02-01), the Centro de Investigación Biomédica en Red (CIBER-BBN), the European Commission (NANGIOFRAC; PI11/03030), the Serra Hunter program and Obra Social La Caixa. I also take this opportunity to thank Prof. Stephen E. Rankin for hosting me in his research group in the Chemical and Materials Engineering Department at the University of Kentucky (UKY) during my international PhD stay in the USA in the summer of 2015, as well as Mr. John W. Layton from the Chemistry Department at the UKY for his support in the NMR experiments. I also thank Dr. Elena Xuriguera, Dr. Joan Pous and Dr. Lídia Bardia form the Materials Sciences and Physical Chemistry Department at the University of Barcelona (UB), the Structural & Computational Biology Unit at the Institute for Research in Biomedicine (IRB-Barcelona) and the Advance Digital Microscopy Department at the IRB-Barcelona respectively for their respective help in the ATR-FTIR spectra, DLS & Z-potential measurements and the development of an ImageJ macro to quantify the blood vessels in the CAM model. I also thank Dr. Romén Rodríguez

from the Nanobioengineering group at IBEC for allowing me a space to write this thesis. To finish with the professional contributions, I would like to express my most sincere respect for all the animals that had to be inevitably sacrificed for the development of this thesis. Apart from the professional contributions, there was a very important emotional support shared with most of the already mentioned names but also including some other people who I would like to cite here. These people can be classified in three main groups; my neighborhood crew, the friends that I meet during my university degree of Chemistry and the people who I have the pleasure to practice Wing Chun weekly, thanks to all of you for giving me such wonderful breaks from time to time. Finally, I would like to give my most sincere gratitude to my family, specially to my parents who apart from giving me birth, have invested endless efforts and money in providing me an education without which I would not be where I am. This thesis is for all of you.

To my unborn niece, who we all are waiting for your arrival.

“The noblest pleasure is the joy of understanding” Leonardo da Vinci 1452-1519

An insufficient vascularization of the wound site is often the cause of failure in tissue regeneration. Although the use of cell therapy or growth factors has introduced promising results, they are risky, expensive and difficult to store. Synthetic biomaterials offer an alternative, reducing these limitations but at the same time decreasing also the positive effects. Among synthetic materials, degradable calcium phosphates have demonstrated an efficient bioactivity. Their partial dissolution towards the surrounding tissue induces several positive responses including cell migration, proliferation and even osteogenic differentiation. What is not so well understood is their angiogenic (formation of blood vessels from pre-existing ones) potential. Recent findings in our group indicates that their Ca^{2+} release is involved in the cell synthesis of angiogenic factors such as the VEGF. Based on this finding, in this thesis, we synthesized binary (P_2O_5-CaO) calcium phosphate glass (CPg) degradable nanoparticles by the sol-gel method and tested and validated their angiogenic potential *in vitro* and *in vivo*. Interestingly, this is the first time that binary (P_2O_5-CaO) CPg nanoparticles have been synthesized by the sol-gel method. We used ethylphosphate and calcium 2-methoxyethoxide as sol-gel precursors, and we catalyzed the precipitation of the particles using $NH_{3(aq)}$ in an ethanolic medium. Nuclear magnetic resonance supplemented with other characterization techniques, showed that the particles were a mixture of highly soluble amorphous calcium monoethylphosphate with the formation of portlandite or $NH_4H_2PO_4$ for an excess or the absence of Ca respectively. After a thermal treatment at 200 or 350 ºC, the highly soluble organic particles were converted into more stable (but still degradable) inorganic amorphous calcium trimetaphosphate (ACTMP), pyrophosphate (ACPP), orthophosphate (ACP) and calcite, as the Ca content of the particles increased respectively. We controlled the ion release of the particles under physiological conditions by modifying their Ca/P ratio and applying this moderately low thermal treatment. The CPg nanoparticles were combined with electrospun polylactic acid nanofibers in order to develop implantable scaffolds. The Ca^{2+} releasing scaffolds showed promising results in angiogenesis, including a similar blood vessel formation than significant VEGF doses in the chick chorioallantioc

membrane model. The scaffolds also induced a stronger osteogenic differentiation, and a significant skin ulcer reduction in diabetic and obese mice, that validates their use not only for bone but also for the healing of highly vascularized softer tissues such as skin. Concluding, we demonstrated that the use of synthetic Ca^{2+} releasing scaffolds free from biological molecules or drugs, offers a cost-effective alternative for the regeneration of highly vascularized tissues.

The authors declare no conflict of interests.

Index

Glossary

A

ACP: Amorphous calcium orthophosphate

ACPP: Amorphous calcium pyrophosphate

ACTM: Amorphous calcium trimetaphosphate

ATR-FTIR: Attenuated total reflectance infrared spectroscopy

C

C: Carbon

CAM: Chick chorioallantoic membrane

CD31: Cluster of differentiation 31

CMEO: Calcium 2-methoxyethoxide

CMEP: Calcium monoethylphosphate

CP: Calcium phosphates

CPc: Calcium phosphate ceramics

CPg: Calcium phosphate glasses

CaSR: Calcium-sensing receptor

D

D_2O: Deuterium oxide (heavy water)

DEP: Diethylphosphate

DLS: Dynamic Light Scattering

DMEM: Dulbecco's modified essential medium

DSC: Differential scanning calorimetry

E

EA: Elemental analysis

ECM: Extracellular matrix**/**Extracted culture medium

EDS: Energy dispersive X-ray spectroscopy

EPCs: Endothelial progenitor cells

ERM: Extracted regular medium

ESI-MS: Electrospray ionization mass spectrometry

F

FBS: Fetal bovine serum

FE-SEM: Field emission scanning electron microscopy

H

HA: Hydroxyapatite

hDFs: Human dermal fibroblasts

HEPES: 4-(2-hydroxyethyl)-1-piperazineethanesulfonic acid

hMSCs: Human mesenchymal stem cells

^{1}H NMR: Proton nuclear magnetic resonance

HUVECs: Human umbilical vein endothelial cells

M

MEOH: 2-methoxyethanol

MEM: Minimum essential medium

MEP: Monoethylphosphate

MSCs: Mesenchymal stem cells

N

NC: Negative control

O

OM: Osteogenic medium

P

PBS: Phosphate buffered saline solution

Pi: Inorganic phosphate

PLA: Polylactic acid

^{31}P MAS NMR: Phosphorus magnetic angle spinning nuclear magnetic resonance

^{31}P NMR: Phosphorus nuclear magnetic resonance

Q

Q^n: Condensed phosphate units

R

RM: Regular medium

RT: Room temperature

S

SEM: Standard error of the mean

T

TCC: Total carbon content

TCP: Tissue culture plate

TEP: Triethylphosphate

Tg: Glass transition temperature

TOC: Total organic carbon

V

VEGF: Vascular endothelial growth factor

X

XRD: X-ray diffraction

Objectives

The aim of this thesis was to develop, characterize and study biodegradable and biocompatible synthetic scaffolds with controllable Ca^{2+} release to stimulate the vascularization and the healing of hard-to-heal wounds. This objective has been based on previous studies performed by a former PhD student of the group (Dr. Aitor Aguirre) that demonstrated that specific physiological Ca^{2+} concentrations played a crucial role in angiogenesis (i.e. formation of blood vessels from pre-existing ones) [1]. Since a poor vascularization is often the main drawback in the regeneration of chronic and hard-to-heal wounds, a Ca^{2+}-releasing strategy has been adopted to develop synthetic scaffolds to overcome this problem. The trend was to avoid biological components (e.g. growth factors, active proteins, drugs) that hinder their translation to the market due to money-cost, unpredictable responses and difficult storage. The development of the scaffolds was based on previous studies performed by another former PhD student (Dr. Nadège Sachot), who worked in the development of composite materials for the healing of critical bone fractures and angiogenesis [2,3]. Since I did not develop some of the scaffold manufacturing protocols (e.g. electrospinning), their parameters are not widely discussed in the materials and methods sections.

Following, I will describe in more detail the specific objectives of this thesis;

- Develop and characterize by the sol-gel method Ca^{2+} releasing nanoparticles with controlled degradability, containing only known metabolizable components, and susceptible to be embedded into polymeric nanofibrous scaffolds.

- Study by nuclear magnetic resonance spectroscopy and other complementary techniques the chemical structure of the sol-gel precursors, the sol-gel reaction and the synthesized nanoparticles. Correlate the chemical structure of the particles with their composition and degradability.

- Developed and characterize implantable scaffolds by the electrospinning technique, using polylactic acid and containing different amounts of the synthesized nanoparticles to release different Ca^{2+} concentrations in physiological conditions.

- Evaluate the *in vitro* angiogenic potential of the developed scaffolds and their potential application in bone regeneration. Correlate the Ca^{2+} released with the induced angiogenesis.

- Evaluate the *in vitro* and *in vivo* applicability of the developed scaffolds for the treatment of chronic skin wounds and correlate the results with current clinic treatments.

[1] A. Aguirre, A. González, M. Navarro, Ó. Castaño, J.A. Planell, E. Engel, Control of microenvironmental cues with a smart biomaterial composite promotes endothelial progenitor cell angiogenesis, Eur. Cells Mater. 24 (2012) 90–106. doi:10.22203/eCM.v024a07.

[2] N. Sachot, O. Castaño, H. Oliveira, J. Martí-Muñoz, A. Roguska, J. Amedee, M. Lewandowska, J.A. Planell, E. Engel, A novel hybrid nanofibrous strategy to target progenitor cells for cost-effective in situ angiogenesis, J. Mater. Chem. B. 4 (2016) 6967–6978. doi:10.1039/C6TB02162J.

[3] O. Castaño, N. Sachot, E. Xuriguera, E. Engel, J.A. Planell, J.-H. Park, G.-Z. Jin, T.-H. Kim, J.-H. Kim, H.-W. Kim, Angiogenesis in Bone Regeneration : Tailored Calcium Release in Hybrid Fibrous Scaffolds, ACS Appl. Mater. Interfaces. 6 (2014) 7512−7522. doi:10.1021/am500885v.

Chapter 1. Calcium phosphate glasses: An overview on their angiogenic potential and uses in bone and wound healing

1.1. Calcium phosphate glasses (CPg)

Phosphate glasses have been avoided in many fields despite their unique properties (e.g. high thermal expansion, low melting temperatures, optical properties) due to their high solubility in aqueous media [1]. For this reason, the less unique but more stable silicate glasses have overcome their use in many applications [2]. This is the case of biomaterials, whose initial aim was to replace the body mechanics by being long-term substitutes [3]. However, when new 3rd generation of biomaterials started to seek to interact with the body and be totally replaced by its own tissue, soluble phosphate glasses started to gain importance [3]. One of the first studies using a pure phosphate glass system for tissue regeneration applications was published in 2000 [4,5]. Salih et al. [5] tested how the ions released by a soluble P_2O_5-CaO-Na_2O glass system affected the *in vitro* behavior of osteoblasts. They demonstrated that by easy modification of the glass composition they could achieve different dissolution rates. The introduction of several ions within the P_2O_5 glass network has been used to create and disrupt different chemical bonds and modified the properties and stability of the bulk glass [2]. By far, the most used ion in phosphate glasses for biomedical applications has been Ca^{2+} due to their biocompatibility and good affinity with the glass P_2O_5 network [2,6]. The P_2O_5-CaO glass systems are known as calcium phosphate glasses (CPg). Their solubility and similar composition to the biological hydroxyapatite (HA) give an alternative to the long being used crystalline CP ceramics (CPc) in bone regenerative applications [7]. Among different advantages of CPg regarding CPc and calcium phosphate glass-ceramics, we can highlight their non-stochiometric composition, which allows a wider range of possible combinations with different properties, a higher and more homogeneous degradability due to the absence of different crystalline phases with different solubility, and the possibility to easily incorporate extra ions (Cu^{2+}, Co^{2+}, Zn^{2+}, Ag^{3+}, Ti^{4+}, etc.) to achieve diverse properties and bioactive responses (e.g. angiogenesis, antimicrobial effects,

osteogenesis) [4,8–11]. Although, the composition of CPg is ideal for bone regenerative applications, the high control over their solubility, their nanoscalability and the release of specific ions to induce specific bioactivity, also suggest the use of CPg for other biological applications [12–14].

1.2. Methods of synthesis

The most common method to produce glasses has been by far the melt-quenching technique [3]. Melt-quenching consists of melting a mixture of metal oxides or salts above their melting point temperature and then quench it quickly below the crystallization temperature to avoid the formation of crystalline phases. This process allows the formation of a different variety of glasses (i.e. borate, silicate, phosphate, etc.) including CPg for biomedical applications [8,15]. As advantages, melt-quenching allows an easy modification of the CPg composition by changing the amount of the metal oxides or salts before melting. However, the high temperatures applied (>1200ºC), apart from being high energy consuming (which is translated in an elevated money cost), result in the production of dense bulk glasses very difficult to nanostructured [3,7,16]. This is a limitation since biomedical devices often need to be tuned in the micro/nanoscale to improve their biological functions [17]. It is for this reason that in the last couple of decades, a low temperature glass synthesis method has gained importance. This process is known as the sol-gel method and consists of synthesizing glass networks by condensing metal alkoxides and/or salts in solution at low temperatures (Figure 1) [16,18]. The use of different alkoxide ratios also allows a high control over the final glass composition while the low temperatures applied minimize atom diffusion and sintering, permitting a higher control over the micro/nanostructure (e.g. nanoporosity, nanoparticles, etc.). However, the yields are often lower than in the melt-quenching

technique, and the glasses, if not thermally treated, will contain the presence of organics, which can modify the glass properties and have possible cytotoxic effects [16,19]. The sol-gel method is being widely used in many studies to produce nanostructured CPg combined with biocompatible polymers to produce composites with improved properties [12,20,21], as we will discuss in section 1.8.. In this thesis, we used the sol-gel method to synthesize pure binary (P_2O_5:CaO) CPg nanoparticles without extra ions that can hinder the synthesis and biocompatibility of the glass. We modified the degradability of the glasses by changing their P/Ca ratio and applying moderately low thermal treatments.

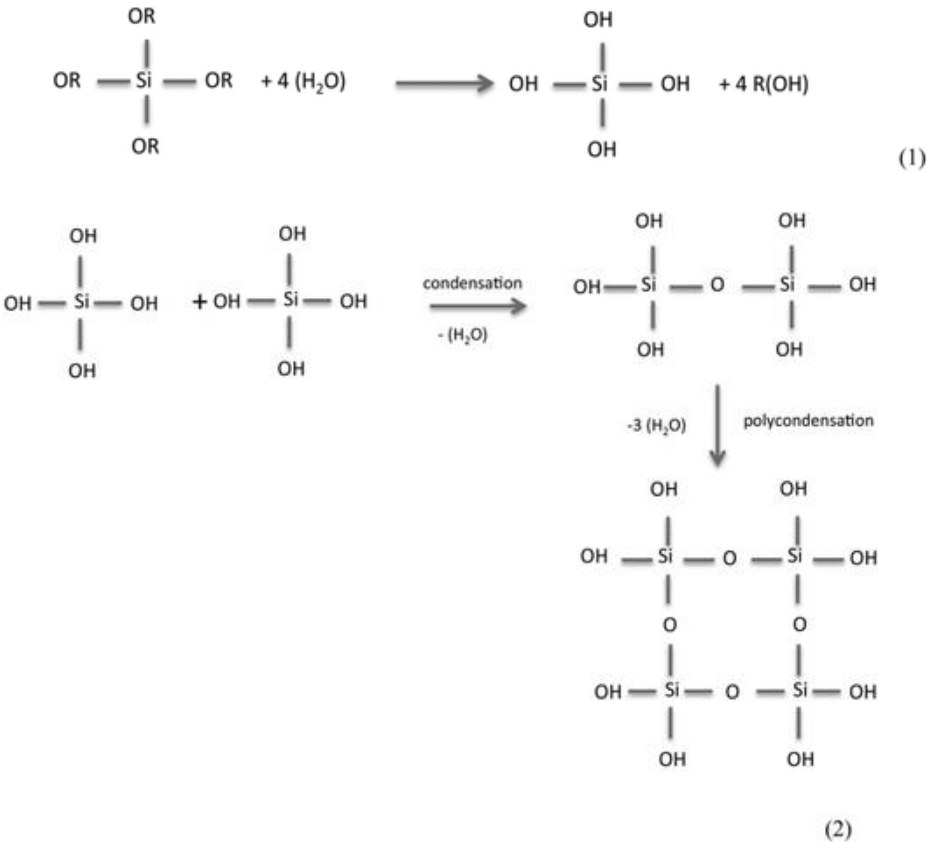

Figure 1. Sol-gel synthesis scheme of silicon glasses. Hydrolysis of the silicon alkoxide **(1)**. Condensation of the hydrolyzed silicon alkoxides to form a silicate glass network **(2)**. Image from [15] with permission.

1.3. Chemical structure and characterization

A glass can be defined as an amorphous network of condensed oxides. Such network allows the incorporation of extra ions able to modify the glass properties through different chemical interactions. In the case of CPg, the glass network is composed by condensed phosphate tetrahedrons (Q^n) and the extra incorporated ions are mainly Ca^{2+}. Other ions such as Na^+ or Ti^{4+} can be also incorporated in smaller proportions for a better adjustment of the glass solubility and/or introduce a specific bioactivity [2,8]. The stability of the glass will depend on the amount and type of interactions between the ions and the phosphate network. For instance, ions with high valence (e.g. Ca^{2+}, Ti^{4+}) will tend to increase the stability of the glass while monovalent ions (e.g. K^+, Na^+) can be used to increase its solubility as they will break the phosphate network not allowing connectivity with other fragments [8,22,23]. On the other hand, an excessive amount of extra ions will disrupt the condensed network leading to the formation of amorphous calcium phosphate salts. In the case of CPg, there is not much information about the chemical structure when Ca^{2+}>50% [2]. As we will see in Chapter 2, the phosphate network is disrupted into amorphous calcium trimetaphosphates (ACTMP), pyrophosphates (ACPP) and orthophosphates (ACP) as the Ca^{2+} content increases respectively [2,24,25]. The characterization of glasses is not trivial due to their amorphous nature. X-ray diffraction, an efficient tool to characterize crystalline CPc, is fairly ineffective with glasses. It can be used to discard the presence of crystalline phases in a glass system and to confirm and quantify its amorphous structure (Figure 2), but it does not differentiate among different amorphous phases like CPg or ACP [26].

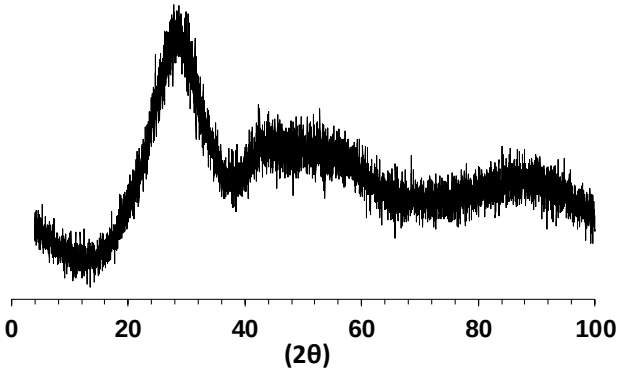

Figure 2 Typical X-ray diffraction spectrum of a CPg showing its amorphous structure.

The maximum expression of a phosphate glass is P_2O_5, which is composed by phosphate units linked to three other phosphates (Q^3) (Figure 3) [2]. The introduction of Ca^{2+} will disrupt the condensed phosphate interactions converting the P_2O_5 in cyclic (Q^2) or open-chained (Q^2 and Q^1) metaphosphates [2]. A further increase of Ca^{2+} will shorten the length of the metaphosphates increasing the amount Q^1 units (pyrophosphates) until their total isolation into orthophosphate units (Q^0) [2,24,25].

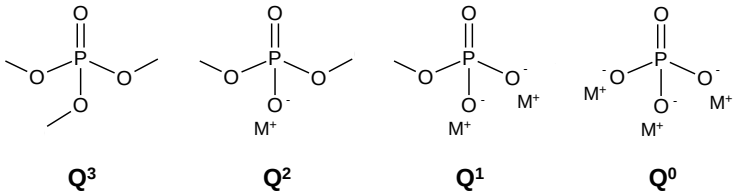

Figure 3. The different Q^n units of CPg. M^+ refers to the addition of monovalent cations. Image adapted from [2] with permission.

Phosphorus nuclear magnetic resonance (^{31}P NMR) spectroscopy can detect the amount and type of these Q^n units (Figure 4). It is very sensitive to changes in the covalent bonds surrounding the ^{31}P nuclei, being very useful to characterize CPg [24]. ^{31}P NMR can also show differences depending on the extra cations introduced (e.g. Ca^{2+}, Na^{2+}, Ti^{4+}, etc.) [24]. However, the ionic nature of such bonds results in small peak shifts

very difficult to identify. The use of NMR for these other ions or even oxygen does not give much information since the low abundance of the isotopes (^{43}Ca, ^{23}Na, ^{17}O, etc.) and their quadrupole moment result in long spectra acquisition times and broad signals difficult to interpret [27,28]. Nowadays, ^{31}P NMR is the most accessible and efficient technique to characterize CPg and can be combined with X-ray diffraction or infrared spectroscopy (FTIR) to extend or support the given information [18,29]. In this thesis, we mostly relied on ^{31}P NMR spectroscopy combined with X-ray diffraction, FTIR spectroscopy and other complementary techniques, to characterize the synthesized CPg nanoparticles.

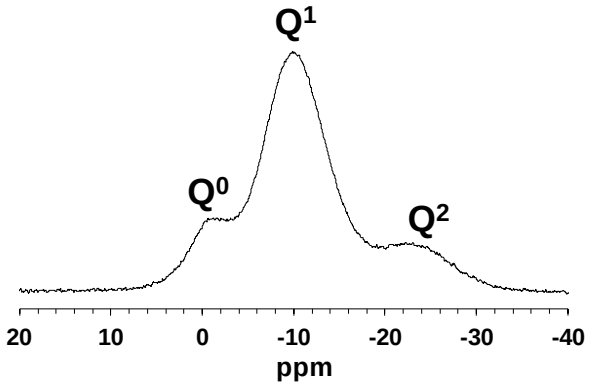

Figure 4. ^{31}P MAS NMR spectrum of a CPg showing its different Q^n units.

1.4. Bone regenerative applications

The similar composition to bone hydroxyapatite (HA) and the solubility of CPg make their use ideal for bone regenerative applications [5]. Hench et al. developed in the late 60s the first synthetic material that chemically bind to bone. This material was a $45SiO_2$-$24.5CaO$-$24.5Na_2O$-$6P_2O_5$ glass system (Bioglass®) and it was a revolution since at that time there were many rejections of implanted metal alloys [16,30]. Moreover, the discovery of a synthetic material with such properties offered an alternative to the

expensive and risky use of growth factors such as bone morphogenetic proteins (BMPs) [31–33]. There are two described mechanisms that attempt to explain the good integration of Bioglass® with bone. The first and more accepted mechanism hypothesizes that the precipitation of HA due to the partial dissolution of the glass is the responsible of the good integration with bone [16]. The second mechanism proposes that the ions released by the glass directly stimulate bone progenitor cells to be differentiated and produce bone [16]. These osteogenic properties have also been observed in soluble CP materials (e.g. β-tricalcium phosphate, biphasic calcium phosphate, CPg, etc.) based on similar mechanisms [5,34]. The advantage regarding Bioglass® is that CP are mainly composed by ions highly abundant in the body while Bioglass® contains a significant amount of SiO_2. Although, it is suspected that the release of SiO_4^{4-} could induce osteogenesis and angiogenesis (formation of blood vessels from pre-existing ones) it is not so well understood how this ion is metabolized in the body and what are its side effects [4,16,35]. Moreover, some authors maintain that osteoclasts are not able to reabsorbed the SiO_2 glass network due to its high stability, not being this removed from the body [5,16]. On the contrary, CPg are completely resorbable by spontaneous degradation. In addition, the amorphous nature of CPg results in a homogeneous degradation, minimizing the detachment of small particles with possible cytotoxic effects. Some studies have been carried out to evaluate the osteogenic properties of different CPg systems with positive results [5,7,23,36,37]. Our group have been working with the system $44.5P_2O_5$:44.5CaO:6NaO:$5TiO_2$ (G5) observing promising results not only in osteogenesis but also in angiogenesis, as we will discuss in section 1.6. [12,20,38]. In one of this studies [38], we supported the Tissue Bioengineering department of the University of Bordeaux (France) with the fabrication of polylactic acid (PLA) nanofiber scaffolds containing G5 nanoparticles, and (hydroxypropyl)methyl cellulose (HPMC) gels containing CPg particles, to test their bone regenerative capacity in rat condylar defects. The PLA-G5 fibers function, apart from constraining the HPMC gels, was to promote vascularization through the defect. The

results were very promising, showing that the presence of the CPg in the HMMC gels increased the volume of produced bone and the amount of blood vessels (Figure 5), indicating that the resorbable CPg enhanced the consolidation of bone fractures through the stimulation of vascularization.

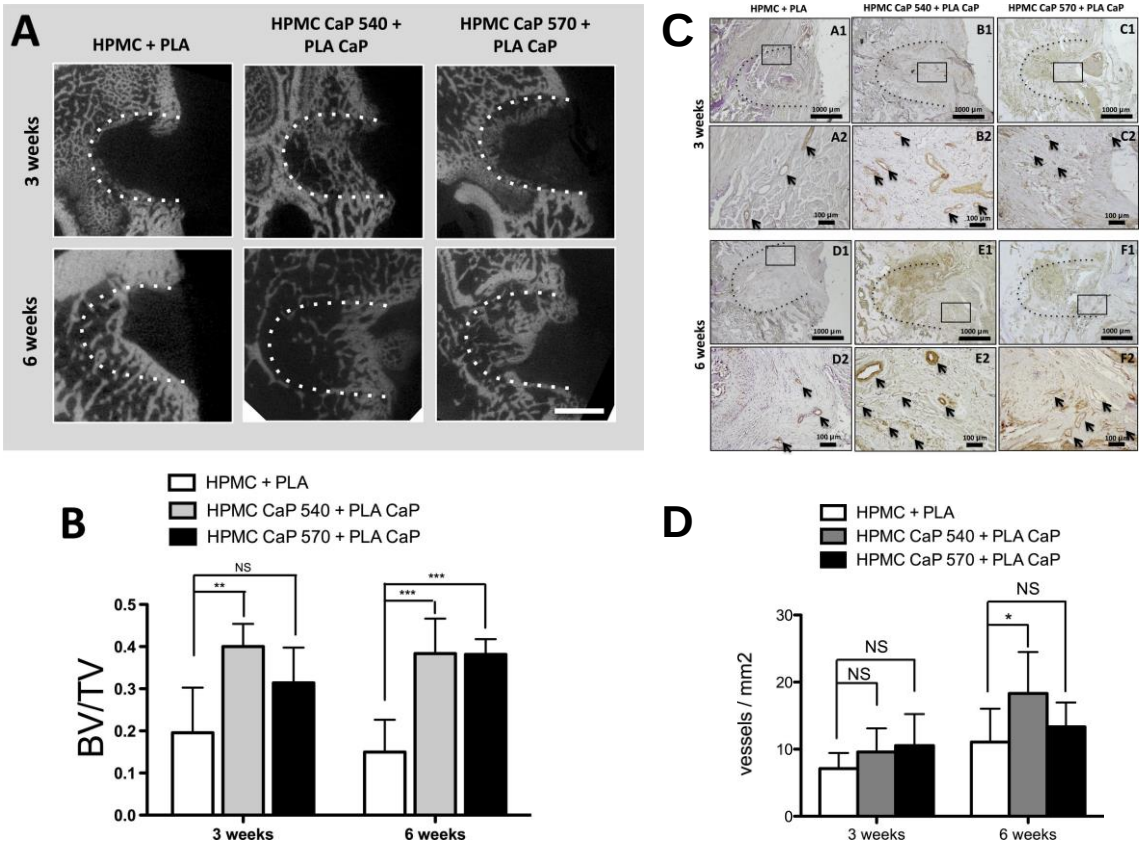

Figure 5. Micro-CT evaluation of the bone volume (BV) produced **A, B)** in the rat condyle implantation of HPMC gels containing CPg particles (CaP) constricted with PLA nanofibers containing CPg nanoparticles. CD31 immunochemistry of histological sections showing the presence of blood vessels (arrows) **C)** and quantification of blood vessels density in the histological images **D)**. 540 and 570 refers to the treatment temperatures applied to the CPg. For more information please refer to [38]. I did not perform the *in vivo* experiments I assisted with the production and characterization of the PLA nanofibers and the CPg nanoparticles. Images adapted from [38] with permission.

1.5. Antimicrobial properties

The increased resistance of bacteria against antibiotics due to general abuse is generating problems associated with infections not only in orthopaedical surgeries but also in other medical interventions [2,39]. On the other hand, the high bioactivity of CP materials provides a nice platform for bacterial attachment and spreading [40,41]. Therefore, there is a need to develop alternative strategies that avoid bacterial infection. Some ions such as Ag^{+}, Cu^{2+}, Ga^{3+}, Zn^{2+} have demonstrated to have specific antimicrobial properties [2,9,10,39,42]. The high affinity of the P_2O_5 glass network with other ions can easily incorporate such antimicrobial cations and introduce a barrier to avoid the attachment of microorganisms. Moreover, the high control in the CPg degradability allows the possibility of tuning the release of these ions and get antimicrobial properties not only during the surgery but also in the post-operatory recovery [42]. The fabrication of biomaterials with antimicrobial properties can increase even more their competitiveness due to the reduction of strict and expensive sterilization procedures that they have to undergo during the surgery intervention and in the synthesis and storage of the material. There are many studies about ceramic CP and silicate glasses doped with antimicrobial ions [14,16,39]. However, the relatively young age of CPg in the field of biomaterials results in a few research publications about this topic. We found few studies that doped CPg with Ag^{+}, Cu^{2+}, F^{-}, and Ga^{3+} and showed antimicrobial properties against several microorganisms [2,9,42,43]. They exhibited potential applications not only for orthopaedical surgeries but also in other medical interventions like dental health care and the prevention of infections in urinary catheters [2]. We are currently working in doping CPg nanoparticles with Zn^{2+}, another antimicrobial ion with promising results [39,44]. Interestingly, we introduced for the first time Zn^{2+} in a controlled way in CPg nanoparticles synthesized by the sol-gel method, using an own synthesized Zn^{2+} dialkoxyalkoxide [45]. Although experiments are still on

going and the solubility of the particles needs to be further adjusted, preliminary *in vitro* tests showed certain antibacterial properties against *Pseudomonas aeruginosa* and *Staphylococcus aureus* (Figure 6), two of the main bacteria strains causing infections in medical devices [46].

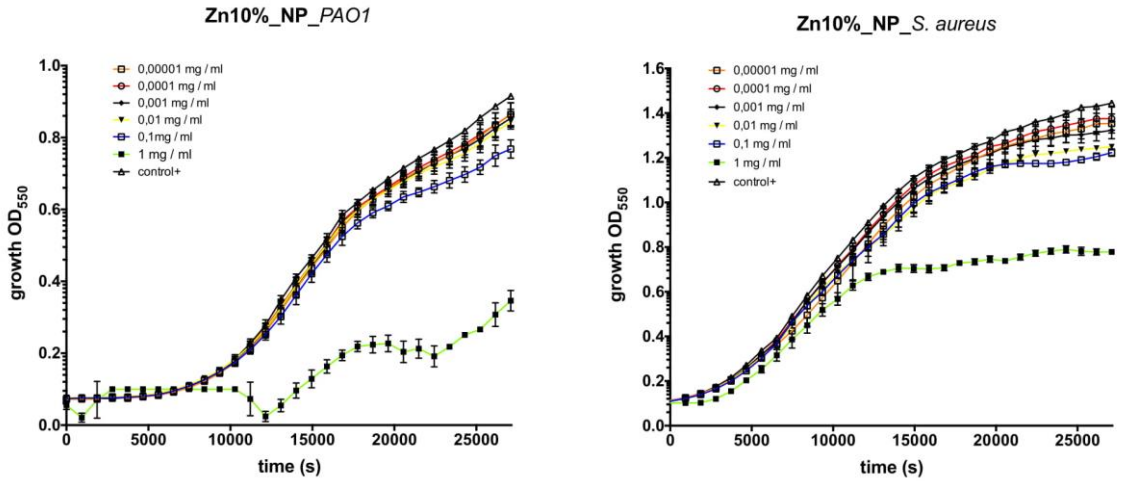

Figure 6. Antibacterial properties of CPg nanoparticles containing 10% of Zn^{2+} against *Pseudomonas aeruginosa* (*PAO1)* and *Staphylococcus aureus* (*S. aureus*). Graphs show bacterial growth over time when incubated with extracts of the CPg nanoparticles incubated at different concentrations in bacteria media. We synthesized the particles with the help of Kevin Weise, a master student from Ecole Européenne d'Ingénieurs en Génie des Matériaux (EEIGM). Experiments with bacteria were performed by Pep Astola from the Bacterial Infections: antimicrobial therapies group (Dr. Eduard Torrents group) at the Institute of Bioengineering of Catalonia (IBEC).

A consideration regarding the incorporation of metal ions in the glass is that one must be careful with the amount introduced. Slightly low amounts can significantly decrease the solubility of the glass minimizing not only the antimicrobial properties but also the own bioactivity of the glass. Another aspect to consider is that some of these ions (e.g. Ag+, Cu^{2+}) can present acute cytotoxicity at moderately high concentrations [43,47] or in the case of Cu^{2+} be involved in the development of cancer tumors [48,49]. Therefore, their

release must be highly controlled. On the contrary, Zn^{2+} has been reported as beneficial in several biological processes like osteoblast proliferation and differentiation, DNA synthesis and enzyme activity [39,44], making its use potentially safer for biological applications.

1.6. Angiogenic potential

Degradable CP materials have demonstrated to favor vascularization [50–52]. However, more attention has been focused in decoding their osteogenic potential than the benefits in inducing vascularization [53]. Vascularization is usually needed for the regeneration of many tissues, including bone. Therefore, it is important to consider its relevance in tissue regeneration. Fortunately, there is an increase interest among the research community to understand better the mechanisms involved in the formation of blood vessels. Blood vessels can grow through two different processes; angiogenesis and vasculogenesis [13], being angiogenesis more commonly observed since it involves the sprouting of blood vessels from pre-existing ones. For this reason, most of the developed strategies to induce vascularization in biomaterials involved angiogenesis [50,51,53]. The use of angiogenic factors such as the vascular endothelial growth factor (VEGF) seemed very promising since they are the natural chemical cues that the body uses to control the spreading of blood vessels. However, the lack of knowledge about their involved biology makes the current use of growth factors risky, unpredictable and expensive [13,53]. On the other hand, proangiogenic synthetic materials such as CPg stimulate the own body to orchestrate the involved mechanisms in the formation of blood vessels, reducing the need of using allogenic growth factors or cells. But through what mechanisms CPg induced angiogenesis? We recently found that increased loads of CPg

nanoparticles in PLA nanofibers increased the subcutaneous formation of blood vessels in mice through the action of macrophages (Figure 7) [12].

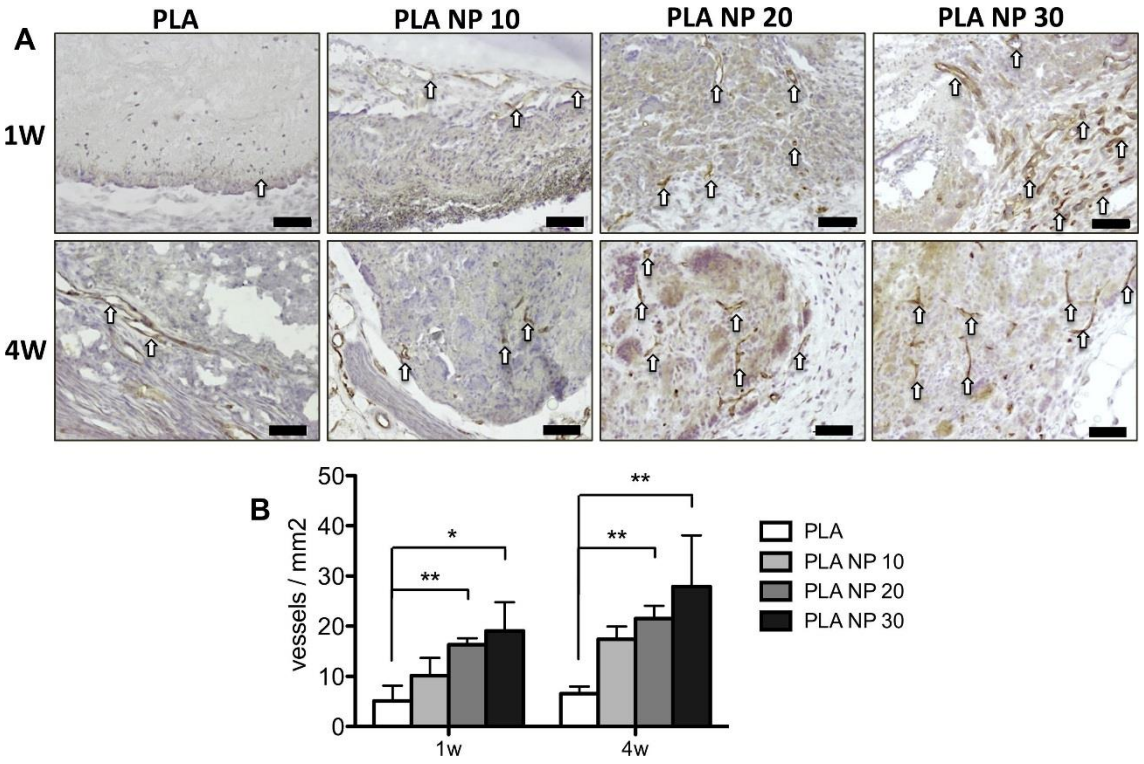

Figure 7. CD31 immunochemistry of histological sections for the subcutaneous implantation of PLA nanofibers loaded with different amounts of CPg nanoparticles after 1 and 4 weeks (1W, 4W) **A)**, arrows point blood vessels. Blood vessels quantification of the histological sections **B)**. I did not perform the *in vivo* experiments I assisted with the production and characterization of the PLA nanofibers and the CPg nanoparticles. For more details please refer to [12]. Images adapted from [12] with permission.

The causes were not well understood but a controlled local inflammatory response due to the scaffold ion release burst during the first stages of implantation could be the reason. On the other hand, our group has evidences that specific extracellular Ca^{2+} concentration ranges are able to regulate angiogenesis through the action of cellular calcium-sensing receptors (CaSRs). Aguirre et al. observed that the release of certain

Ca^{2+} gradients by a CPg/PLA-scaffold, together with the mechanical stimulus, induced the CaSR regulated synthesis of VEGF by endothelial progenitor cells (EPCs), and favored their differentiation into blood vessels (Figure 8) [54].

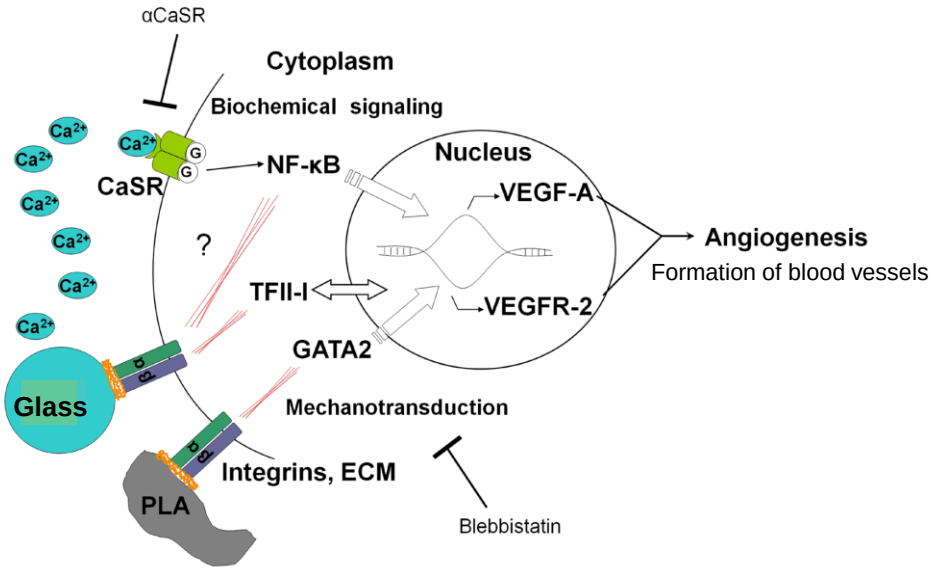

Figure 8. Scheme illustrating the angiogenic effects of the released Ca^{2+} and the mechanical stimulus of a CPg(Glass)/PLA-scaffold in EPCs. For more details please refer to [54]. Image adapted from [54] with permissions.

Therefore, controlling the Ca^{2+} release of CPg over the implantation time could benefit the regeneration of tissue through vascularization. However, in the mentioned studies the solubility of the CPg was very high when synthesized by the sol-gel method in form of nanoparticles [12]. In this thesis, we were focused on sustaining the Ca^{2+} release of CPg nanoparticles synthesized by the sol-gel method and therefore prolonged their angiogenic effects. Other alternative strategies to induce vascularization, include the incorporation of angiogenic ions to the glass system to give an extra angiogenic potential. Among these ions there is Cu^{2+} or Co^{2+} with reported angiogenic effects [11,55]. However, again their possible biological side effects must be considered as well as the produced changes in the solubility of the glass [49,56].

1.7. Wound healing applications

As we reported in section 1.6., CPg can induce the formation of blood vessels. This capacity is not only useful for bone regenerative applications but also for the regeneration of softer tissues. Among them, the healing of chronic skin wounds (wound healing) need from strategies that favor vascularization [57]. Skin wounds can become chronic due to complications associated with infections or disorders in the healing mechanisms due to for example diabetes or obesity [58–60]. The result is a poor vascularization in the wound site (ischemia) that impairs a normal healing. The current treatments for healing these types of wounds are inefficient and patients suffer a high morbidity, pain and sometimes amputation is required [61,62]. The angiogenic potential of CPg can introduce benefits in the treatment of chronic skin wounds. However, most of the studies about CPg are focused in bone regeneration due to their similar composition [5,7,23], not being many studies about their use in the healing of soft tissues [13]. Our group has recently published the use of a polyethylene glycol (PEG)-based hydrogel containing CPg nanoparticles to enhance the survival of implanted mesenchymal stem cells (MSCs) and favor the regeneration of soft tissues. In this study Navarro-Requena et al. [13] demonstrated that the presence of the CPg nanoparticles increased the survival of MSCs and observed benefits in the promotion of vascularization when implanted in the chick chorioallantoic membrane (CAM) (Figure 9) and mice fat tissue. In a parallel study, Navarro-Requena et al. also observed that the ions released by a CPg stimulated responses on dermal fibroblasts that could favor skin wound healing [63]. Since these cells play an essential role in the skin healing process [64], by increasing their potential we can accelerate the recovery of hard-to-heal wounds such as chronic skin injuries.

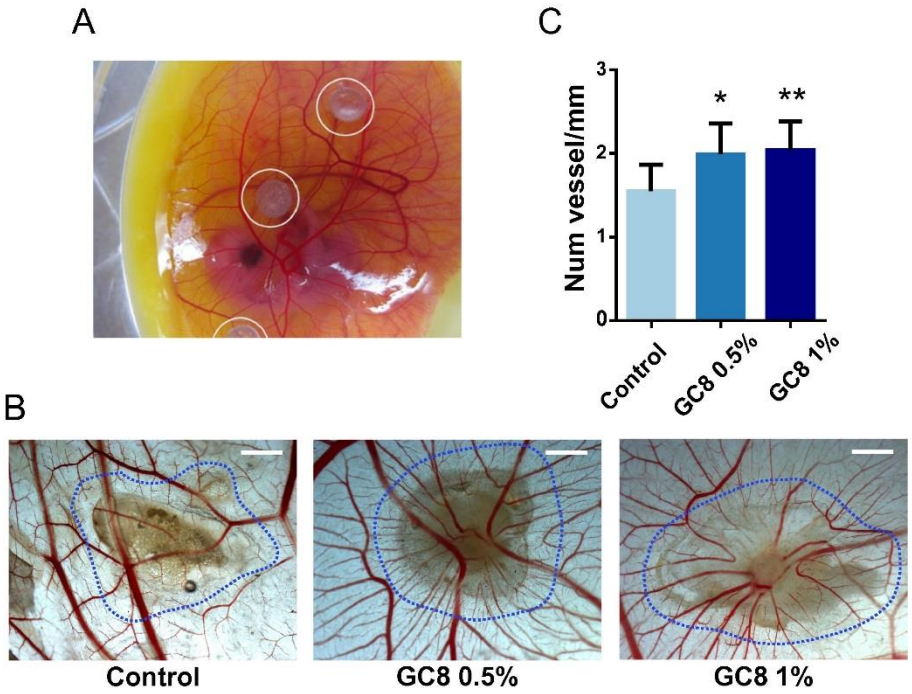

Figure 9. Navarro-Requena et al. [13] showing how degradable CPg nanoparticles embedded in methylcellulose (MEC) discs enhanced vascularization in the CAM model. Ex-ovo CAM model containing the MEC (Circles) **A)**. Selected images of the pure MEC discs (Control) and the MEC discs containing 0.5% or 1% of the CPg nanoparticles (GC8 0.5%, GC8 1%) after being 3 days in the CAM model **B)**. Quantification of the number of blood vessels converging towards the MEC discs in the CAM images **C)**. GC8 refers to a CPg containing 8% of Ti^{4+}. Image adapted from [13] with permission.

Going further, we have already demonstrated (paper under development), that PLA nanofiber dressings containing degradable CPg nanoparticles significantly increased the healing of ischemic cutaneous wounds in diabetic and obese mice in comparison to conventional Mepilex® dressings, already used in the clinics to treat these types of wounds. In this study (which I supported with the fabrication and characterization of the PLA-CPg dressings), Perez-Amodio et al. correlated the mentioned improvements with an increase in the vascularization at early stages of the healing, and with a higher fibroblast activity, both attributed to the Ca^{2+} released by the degradation of the

dressings. However, in this thesis we considered that the simultaneous release of inorganic phosphate (Pi) could also induce the calcification of the wound site, which would not be ideal for the healing of soft tissues [64]. For this reason, we avoided the presence of Pi in the glass system and synthesized pure Ca^{2+} containing degradable nanoparticles for wound healing applications.

1.8. Scaffolds manufacturing techniques

The development of synthetic scaffolds have a great potential for biomedical applications since there is the possibility to avoid the use of drugs or biological components (e.g. growth factors, cells) with strict regulations to reach the market [65,66]. Moreover, the current manufacturing technologies allow a high control over the scaffold morphology and properties. CPg, although being less stiff than crystalline CP ceramics [5], easily break under stress and often need to be combined with a tougher matrix to create a composite with more flexibility and higher shape control [19,67,68]. The matrix is usually a biodegradable polymer from a natural (e.g. collage, alginate, gelatin) or synthetic origin. Synthetic biodegradable polymers are usually less bioactive, but they possess better mechanical properties and have less variability once implanted due to they do not undergo enzymatic degradation [69]. Among synthetic polymers, polylactic acid (PLA) have an interesting degradability rate between the more stable polycaprolactone (PCL) and the highly degradable polyglycolic acid (PGA) [69]. Moreover, the released L-lactate due to its degradation, apart from being metabolized in the Krebs cycle [69], has demonstrated to be angiogenic [70,71]. Among polymer manufacturing technics for biomedical scaffolds, we can highlight; solvent-casting, 3D printing and electrospinning technique. Most of them consist of dissolving or sintering the polymer to cast a certain shape. 3D printing has the highest control over the scaffold morphology, allowing to build

macro and microstructures with specific geometry. In the case of solvent-casting, soluble particles (i.e. porogen) can be introduced in the polymer solution to introduce porosity to the manufactured scaffold [50]. On the other hand, the electrospinning technique is nowadays the cheapest way to mimic the morphology of the extracellular matrix (ECM) collagen fibrils and achieve scaffolds with the highest surface-to-volume ration [72]. Since in this thesis we chose the electrospinning technique to fabricate the scaffolds, we will discuss it further in this section.

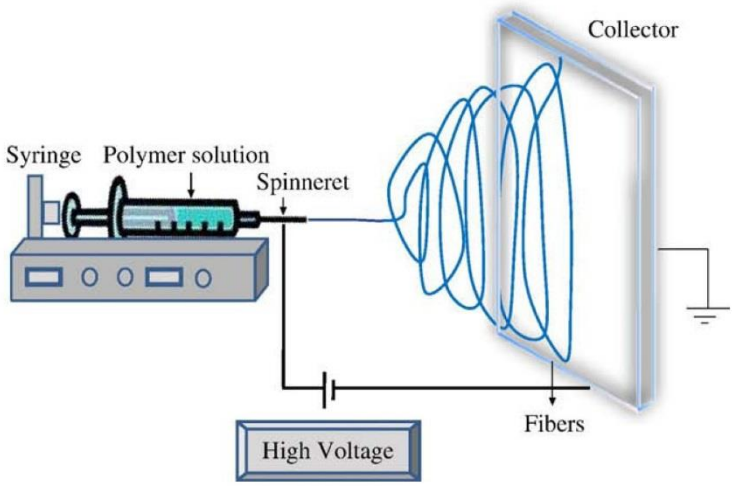

Figure 10. Scheme illustrating the electrospinning procedure. Image from [73] with permission.

The electrospinning technique consist of applying a high voltage into a polymer solution to achieve nanofibers of the polymer in question (Figure 10) [74]. When the repulsion between the dissolved polymer chains overcomes the solution surface tension a jet is projected against a grounded collector. The solvent from the jet is evaporated due to the high voltage, leaving solid nanofibers of the polymer. Using rotatory collectors or coaxial syringe tips, one can achieve aligned or core-shell polymer fibers respectively [74]. The CPg in form of nanoparticles can be easily dispersed into the polymer solution before electrospinning, as we did in several studies [12,38], to create a composite of PLA nanofibers with improved mechanical properties and bioactivity (Figure 11A). However, in order to reinforce the interaction polymer-CPg and expose the bioactive CPg onto the

surface of the fibers, we have developed alternative methods of fabrication. These methods consisted of mixing the partially hydrolyzed CPg sol-gel precursors with the polymer solution before electrospinning or covalently attach the CPg nanoparticles onto the already electrospun polymer nanofibers surface (Figure 11B,11C) [20,21]. These two approaches have given promising results. For instance, CPg blended fibers increased the mice subcutaneous formation of blood vessels [20], and Si-CPg coated fibers induced a higher cell adhesion in comparison to pure PLA nanofibers [21].

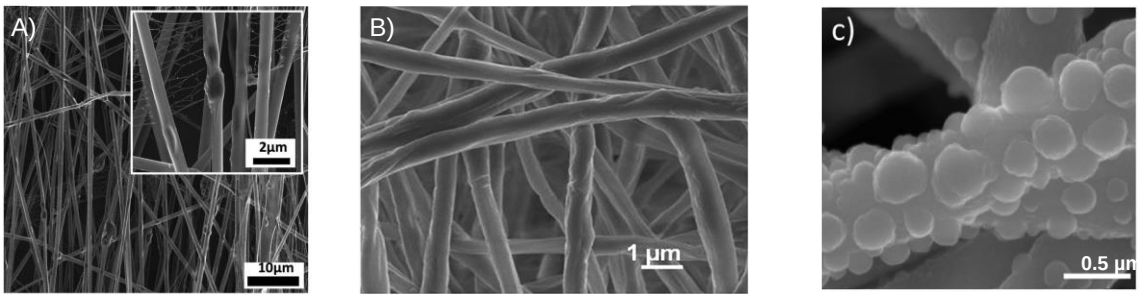

Figure 11. PLA nanofibers containing embedded CPg nanoparticles [12] **A)**. PLA nanofibers blended with the partially hydrolyzed CPg sol-gel precursors [20] **B)**. PLA nanofibers covalently coated with Si-CPg nanoparticles using the EDC/NHS surface treatment and the APTES coupling agent [21] **C)**. Images from [12,20,21] with permission.

One of the research lines in which I was involved consisted of covalently coat the PLA nanofibers with the new developed CPg nanoparticles, using the 1-ethyl-3-(-3-dimethylaminopropyl)carbodiimide/N-hydroxysuccinimide (EDC/NHS) activation method and the (3-aminopropyl)triethoxysilane (APTES) coupling agent [21]. However, problems regarding steric effects difficulted the attachment of the particles, whose were finally embedded inside the PLA nanofibers by conventional methods (Figure 11A). On the other hand, pure CPg scaffolds without a polymer matrix can be also conformed into different shapes by sintering or melting techniques. It is possible to introduce porosity to

these scaffolds by the infusion of a gas, creating a foam [7]. However, crystalline and brittle structures are usually obtained. Pure CPg fibers have been also produced for biomedical applications following sophisticated laser techniques [2]. The high length-to-diameter fiber ratio conferred a unique flexibility reducing the brittleness of the scaffold. However, in aqueous solutions these fibers broke easily due to the formation of polycrystalline structures [2,75]. In this thesis, we used the electrospinning technique to create implantable composite scaffolds of PLA nanofibers with embedded CPg nanoparticles that mimicked the natural ECM. The high surface area achieved by this technique was chosen to increase the scaffold degradability and ion release.

1.9. Conclusions

CPg offer a unique platform for temporary tissue substitutes. Their high control over their composition and solubility adapts their use for different biomedical applications. Among manufacturing techniques, the sol-gel method allows the possibility to nanostructure the glass into nanoparticles. The sol-gel method also allows the possibility to incorporate extra ions to the glass structure to tune their properties and confer specific bioactivity (e.g. antimicrobial, angiogenesis). NMR spectroscopy is among the most used techniques to characterize CPg due to their amorphous nature, nevertheless, it needs from the complementation of other techniques like X-ray diffraction or FTIR spectroscopy. Many applications of CPg have been focused in bone regeneration due to their similar composition and ability to be strongly attached. However, their angiogenic potential, in which their Ca^{2+} release plays an important role, also suggests their use in the regeneration of highly vascularized softer tissues like chronic skin wounds. The brittleness of CPg makes necessary their combination with tougher biodegradable polymers to create implantable scaffolds. In this case, the electrospinning technique offers the possibility to create nanofiber composites that mimic the morphology of the extracellular matrix. Among biodegradable polymers, PLA have demonstrated to stimulate angiogenesis due to the release of L-lactate by its degradation. However, in this thesis, we will focus on controlling the Ca^{2+} release of CPg nanoparticles synthesized by the sol-gel method to improve angiogenesis. We will create composite scaffolds combining the CPg nanoparticles with electrospun PLA nanofibers, and finally, we will study the angiogenic potential of the scaffolds for bone and wound healing applications.

1.10. References

[1] B.C. Bunker, G.W. Arnold, J.A. Wilder, Phosphate glass dissolution in aqueous solutions, J. Non. Cryst. Solids. 64 (1984) 291–316. doi:10.1016/0022-3093(84)90184-4.

[2] J.C. Knowles, Phosphate based glasses for biomedical applications, J. Mater. Chem. 13 (2003) 2395–2401. doi:10.1039/b307119g.

[3] D. Carta, D.M. Pickup, J.C. Knowles, I. Ahmed, M.E. Smith, R.J. Newport, A structural study of sol–gel and melt-quenched phosphate-based glasses, J. Non. Cryst. Solids. 353 (2007) 1759–1765. doi:10.1016/j.jnoncrysol.2007.02.008.

[4] K. Franks, I. Abrahams, J.C. Knowles, Development of soluble glasses for biomedical use part I: In vitro solubility measurement, J. Mater. Sci. Mater. Med. 11 (2000) 609–614. doi:10.1023/A:1008949527695.

[5] V. Salih, K. Franks, M. James, G.W. Hastings, J.C. Knowles, I. Olsen, Development of soluble glasses for biomedical use part II: The biological response of human osteoblast cell lines to phosphate-based soluble glasses, J. Mater. Sci. Mater. Med. 11 (2000) 615–620. doi:10.1023/A:1008901612674.

[6] A. González-Vázquez, J.A. Planell, E. Engel, Extracellular calcium and CaSR drive osteoinduction in mesenchymal stromal cells, Acta Biomater. 10. 10 (2014) 2824–2833. doi:10.1016/j.actbio.2014.02.004.

[7] M. Navarro, S. del Valle, S. Martínez, S. Zeppetelli, L. Ambrosio, J.A. Planell, M.P. Ginebra, New macroporous calcium phosphate glass ceramic for guided bone regeneration, Biomaterials. 25 (2004) 4233–4241. doi:10.1016/j.biomaterials.2003.11.012.

[8] M. Navarro, M. Ginebra, J. Clément, M. Salvador, A. Gloria, J.A. Planell,

Physicochemical Degradation of Titania-Stabilized Soluble Phosphate Glasses for Medical Applications, J. Am. Ceram. Soc. 86 (2003) 1345–1352. doi:10.1111/j.1151-2916.2003.tb03474.x.

[9] A.M. Mulligan, M. Wilson, J.C. Knowles, The effect of increasing copper content in phosphate-based glasses on biofilms of Streptococcus sanguis, Biomaterials. 24 (2003) 1797–1807. doi:10.1016/S0142-9612(02)00577-X.

[10] S.P. Valappil, D.M. Pickup, D.L. Carroll, C.K. Hope, J. Pratten, R.J. Newport, M.E. Smith, M. Wilson, J.C. Knowles, Effect of silver content on the structure and antibacterial activity of silver-doped phosphate-based glasses, Antimicrob. Agents Chemother. 51 (2007) 4453–4461. doi:10.1128/AAC.00605-07.

[11] C. Peticone, D.D.S. Thompson, G.J. Owens, H. Kim, M. Micheletti, J.C. Knowles, I. Wall, Towards modular bone tissue engineering using Ti – Co-doped phosphate glass microspheres : cytocompatibility and dynamic culture studies, J. Biomater. Appl. 32 (2017) 295–310. doi:10.1177/0885328217720812.

[12] H. Oliveira, S. Catros, C. Boiziau, R. Siadous, J. Marti-Munoz, R. Bareille, S. Rey, O. Castano, J. Planell, J. Amédée, E. Engel, The proangiogenic potential of a novel calcium releasing biomaterial: Impact on cell recruitment, Acta Biomater. 29 (2016) 435–445. doi:10.1016/j.actbio.2015.10.003.

[13] C. Navarro-Requena, J.D. Weaver, A.Y. Clark, D.A. Clift, S. Pérez-Amodio, Ó. Castaño, D.W. Zhou, A.J. García, E. Engel, PEG hydrogel containing calcium-releasing particles and mesenchymal stromal cells promote vessel maturation, Acta Biomater. (2017). doi:10.1016/j.actbio.2017.12.009.

[14] M. Yang, J. Ren, R. Zhang, Novel gallium-doped amorphous calcium phosphate nanoparticles: Preparation, application and structure study, J. Non. Cryst. Solids. 466–467 (2017) 15–20. doi:10.1016/j.jnoncrysol.2017.03.034.

[15] G. Kaur, G. Pickrell, N. Sriranganathan, V. Kumar, D. Homa, Review and the state of the art: Sol-gel and melt quenched bioactive glasses for tissue engineering, J. Biomed. Mater. Res. - Part B Appl. Biomater. 104 (2016) 1248–1275. doi:10.1002/jbm.b.33443.

[16] J.R. Jones, Review of bioactive glass : From Hench to hybrids, Acta Biomater. 23 (2015) S53–S82. doi:10.1016/j.actbio.2015.07.005.

[17] M. Navarro, A. Michiardi, O. Castaño, J.A. Planell, Biomaterials in orthopaedics, J. R. Soc. Interface. 5 (2008) 1137–1158. doi:10.1098/rsif.2008.0151.

[18] D.M. Pickup, P. Guerry, R.M. Moss, J.C. Knowles, M.E. Smith, R.J. Newport, New sol–gel synthesis of a (CaO)0.3(Na2O)0.2(P2O5)0.5 bioresorbable glass and its structural characterisation, J. Mater. Chem. 17 (2007) 4777–4784. doi:10.1039/b709955j.

[19] N. Sachot, O. Castaño, M.A. Mateos-Timoneda, E. Engel, J.A. Planell, Hierarchically engineered fibrous scaffolds for bone regeneration, J. R. Soc. Interface. 10 (2013) 20130684. doi:10.1098/rsif.2013.0684.

[20] N. Sachot, O. Castaño, H. Oliveira, J. Martí-Muñoz, A. Roguska, J. Amedee, M. Lewandowska, J.A. Planell, E. Engel, A novel hybrid nanofibrous strategy to target progenitor cells for cost-effective in situ angiogenesis, J. Mater. Chem. B. 4 (2016) 6967–6978. doi:10.1039/C6TB02162J.

[21] N. Sachot, M.A. Mateos-Timoneda, J.A. Planell, A.H. Velders, M. Lewandowska, E. Engel, O. Castaño, Towards 4th generation biomaterials: a covalent hybrid polymer–ormoglass architecture, Nanoscale. 7 (2015) 15349–15361. doi:10.1039/C5NR04275E.

[22] J.C. Knowles, K. Franks, I. Abrahams, Investigation of the solubility and ion release in the glass system K2O-Na2O-CaO-P2O5, Biomaterials. 22 (2001)

3091–3096. doi:10.1016/S0142-9612(01)00057-6.

[23] N.J. Lakhkar, J.H. Park, N.J. Mordan, V. Salih, I.B. Wall, H.W. Kim, S.P. King, J. V. Hanna, R.A. Martin, O. Addison, J.F.W. Mosselmans, J.C. Knowles, Titanium phosphate glass microspheres for bone tissue engineering, Acta Biomater. 8 (2012) 4181–4190. doi:10.1016/j.actbio.2012.07.023.

[24] J.P. Fletcher, R.J. Kirkpatrick, D. Howell, S.H. Risbud, 31P Magic-angle Spinning Nuclear Magnetic Resonance Spectroscopy of Calcium Phosphate Glasses, J. Chem. Soc. Faraday Trans. 89 (1993) 3297–3299. doi:10.1039/FT9938903297.

[25] I. Abrahams, K. Franks, G.E. Hawkes, G. Philippou, J. Knowles, T. Nunes, 23Na , 27Al and 31P NMR and X-ray powder diffraction study of Na/Ca/Al phosphate glasses and ceramics, J. Mater. Chem. 7 (1997) 1573–1580. doi:10.1039/A608325K.

[26] L. Jiang, Y. Li, Y. Shao, Y. Zhang, R. Han, S. Li, W. Wai, Enhanced removal of humic acid from aqueous solution by novel stabilized nano-amorphous calcium phosphate : Behaviors and mechanisms, Appl. Surf. Sci. 427 (2018) 965–975. doi:10.1016/j.apsusc.2017.08.104.

[27] D. Lee, C. Leroy, C. Crevan, L. Bonhomme-Coury, F. Babonneau, D. Laurencin, C. Bonhomme, G. De Paëpe, Interfacial Ca2+ environments in nanocrystalline apatites revealed by dynamic nuclear polarization enhanced 43Ca NMR spectroscopy, Nat. Commun. 8 (2017) Article number 14104. doi:10.1038/ncomms14104.

[28] I.P. Gerothanassis, Oxygen-17 NMR spectroscopy : Basic principles and applications (Part I), Prog. Nucl. Magn. Reson. Spectrosc. 56 (2010) 95–197. doi:10.1016/j.pnmrs.2009.09.002.

[29] D. Carta, J.C. Knowles, M.E. Smith, R.J. Newport, Synthesis and structural characterization of P2O5–CaO–Na2O sol–gel materials, J. Non. Cryst. Solids. 353 (2007) 1141–1149. doi:10.1016/j.jnoncrysol.2006.12.093.

[30] V. Krishnan, T. Lakshmi, Bioglass: A novel biocompatible innovation, J. Adv. Pharm. Technol. Res. 4 (2013) 78. doi:10.4103/2231-4040.111523.

[31] D.H. Bach, H.J. Park, S.K. Lee, The Dual Role of Bone Morphogenetic Proteins in Cancer, Mol. Ther. - Oncolytics. 8 (2018) 1–13. doi:10.1016/j.omto.2017.10.002.

[32] E.L. Lord, J.R. Cohen, Z. Buser, H.J. Meisel, D.S. Brodke, S.T. Yoon, J.A. Youssef, J.C. Wang, J.B. Park, Trends, Costs, and Complications of Anterior Cervical Discectomy and Fusion With and Without Bone Morphogenetic Protein in the United States Medicare Population, Glob. Spine J. 7 (2017) 603–608. doi:10.1177/2192568217699207.

[33] E.A. Barcak, M.J. Beebe, Bone Morphogenetic Protein: Is There Still a Role in Orthopedic Trauma in 2017?, Orthop. Clin. North Am. 48 (2017) 301–309. doi:10.1016/j.ocl.2017.03.004.

[34] A. Barradas, H. Yuan, C. van Blitterswijk, P. Habibovic, Osteoinductive biomaterials: current knowledge of properties, experimental models and biological mechanisms, Eur. Cells Mater. 21 (2011) 407–429. doi:10.22203/eCM.v021a31.

[35] K. Lin, Y. Liu, H. Huang, L. Chen, Z. Wang, J. Chang, Degradation and silicon excretion of the calcium silicate bioactive ceramics during bone regeneration using rabbit femur defect model, J. Mater. Sci. Mater. Med. 26 (2015) 1–8. doi:10.1007/s10856-015-5523-2.

[36] M. Navarro, E.S. Sanzana, J. a. Planell, M.P. Ginebra, P. a. Torres, In Vivo

Behavior of Calcium Phosphate Glasses with Controlled Solubility, Key Eng. Mater. 284–286 (2005) 893–896. doi:10.4028/www.scientific.net/KEM.284-286.893.

[37] Y.-K. Lee, J. Song, H.J. Moon, S.B. Lee, K.M. Kim, K.N. Kim, S.H. Choi, R.Z. LeGeros, In Vitro and In Vivo Evaluation of Non-Crystalline Calcium Phosphate Glass as a Bone Substitute, Key Eng. Mater. 254–256 (2004) 185–188.

[38] H. Oliveira, S. Catros, O. Castano, S. Rey, R. Siadous, D. Clift, J. Marti-Munoz, M. Batista, R. Bareille, J.A. Planell, E. Engel, The proangiogenic potential of a novel calcium releasing composite biomaterial : Orthotopic in vivo evaluation, Acta Biomater. 54 (2017) 377–385. doi:10.1016/j.actbio.2017.02.039.

[39] T.S. Sampath Kumar, K. Madhumathi, Y. Rubaiya, M. Doble, Dual Mode Antibacterial Activity of Ion Substituted Calcium Phosphate Nanocarriers for Bone Infections, Front. Bioeng. Biotechnol. 3 (2015) 1–10. doi:10.3389/fbioe.2015.00059.

[40] Y. SAKAMOTO, H. OCHIAI, I. OHSUGI, Y. INOUE, Y. YOSHIMURA, K. KISHI, Evaluation of Antibiotic-loaded Calcium Phosphate Bone Cement in an Cranium-infected Experimental Model, Neurol. Med. Chir. (Tokyo). 54 (2014) 647–653. doi:10.2176/nmc.oa.2013-0295.

[41] S.L. Zhang, Z.Y. Meng, Z. Dong, G. Cao, Z. Yang, Drug-impregnated calcium phosphate cement for repairing bone defect and preventing infection, Chinese J. Clin. Rehabil. 10 (2006) 67–69. http://www.scopus.com/inward/record.url?eid=2-s2.0-33747359083&partnerID=tZOtx3y1.

[42] D.M. Pickup, S.P. Valappil, R.M. Moss, H.L. Twyman, P. Guerry, M.E. Smith, M. Wilson, J.C. Knowles, R.J. Newport, Preparation , structural characterisation and antibacterial properties of Ga-doped sol–gel phosphate-based glass, J Mater Sci. 44 (2009) 1858–1867. doi:10.1007/s10853-008-3237-2.

[43] S. Lee, T. Nakano, T. Kasuga, Structure, dissolution behavior, cytocompatibility, and antibacterial activity of silver-containing calcium phosphate invert glasses, J. Biomed. Mater. Res. - Part A. 105 (2017) 3127–3135. doi:10.1002/jbm.a.36173.

[44] N. Ohtsu, Y. Kakuchi, T. Ohtsuki, Antibacterial effect of zinc oxide/hydroxyapatite coatings prepared by chemical solution deposition, Appl. Surf. Sci. 445 (2018) 596–600. doi:10.1016/j.apsusc.2017.09.101.

[45] E. Sattarzadeh, G. Mohammadnezhad, M.M. Amini, Size-controlled synthesis of ZnO nanocrystals from diethylzinc and donor-functionalized alcohols, Mater. Lett. 65 (2011) 527–529. doi:10.1016/j.matlet.2010.11.005.

[46] S.P. Valappil, J.C. Knowles, M. Wilson, Effect of silver-doped phosphate-based glasses on bacterial biofilm growth, Appl. Environ. Microbiol. 74 (2008) 5228–5230. doi:10.1128/AEM.00086-08.

[47] A. Bernhardt, M. Schamel, U. Gbureck, M. Gelinsky, Osteoclastic differentiation and resorption is modulated by bioactive metal ions Co2+, Cu2+ and Cr3+ incorporated into calcium phosphate bone cements, PLoS One. 12 (2017) 1–18. doi:10.1371/journal.pone.0182109.

[48] T. Ishida, Anti-Cancer Activities of Cu(Ⅱ) Ion Solution in Progression and Development against Cancer and Tumor Cells, Glob. J. Med. Reseach. 17 (2017) 7–16.

[49] S.A. Lowndes, A.L. Harris, The role of copper in tumour angiogenesis, J. Mammary Gland Biol. Neoplasia. 10 (2005) 299–310. doi:10.1007/s10911-006-9003-7.

[50] O.F. Vila, J.R. Bagó, M. Navarro, M. Alieva, E. Aguilar, E. Engel, J. Planell, N. Rubio, J. Blanco, Calcium phosphate glass improves angiogenesis capacity of poly(lactic acid) scaffolds and stimulates differentiation of adipose tissue-derived

mesenchymal stromal cells to the endothelial lineage, J. Biomed. Mater. Res. - Part A. 101 A (2013) 932–941. doi:10.1002/jbm.a.34391.

[51] Y. Chen, J. Wang, X.D. Zhu, Z.R. Tang, X. Yang, Y.F. Tan, Y.J. Fan, X.D. Zhang, Enhanced effect of β-tricalcium phosphate phase on neovascularization of porous calcium phosphate ceramics: In vitro and in vivo evidence, Acta Biomater. 11 (2015) 435–448. doi:10.1016/j.actbio.2014.09.028.

[52] W. Xiao, Y.-M. Liu, K.-G. Ren, F. Shi, Y. Li, W. Zhi, J. Weng, S.-X. Qu, Evaluation of Vascularization of Porous Calcium Phosphate by Chick Chorioallantoic Membrane Model ex vivo, Wuji Cailiao Xuebao/Journal Inorg. Mater. 32 (2017) 649–654. doi:10.15541/jim20160535.

[53] A. Malhotra, P. Habibovic, Calcium Phosphates and Angiogenesis: Implications and Advances for Bone Regeneration, Trends Biotechnol. 34 (2016) 983–992. doi:10.1016/j.tibtech.2016.07.005.

[54] A. Aguirre, A. González, M. Navarro, Ó. Castaño, J.A. Planell, E. Engel, Control of microenvironmental cues with a smart biomaterial composite promotes endothelial progenitor cell angiogenesis, Eur. Cells Mater. 24 (2012) 90–106. doi:10.22203/eCM.v024a07.

[55] C. Wu, Y. Zhou, M. Xu, P. Han, L. Chen, J. Chang, Y. Xiao, Copper-containing mesoporous bioactive glass scaffolds with multifunctional properties of angiogenesis capacity, osteostimulation and antibacterial activity, Biomaterials. 34 (2013) 422–433. doi:10.1016/j.biomaterials.2012.09.066.

[56] A.C. Cheung, S. Banerjee, J.J. Cherian, F. Wong, J. Butany, C. Gilbert, C. Overgaard, K. Syed, M.G. Zywiel, J.J. Jacobs, M.A. Mont, Systemic cobalt toxicity from total hip arthroplasties: review of a rare condition Part 1 - history, mechanism, measurements, and pathophysiology, Bone Joint J. 98–B (2016) 6–13. doi:10.1302/0301-620X.98B1.36374.

[57] S. Böttcher-Haberzeth, T. Biedermann, E. Reichmann, Tissue engineering of skin, Burns. 36 (2010) 450–460. doi:10.1016/j.burns.2009.08.016.

[58] S. Hampton, Understanding the pH balance in wound healing, J. Community Nurs. 22 (2008) 34–38.

[59] H. Chen, L. Guo, J. Wicks, C. Ling, X. Zhao, Y. Yan, J. Qi, W. Cui, L. Deng, Quickly promoting angiogenesis by using a DFO-loaded photo-crosslinked gelatin hydrogel for diabetic skin regeneration, J. Mater. Chem. B. 4 (2016) 3770–3781. doi:10.1039/C6TB00065G.

[60] A. Siebert, I. Goren, J. Pfeilschifter, S. Frank, Anti-inflammatory effects of rosiglitazone in obesity-impaired wound healing depend on adipocyte differentiation, PLoS One. 11 (2016) 1–25. doi:10.1371/journal.pone.0168562.

[61] N. Goonoo, A. Bhaw-Luximon, Analyzing polymeric nanofibrous scaffold performances in diabetic animal models for translational chronic wound healing research, Nanotechnol. Rev. 6 (2017) 583–600. doi:10.1515/ntrev-2017-0162.

[62] G. Weaver, K. Crawford, The use of Mepilex on dehisced amputation wounds, Wounds UK. 3 (2007) 70–74.

[63] C. Navarro-Requena, S. Pérez-Amodio, O. Castano, E. Engel, Wound healing-promoting effects stimulated by extracellular calcium and calcium-releasing nanoparticles on dermal fibroblasts, Nanotechnology. 29 (2018) 395102. doi:10.1088/1361-6528/aad01f.

[64] M. Ohnishi, T. Nakatani, B. Lanske, M.S. Razzaque, In vivo genetic evidence for suppressing vascular and soft-tissue calcification through the reduction of serum phosphate levels, even in the presence of high serum calcium and 1,25-dihydroxyvitamin D levels, Circ. Cardiovasc. Genet. 2 (2009) 583–590. doi:10.1161/CIRCGENETICS.108.847814.

[65] M.S. Chapekar, K.C. Gunter, FDA regulations for growth factors and related products, EXS. 61 (1992) 471–478. http://www.scopus.com/inward/record.url?eid=2-s2.0-0026494349&partnerID=40.

[66] A.A.G. Ridgway, The regulation of cell therapy products in Canada, Biologicals. 43 (2015) 406–409. doi:10.1016/j.biologicals.2015.05.013.

[67] S. Haimi, N. Suuriniemi, A.-M. Haaparanta, V. Ellä, B. Lindroos, H. Huhtala, S. Räty, H. Kuokkanen, G.K. Sándor, M. Kellomäki, S. Miettinen, R. Suuronen, Growth and Osteogenic Differentiation of Adipose Stem Cells on PLA / Bioactive Glass and PLA / β -TCP Scaffolds Growth and Osteogenic Differentiation of Adipose Stem Cells, 15 (2009) 1473–1480. doi:10.1089/ten.tea.2008.0241.

[68] E. García-Gareta, M.J. Coathup, G.W. Blunn, Osteoinduction of bone grafting materials for bone repair and regeneration, Bone. 81 (2015) 112–121. doi:10.1016/j.bone.2015.07.007.

[69] L.S. Nair, C.T. Laurencin, Biodegradable polymers as biomaterials, Prog. Polym. Sci. 32 (2007) 762–798. doi:10.1016/j.progpolymsci.2007.05.017.

[70] O. Trabold, S. Wagner, C. Wicke, H. Scheuenstuhl, M.Z. Hussain, N. Rosen, A. Seremetiev, H.D. Becker, T.K. Hunt, Lactate and oxygen constitute a fundamental regulatory mechanism in wound healing, WOUND REP REG. 11 (2003) 504–509. doi:10.1046/j.1524-475X.2003.11621.x.

[71] K.K. Chereddy, A. Lopes, S. Koussoroplis, V. Payen, C. Moia, H. Zhu, P. Sonveaux, P. Carmeliet, A. des Rieux, G. Vandermeulen, V. Préat, Combined effects of PLGA and vascular endothelial growth factor promote the healing of non-diabetic and diabetic wounds, Nanomedicine Nanotechnology, Biol. Med. 11 (2015) 1975–1984. doi:10.1016/j.nano.2015.07.006.

[72] O. Castaño, M. Eltohamy, H.-W. Kim, Electrospinning technology in tissue regeneration, Methods Mol. Biol. 811 (2012) 127–140. doi:10.1007/978-1-61779-388-2.

[73] N. Zhu, X. Chen, Chapter 12: Biofabrication of Tissue Scaffolds, in: Adv. Biomater. Sci. Biomed. Appl., 2013: pp. 315–328. doi:http://dx.doi.org/10.5772/54125.

[74] Q.P. Pham, U. Sharma, A.G. Mikos, Electrospinning of Polymeric Nanofibers for Tissue Engineering Applications: A Review, Tissue Eng. 12 (2006) 1197–1211. doi:10.1089/ten.2006.12.1197.

[75] I. Abdulhalim, C.N. Pannell, K.P. Jedrzejewski, E.R. Taylor, Cavity dumping of neodymium-doped fibre laser using an acoustooptic modulator, Opt. Quantum Electron. 26 (1994) 997–1001. doi:10.1007/BF00304999.

Chapter 2. First sol-gel synthesis of binary (P_2O_5-CaO) calcium phosphate glass nanoparticles with controlled bioactive degradation

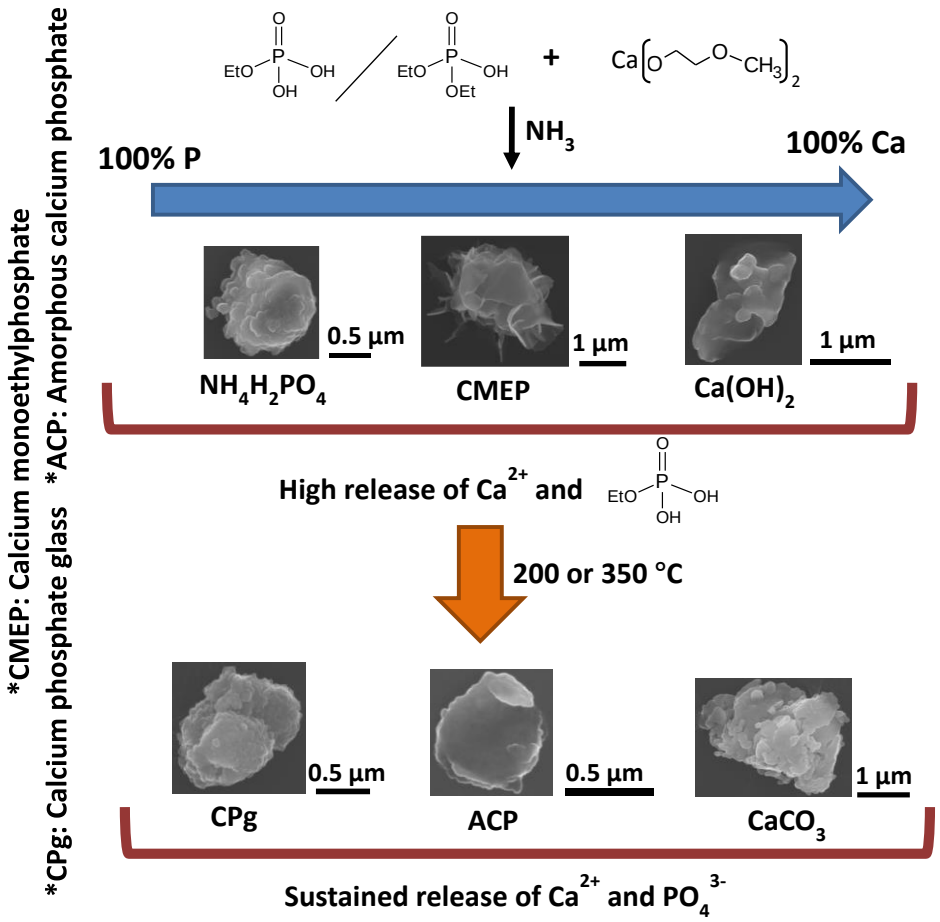

Scheme summarizing the content of the chapter

In this chapter we reported the first systematic sol-gel synthesis of binary (P_2O_5-CaO) calcium phosphate glasses (CPg) nanoparticles. We highlight “systematic” because only the strict control of the experimental conditions and the generated knowledge in the fundamental characterization of the transition sol-gel/solid allowed us to obtain this important and reproducible milestone. The study of binary CPg for biomedical applications is of interest due to their straightforward synthesis, lack of unnatural-body ions (e.g. SiO_4^{4-}, Ti^{4+}), and increase of bioactive release of Ca^{2+} and inorganic phosphate (Pi) ions. CPg nanoparticles with different Ca/P ratios were synthesized by combining ethylphosphate and calcium 2-methoxyethoxide. We applied a moderately low thermal treatment at 200 or 350 °C to stabilize the solubility of the particles in physiological conditions. The reaction between the two precursors and the formation of the particles was studied by NMR spectroscopy and other complementary techniques. We also measured the ion release (Ca^{2+} and Pi) and pH modifications when the particles were immersed in buffered aqueous medium. Before thermal treatment, we achieved highly soluble particles due to the formation of calcium monoethylphosphate. After thermal treatment, the ion release was sustained due to the elimination of ethoxides and the condensation of phosphates. We developed a cost-effective and feasible CPg platform to adjust different ion release profiles to fulfil different biological demands for tissue regeneration like for example angiogenesis, osteogenesis or wound healing.

2.1. Introduction

CPg synthesized by the sol-gel method are gaining importance in the field of tissue engineering especially in bone regeneration [1]. Their low temperature synthesis, in contrast to melt-quenched glasses, minimizes atom diffusion and sintering, allowing an outstanding control over their micro/nanostructure [2,3]. Several studies have focused in synthesizing different nanostructured CPg systems combining Pi and Ca^{2+} with other ions (e.g. Na^{+}, Ti^{4+}, SiO_4^{4-}) to achieve different properties and degradability [3–5]. However, the use of multicomponent systems hinders their synthesis and introduces ions whose metabolization is still not fully understood [6–8]. In this study, we wanted to develop binary (P_2O_5-CaO) CPg nanoparticles containing only Ca^{2+} and Pi due to their known biocompatibility. We tailored their degradability by modifying their Ca/P ratio and applying moderately low thermal treatment temperatures. The degradation of such materials in the body are able to trigger several bioactive responses. For example, it is known that the release of Ca^{2+} and Pi, participates in bone mineralization and osteogenesis [9,10]. On the other hand, Ca^{2+} also participate in many other cell metabolic processes such as chemotaxis and cell proliferation [9], and recently we found evidences that certain Ca^{2+} mM concentrations stimulate angiogenesis [2,3,11]. We chose to synthesize the CPg in the form of nanoparticles for an straightforward combination with other nanoconstructions (e.g. biodegradable polymer scaffolds) [3,10] and thus achieve biomedical devices with specific micro/nanofeatures. We synthesized the CPg nanoparticles by the sol-gel method using a mixture of mono/diethylphosphate (MEP/DEP) and calcium 2-methoxyethoxide (CMEO) (Scheme 1). These two sol-gel precursors have shown a suitable compatibility, resulting in the synthesis of CPg with a homogeneous composition [3,5]. We applied a moderately low thermal treatment (200 or 350 °C) to eliminate the organic material and stabilize the physiological solubility of the particles. The reaction between the two precursors and the characterization of the

particles, before and after thermal treatment, was studied by NMR spectroscopy (^{1}H NMR, ^{31}P NMR and ^{31}P MAS NMR) and other complementary techniques such as ESI-MS, X-ray diffraction (XRD), ATR-FTIR, EDS, elemental analysis (EA), DLS and FE-SEM. Finally, we measured the ion release (i.e. Ca^{2+} and Pi) and pH modification of the particles, before and after thermal treatment, in a 4-(2-hydroxyethyl)-1-piperazineethanesulfonic acid (HEPES) buffered solution (pH 7.4) at 37 ºC, that mimicked the physiological conditions of the body.

2.2. Materials and methods

If not otherwise specified all reagent were purchased from Sigma-Aldrich.

2.2.1. Sol-gel precursors synthesis

P and Ca precursors were synthesized as previously published [3,12]. Briefly, phosphorus pentoxide (≥99,99%) and metallic calcium granules PS (98%, Panreac) were dissolved in distilled absolute ethanol PRS (99,5%, Panreac) and anhydrous 2-methoxyethanol (99,8%) respectively. After refluxing them at the solvent boiling point under $Ar_{(g)}$ atmosphere for 12 and 24 h respectively, we obtained 4 M ethylphosphate in ethanol and 1 M calcium 2-methoxyethoxide in 2-methoxyethanol. The solutions were filtered using 0.45 µm PTFE hydrophobic Minisart® SRP25 syringe filters (Sartorius AG, Göttingen, Germany) and stored under $Ar_{(g)}$ at -20 °C.

2.2.2. CPg nanoparticles synthesis

The CPg nanoparticles were synthesized by mixing different ratios (10:0, 8.5:1.5, 6:4, 1.5:8.5 and 0:10 mL) of the P and Ca precursors respectively, in 90 mL of absolute ethanol (PRS, 99,5%, Panreac). Ammonia (PA-ACS, 30%, Panreac) was added dropwise under vigorous stirring until a suspension of particles was observed. After 12 h the particles were centrifuged, cleaned twice with absolute ethanol, once with hexane (ACS, ≥99%) and dried at 70 ºC for 2 h. Dried particles were ground and stored in a desiccator under vacuum. Then the particles were heated for 12 h at 200 or 350 ºC in a muffle furnace L9/11 (Nabertherm, Lilienthal, Germany) and stored in a desiccator under vacuum. Before and after thermal treatment, the particles were weighed in a Sartorius CP224S analytical balance (Sartorius AG, Göttingen, Germany) to know yields and mass loss.

2.2.3. ^{1}H and ^{31}P NMR spectroscopy

^{1}H and ^{31}P NMR of the two alkoxides in anhydrous ethanol-d6 (≥99,6%) and the dissolved particles (5 mg/mL) in D_2O (99.9%) plus 1.5% HCl (37%, Panreac), were performed at room temperature using a Bruker 400 MHz Avance III spectrometer (Bruker, Billerica, MA, USA) equipped with a Prodigy TCl 5 mm cryoprobe. ^{1}H NMR spectra were recorded between 16 and -3.8 ppm, applying 3.66 µs, 30° pulse, a delay of 1 s between pulses, and an acquisition time of 2.5 s. 32 scans were accumulated to have a good signal-to-noise ratio. Spectra were referenced to the ^{1}H of the deuterium solvent. ^{31}P NMR spectra were registered between 250 and -250 ppm, applying 3.76 µs, 30° pulse, a delay of 1 s between pulses, and an acquisition time of 1.6 s. 256 scans were accumulated to have a good signal-to-noise ratio. Spectra were externally referenced to H_3PO_4 (85%). ^{1}H was decoupled during ^{31}P NMR spectrum acquisition. Data were analyzed with the ACD/Spectrus Processor software [13]. The ethanol (solvent) of the phosphorus precursor was evaporated prior to analysis using a vacuum pump to better resolve possible hydrolysis or condensation of the ethylphosphate.

2.2.4. Electrospray ionization mass spectrometry (ESI-MS)

The 1 M calcium 2-methoxyethoxide was dissolved 10^4 times in absolute ethanol (PRS, 99.5%, Panreac) and analyzed on a ThermoFinnigan LTQ ion trap mass spectrometer (Thermo Fischer Scientific, Waltham, MA, USA), with sample introduction by direct infusion at 3 µL/min. The full mass spectrum scan was recorded in the mass range of m/z 50-650 using positive ion polarity. Instrument parameters included spray voltage: 3.5 kV, capillary temperature: 200 °C, capillary voltage: 75 V, and tube lens voltage: 100 V. Mass spectra were acquired by the University of Kentucky Mass Spectrometry Facility.

2.2.5. Dynamic Light Scattering (DLS)

The P and Ca precursors were dissolved (a few drops) separately and together in 1 mL of absolute ethanol (PRS, 99.5%, Panreac). The solutions were measured in a Zetasizer Nano ZS (Malvern, Worcestershire, UK) using a 10x2 mm precision Quartz Suprasil® cell 115F-QS (Hellma®Analytics, Müllheim, Germany). Results were analyzed using the Zetasizer software version 7.12 (07/12/2016) (Malvern, Worcestershire, UK) for Windows 7. Size population was expressed in volume percentage.

2.2.6. Particle composition and morphological images (EDS/FE-SEM)

A Quanta Q200 scanning electron microscope (SEM) (FEI Company, Hillsboro, OR, USA) coupled with an energy dispersive X-ray spectroscopy detector (EDS) was used at 20.0 KV and 10 mm of working distance to quantify the approximate P and Ca atomic ratio of the particles. Values express the average of at least three different measurements. For morphological images, we used the NOVA NanoSEM-230 ultrahigh-resolution field emission scanning electron microscope (FE-SEM) (FEI Company, Hillsboro, OR, USA) at 5.00 KV and 5.0 mm of working distance. In both cases, samples were coated with a thin carbon layer to improve conductivity. For morphological images, approximately 1 mg of the particles was dispersed in 1 mL of absolute ethanol PRS (99,5%, Panreac) and sonicated for several seconds with an Ultrasonic Processor UP50H (Hielscher Ultrasonics, Teltow, Germany) for a better particle dispersion. 2 µL of the dispersion were added on silicon substrates and left to dry at room temperature (RT).

2.2.7 Elemental analysis (EA)

Approximately, 2000 µg of each particles were weighed in a MX5 microbalance (Mettler-Toledo, Greifensee, Switzerland). The samples were analyzed by combustion at 1060

ºC in an elemental analyzer EA CE 1108 (Thermo Fischer Scientific, Waltham, MA, USA) to determine the mass percentage of C and N. A mixture of vanadium pentoxide and lead powder was added to facilitate combustion. Atropine was used as a standard.

2.2.8. X-ray diffraction (XRD)

The particles were manually pressed in a cylindrical standard sample holder of 16 mm of diameter and 2.5 mm of height, using a glass plate to get a flat surface. Samples were analyzed using a PANalytical X'Pert PRO MPD Alpha1 Powder Diffractometer (PANalytical, Almelo, the Netherlands) in a Bragg-Brentano $\theta/2\theta$ geometry of 240 mm of radius. The spectra were interpreted using the software ©PANalytical X'Pert HighScore (PANalytical, Almelo, the Netherlands) and the database PDF2 (2001) from the international center of diffraction data (ICDD).

2.2.9. ^{31}P MAS NMR spectroscopy

^{31}P MAS NMR spectra were performed in a Bruker 400 MHz-WB Avance-II spectrometer (Bruker, Billerica, MA, USA), externally referenced to H_3PO_4 (85%). Approximately 50 mg of the particles were placed in a ZrO_2 4 mm rotor and spun at 12 kHz. The HPDEC.AV standard pulse sequence was used to run the experiments with a 5 µs pulse length corresponding to a 90° tip angle and the recovery delay was set to 5 s. A total of 512 scans were accumulated for each spectrum to have a good signal-to-noise ratio. ^{1}H was decoupled using a Spinal-64 scheme (at 73 watts power level). Data was processed applying a FT exponential function (line broadening, *lb* 15 Hz).

2.2.10. Attenuated total reflectance infrared spectroscopy (ATR-FTIR)

Approximately 5 mg of the particles were pressed in a Spectrum Two FT-IR Spectrometer (PerkinElmer, Waltham, MA, USA) coupled with an UATR Diamond/ZnSe accessory (1 reflection). A background without particles was taken before each measurement. Spectra were analyzed using the software ©PerkinElmer Spectrum (PerkinElmer, Waltham, MA, USA) and the database ©2005-2008, Fiveash Data Management, Inc.

2.2.11. Ion release and pH measurements

3 mg of each particle (three replicates per condition) were placed in 1.5 mL microcentrifuge tubes. 1.3 mL of 0.05 M 4-(2-hydroxyethyl)piperazine-1-ethanesulfonic acid (HEPES) (99,5%) in miliQ-water at pH=7.4 was added to each tube. Tubes were placed in a Memmert incubator (Memmert Gmbh + Co KG, Schwabach, Germany) at 37 °C with gentle agitation. At 1 h, day 1, 3, 6, 9 and 14, tubes were centrifuged at 8000 rpm for 6 minutes and 1.1 mL of each media was extracted. Another 1.1 mL of 0.05 M HEPES solution was added to each tube and the particles were gently resuspended using a vortex mixer. Tubes were incubated again at 37 °C. The extracted media were frozen at -20 °C until further analysis. The pH of each extraction was measured using a Crison 50 28 pH electrode and a Crison pH-Meter GLP 22+ (Hach Company, Loveland, CO, USA) previously calibrated with 4.01, 7.00 and 9.21 pH standard solutions. The Ca^{2+} content of the extracts was measured using a colorimetric method based on the O-Cresolphthalein complexone [14,15]. Briefly, 4 µL of the extractions were added to 80 µL of 1.5 M 2-amino-2-methyl-1-propanol (AMP) (≥90%) aqueous solution with HCl (37%, Panreac) to maintain the pH at 10.4. Then 80 µL of 0.16 mM O-Cresolphthalein, 6.8 mM 8-Hydroxyquinoline (99%) and 1.19 M HCl (37%, Panreac) aqueous solution was added. The reaction between the Ca^{2+} and the O-Cresolphthalein produced a purple complex

that was measured by absorbance at 570 nm. A calibration curve (7.5, 5, 2, 1, 0.5, 0.1, 0 mM) of $CaCl_2$ ion solution for ion-selective electrodes (0.1 M) was prepared to convert absorbances to Ca^{2+} concentrations. The Pi content of the extracts was measured using the Phosphate Colorimetric Kit based on the malachite green method [16]. A calibration curve of PO_4^{3-} (25, 20, 15, 10, 5, 0 µM) was prepared from a 10 mM phosphate standard solution (included in the kit) to convert absorbance to Pi concentrations. The absorbance was measured at 650 nm wavelength. All absorbances were measured in an Infinite M200 Pro Microplate Reader (Tecan Group Ltd., Männedorf, Zürich, Switzerland).

2.3. Results and discussion

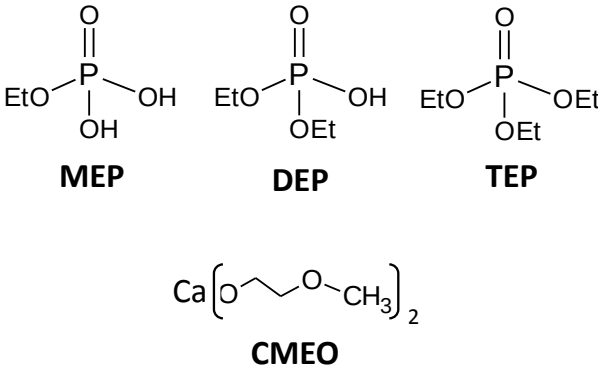

Scheme 1. Scheme of the Mono-, Di- and Tri-ethylphosphate (MEP, DEP and TEP), and the calcium 2-methoxyethoxide (CMEO).

2.3.1. Phosphorus (P) precursor characterization

We characterized the P precursor by ^{1}H and ^{31}P NMR spectroscopy (Figure 1). Being consistent with Ali et al. [17], we identified the formation of monoethylphosphate (MEP) and diethylphosphate (DEP) with traces of triethylphosphate (TEP) and H_3PO_4. The ^{1}H NMR spectrum (Figure 1A) showed two overlapped triplets centered at 1.3 ppm that represents the methyl groups (-CH_3) of the MEP and DEP respectively. The splitting of each peak in two refers to the coupling with the ^{31}P nuclei ($J^{4}_{1H\text{-}31P}$) and demonstrates that the -CH_3 were part of ethylphosphate molecules. The multiplet centered at 4.07 ppm refers to the methylene bridges (-CH_2-), and it is the result of the overlapping of two quadruplets associated to the MEP and DEP respectively. Again, each quadruplet is split in two due to the coupling with the ^{31}P nuclei.

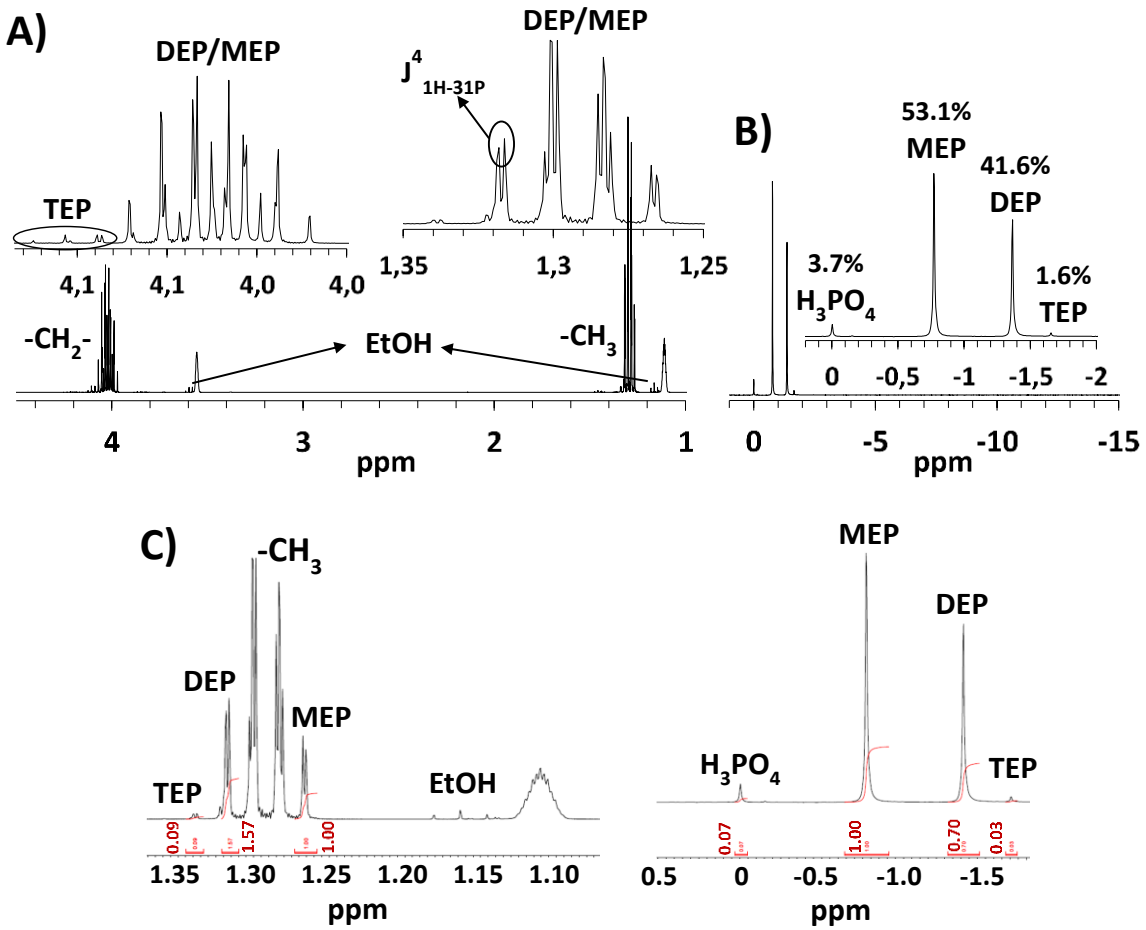

Figure 1. ^{1}H NMR **A)** and ^{31}P NMR **B)** spectra of the P precursor. Integrated intensities of the ^{1}H and ^{31}P NMR spectra **C)**. To compare ^{1}H and ^{31}P NMR integrated intensities, the ^{31}P NMR ones need to be multiplied by the number of ethoxides. Notice that the ^{31}P NMR integrated intensities contained a certain error due to the decoupling with the ^{1}H nuclei. Percentages in **B)** were calculated using the integrated intensities from **C)**.

The ^{31}P NMR spectrum (Figure 1B) of the P precursor showed the presence of two high abundant ^{31}P compounds, and traces of another two. ^{1}H and ^{31}P NMR integrated intensities (Figure 1C) indicates that the MEP was the most abundant compound followed by the DEP. The two less abundant compounds were associated to the TEP and H_3PO_4. We used the ^{1}H NMR integrated intensities to quantify the relative abundance of the MEP, DEP and TEP, and the ^{31}P NMR ones to quantify the H_3PO_4.

Notice that the ^{31}P NMR integrated intensities contained a certain error due to the decoupling with the ^{1}H nuclei.

2.3.2. Calcium (Ca) precursor characterization

The ^{1}H NMR spectrum of the Ca precursor showed two broad triplets and one broad singlet, associated to the $-CH_2-$ and $-CH_3$ of the calcium 2-methoxyetoxide (CMEO) respectively (Figure 2A). It has been reported this broadening effect for Ca^{2+} organic complexes due to the coordination of the oxygen atoms to a metallic center [18]. Unlike the P precursor (Figure 1C), here we could not differentiate between the CMEO and the solvent 2-methoxyethanol (MEOH). The addition of MEOH sharpened and shifted the ^{1}H NMR peaks instead of adding a new signal. The fast exchange CMEO/MEOH due to the ionic interaction Ca^{2+}/MEO^{-} could be the reason of observing the same signals for the two compounds [19]. To better elucidate the Ca precursor structure, we complemented the NMR analysis with mass spectrometry. The ESI-MS spectra (Figure 2B) revealed the formation of highly stable $[Ca(MEOH)_3]^{2+}$ and $[Ca(MEOH)_4]^{2+}$ complexes. These two complexes are consistent with the identification of hexa- and heptavalent calcium domains for the single crystal characterization of CMEO [20]. In such study [20] Goel et al. defined the formation of a bigger $[Ca_9(MEO)_{18}(MEOH)_2]$ cluster than those observed in the ESI-MAS spectrum. However, the DLS measurements of the Ca precursor (Figure 2C) showed an average complex size of ~5 nm, suggesting the formation of such big cluster in solution and that the ESI-MS measurement conditions disrupted it into smaller subunits. A relevant observation about the Ca precursor is its dark-orange color (Figure 2D). Electronic orbital transition energies between metal ions and alkoxides can result in the emission of certain colors. It has been described that the ligand-metal charge transfer

drives the orbital transitions into energies that absorb and emit at different wavelengths [21–23], which would explain the observed dark-orange color.

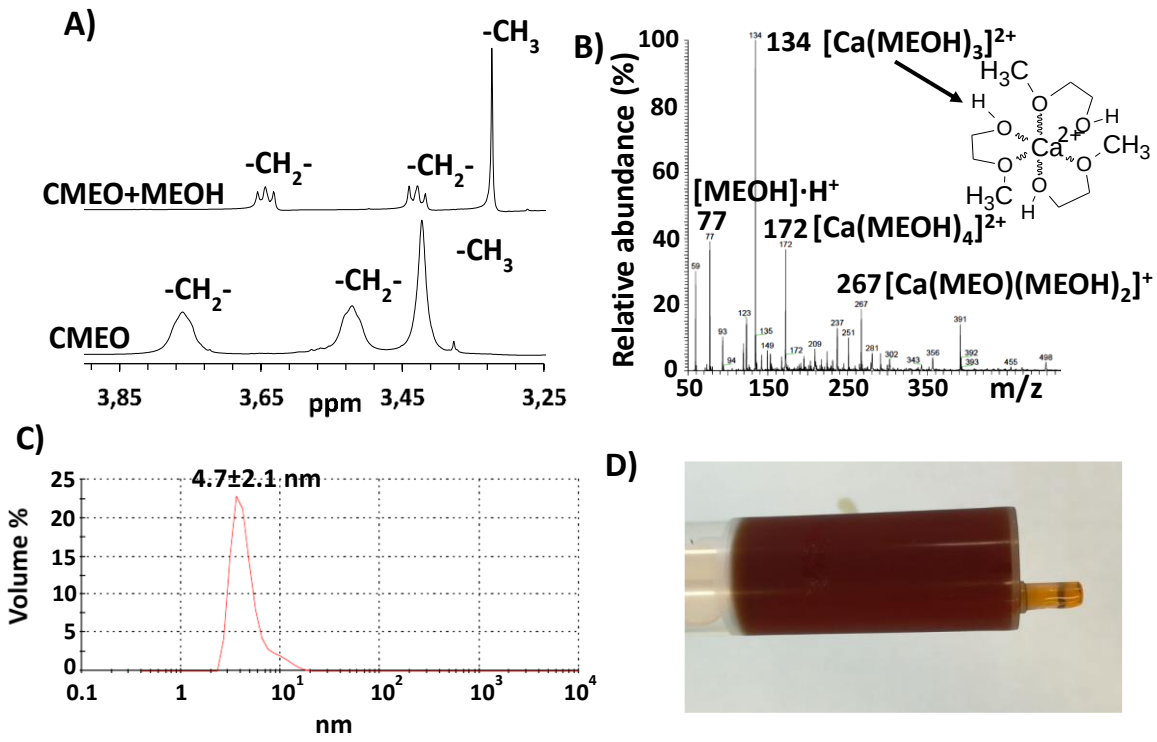

Figure 2. ^{1}H NMR spectra of the Ca precursor before (CMEO) and after the addition of MEOH (CMEO+MEOH) **A)**. ESI-MAS analysis **B)** and DLS measurements **C)** of the Ca precursor. Picture showing the dark-orange color of the Ca precursor **D)**.

2.3.3. P and Ca precursors interaction

We observed by ^{1}H and ^{31}P NMR spectroscopy (Figure 3A, 3B) a peak broadening and shielding of the MEP and DEP signals when the two precursors were mixed together (P+Ca). On the other hand, the peaks of the TEP remained unaltered and the ones from the CMEO became sharper (Figure 3C). All together indicates that the Ca^{2+} were

interacting with the free hydroxyl groups of the ethylphosphate molecules, forming a new complex.

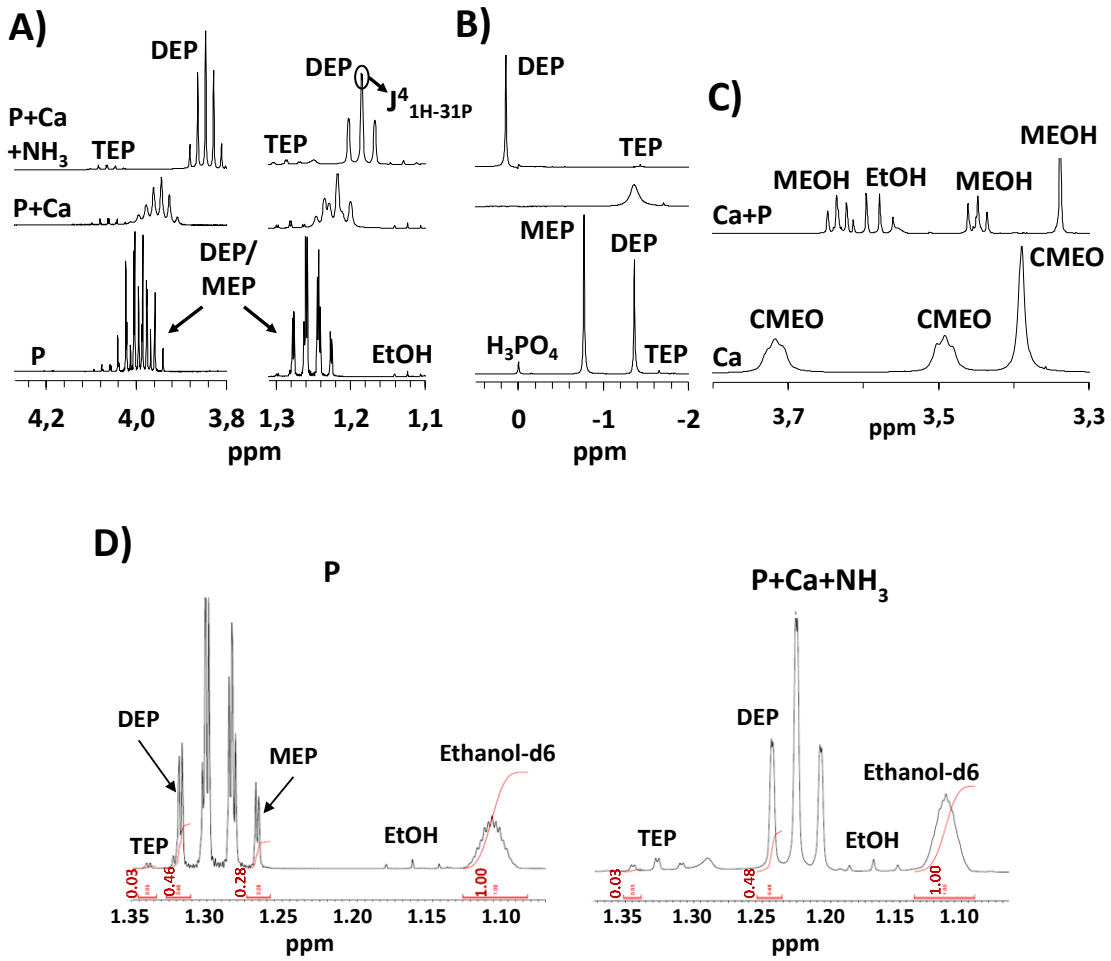

Figure 3. ^{1}H **A)** and ^{31}P **B)** NMR spectra of the P precursor, before (P) and after the addition of the Ca precursor (P+Ca), and the supernatant after the precipitation of particles by the addition of $NH_{3(aq)}$ (P+Ca+NH_3). ^{1}H NMR spectrum of the Ca precursor before (Ca) and after the addition of the P precursor (Ca+P) **C)**. Notice that the EtOH of Ca+P in **C)** came from the absence of P precursor purification in this specific analysis (section 2.2.3.). ^{1}H NMR integrated intensities of the P precursor (P) and the supernatant P+Ca+NH_3 **D)**.

DLS measurements supported the previous results, showing the disruption of the CMEO complex at ~5 nm and presenting a new one at ~1.8 nm (Figure 4A). We observed that the size of this new complex increased over time until the formation of particles or aggregates of ~1 µm after 30 h (Figure 4B). The addition of ammonia ($NH_{3(aq)}$) accelerated and increased the precipitation of particles. Integrated ^{1}H NMR intensities (Figure 3D) of the supernatant (P+Ca+NH_3) after the precipitation of particles by the addition of $NH_{3(aq)}$, showed the sole presence of DEP and TEP, indicating that only the MEP and the H_3PO_4 were incorporated into the particles. The lack of increase in the ethanol signal (Figure 3D) indicates the absence of hydrolysis or condensation of the ethylphosphates and the incorporation of the ethoxide groups into the particles.

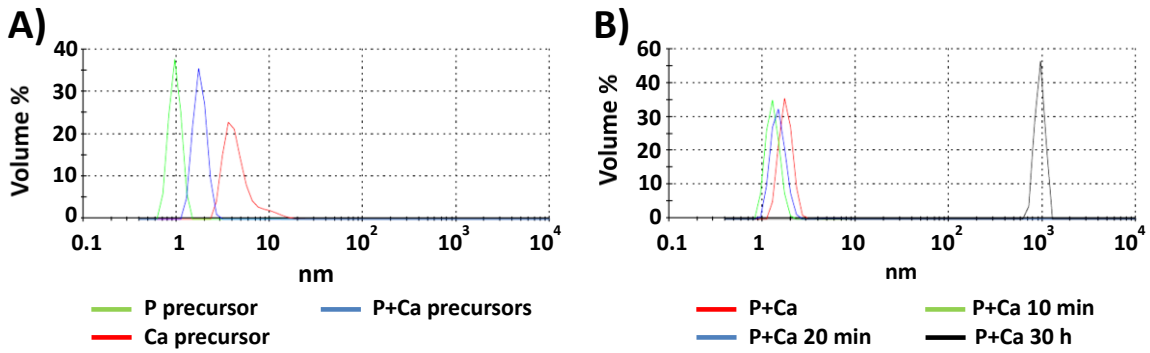

Figure 4. DLS measurements of the P and Ca precursors separately and together **A)**. P+Ca complex size evolution over time **B)**.

2.3.4. Precipitation of CPg nanoparticles

We synthesized particles with different P/Ca atomic ratios using different proportions of the P and Ca precursors (Table 1, 2). The particles were coded depending on their P content in ratio to the Ca one. We achieved particles with P contents ranging from 100% to 0%. Surprisingly, we needed huge volumes of the P precursor to obtain particles with

P>55%. The low mass yields for the P>55% particles suggest that their precipitation in an ethanolic environment was hindered. Regarding the amount of $NH_{3(aq)}$ used, we needed significantly smaller proportions to synthesize P100 and P65 particles, and, surprisingly, P55 particles were achieved by spontaneous precipitation. This indicates that the particles with P≥55% precipitated at lower alkaline conditions. Before thermal treatment, the particles contained a high amount of carbon (C), increasing this one with the P content. This was consistent with the incorporation of MEP into the particles (Figure 3D). After thermal treatment, the C content and the weight of the particles significantly decreased, suggesting the decomposition of the ethoxide groups. However, P30 and P0 particles maintained a significant C amount with a mass increase for P0 after thermal treatment. Before thermal treatment, The P100 particles contained a high N amount, suggesting the formation of ammonium phosphate salts. The P/Ca ratio of the particles was practically the same after thermal treatment, showing the absence of phosphate decomposition at such temperatures [24]. On the other hand, the P100 particles decomposed to a brown paste at 200 ºC.

Table 1. Particle synthesis conditions, yields and mass loss after thermal treatment.

	P:Ca precursors (mL)	EtOH:$NH_{3(aq)}$:H_2O (mL)	Yield (mg)	Mass loss (%)
P100	10:0	90:1.7:10	127	Decomposed (200 °C)
P65	8.5:1.5	90:1.9:6	359	-26.9 (200 °C)
P55	4:6	90:0:0	718	-25.96 (200 °C)
P30	1.5:8.5	90:30:0	948	-23.24 (350 °C)
P0	0:10	90:30:0	781	+19.59 (350 °C)

Table 2. Particle composition before **A)** and after thermal treatment **B)**. P/Ca atomic % measured by EDS. C and N mass % measured by EA.

A)	**P/Ca (atomic %)**	**C (mass %)**	**N (mass %)**
P100	100/0	0.80	12.63
P65	63.9/36.1	17.13	≤0.2
P55	54.1/45.9	15.81	≤0.2
P30	28.7/71.3	9.77	≤0.2
P0	0/100	3.15	≤0.2

B)	**P/Ca (atomic %)**	**C (mass %)**	**N (mass %)**
200°C	Decomp.	-	-
200°C	62.9/37.1	0.34	≤0.2
200°C	56.5/43.5	0.37	≤0.2
350°C	29.8/70.2	5.66	≤0.2
350°C	0/100	7.74	≤0.2

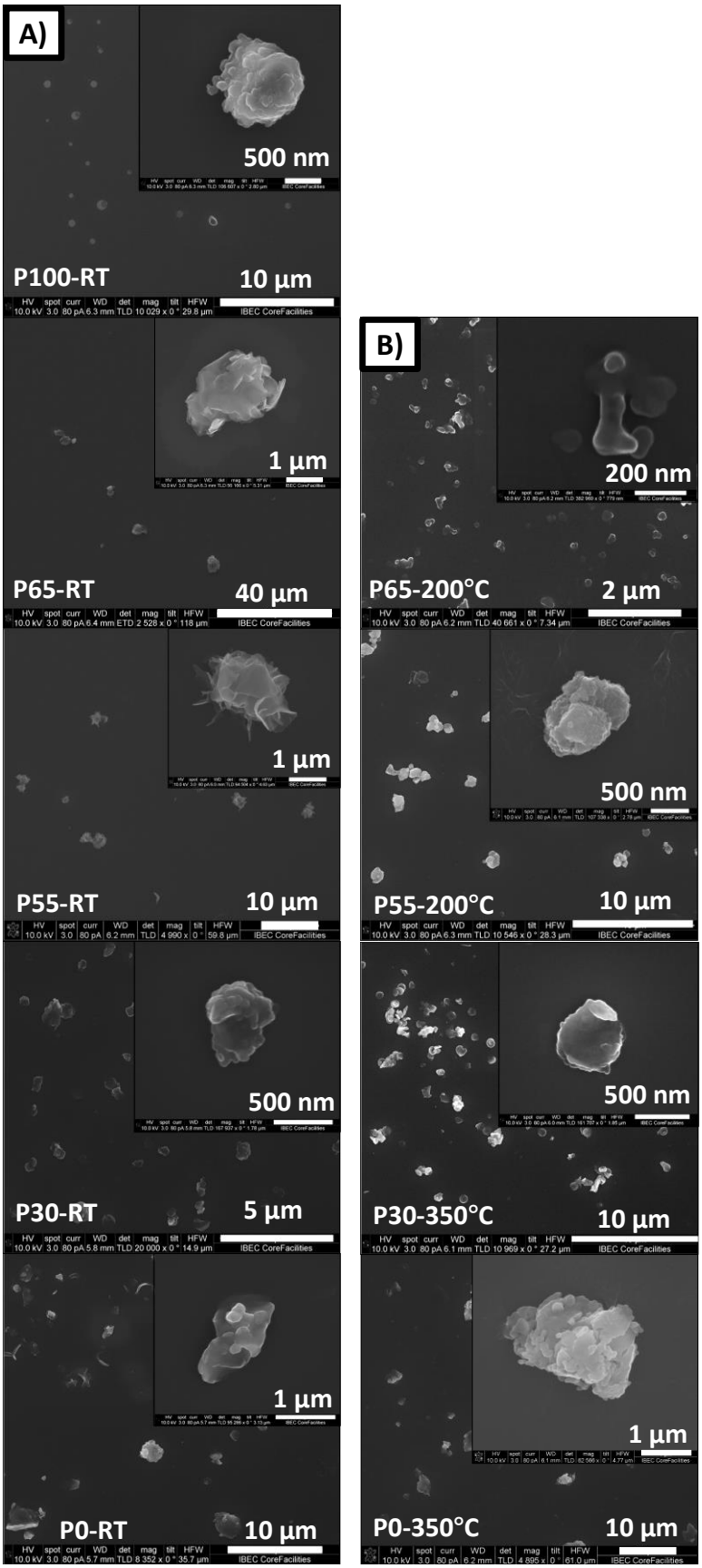

Figure 5. FE-SEM images of the particles before **A)** and after thermal treatment **B)**.

FE-SEM images of the particles (Figure 5) showed aggregates ranging from several hundreds of nm to few µm. The aggregates seemed to be composed by smaller particles of few nm in size. The formation of aggregates suggests a low particle electrostatic repulsion, attributed to small surface Z-potentials. All compositions showed a spherical-like shape except for P65 and P55 particles whose morphology resembled to those of faceting-like structures. After thermal treatment, all compositions had a similar spherical-like shape. We did not observe significant changes in the aggregate size for the different compositions before and after thermal treatment.

2.3.5. CPg nanoparticles characterization

2.3.5.1. X-ray diffraction analysis

X-ray diffraction showed the formation of portlandite for P30 and P0 particles (Figure 6A). This indicates that existed a Ca excess for the particles with P≤30% that precipitated in form of $Ca(OH)_2$. On the other hand, we observed the formation of crystalline $NH_4H_2PO_4$ for P100 particles, which was consistent with the N detected in the EA analysis (Table 2A). That shows up that in the absence of Ca^{2+}, the $NH_{3(aq)}$ added to precipitate the particles was incorporated as a counterion. Separately, we detected for P30, P55 and P65 particles an unidentified peak (marked with a star) at the left side of the spectrum. The increase of this peak intensity with the P content suggests that it might be related to some crystalline diffraction plane of calcium MEP, since we identified by ^1H NMR spectroscopy the sole incorporation of MEP (with a small amount of H_3PO_4) in the particles (Figure 3D).

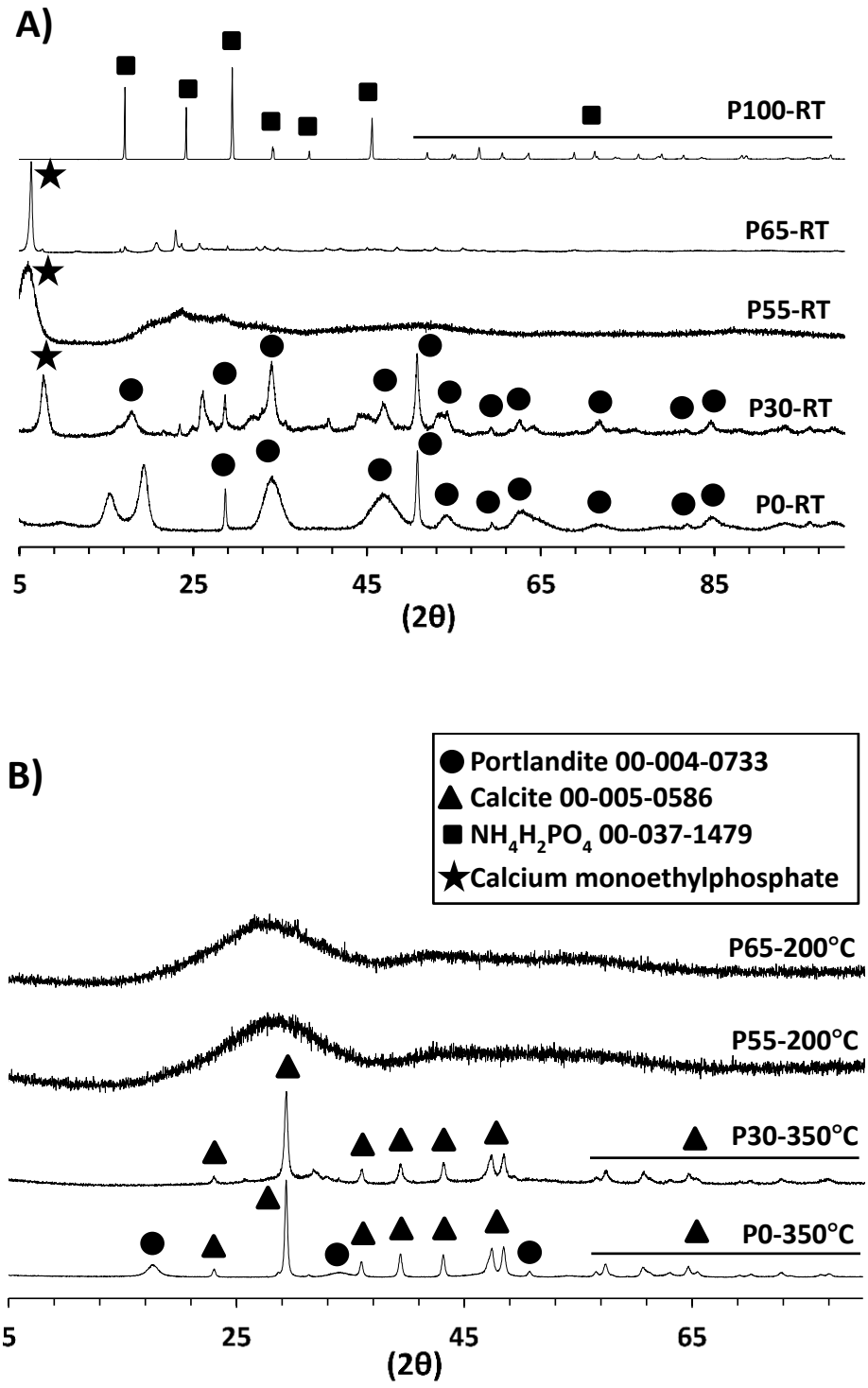

Figure 6. X-ray diffraction spectra of the particles before **A)** and after thermal treatment **B)**.

After thermal treatment (Figure 6B), we observed the carbonatation of the portlandite of the P30 and P0 particles to calcite. Although there were still traces of portlandite in the P0 particles, a minimum temperature of 350 ºC was enough for most of the conversion. The formation of calcite ($CaCO_3$) justifies the high amount of C detected for P30 and P0 particles in the EA analysis (Table 2B). As previously mentioned, we inferred that P100 particles probably decomposed to $NH_{3(g)}$ and $H_3PO_{4(l)}$ at 200 ºC. We observed a complete amorphous structure for P55 and P65 particles, suggesting the formation of CPg phases [25–27]. The unidentified peak (marked with a star), which we attributed to calcium MEP, was not observed anymore, being consistent with the decomposition of ethoxides at 200 ºC (Table 2B). We would like to highlight that the presence of P by EDS (Table 2B) and the absence of CP crystalline structures [24,28–30] before and after thermal treatment, indicates the existence of amorphous CP compounds for all the particles containing P.

2.3.5.2. ^{31}P MAS NMR spectroscopy

The ^{31}P MAS NMR spectra of the particles before thermal treatment showed the sole presence of orthophosphate (Q^0) units (Figure 7A) [4]. The only detection of Ca and P by EDS (Table 1) lead us to the conclusion that these orthophosphates were in form of CP. The peaks were narrow indicating a high mobility of the ^{31}P nucleus. This high mobility is commonly observed in crystalline CP structures [31]. However, we did not identify any crystalline CP phase in the X-ray diffraction spectra (Figure 6A). We hypothesize that the existence of ethoxide groups disrupted the CP crystalline periodicity but still allowed a high nuclei mobility. On the other hand, the P55 particles showed significant wider peaks, distinctive of chemical structures with low mobility and high connectivity, like amorphous ones [4,31]. Returning to the X-ray diffraction spectra

(Figure 6A), we observed that the P55 particles had an amorphous pattern. The spontaneous precipitation of P55 particles without the addition of $NH_{3(aq)}$ in the synthesis process (Table 1), may have affected somehow in the CP structure. Another possibility is that the absence of well-ordered structures like portlandite or $NH_4H_2PO_4$ in the particles (Figure 6A) had also an effect on the amorphicity of the CP phase.

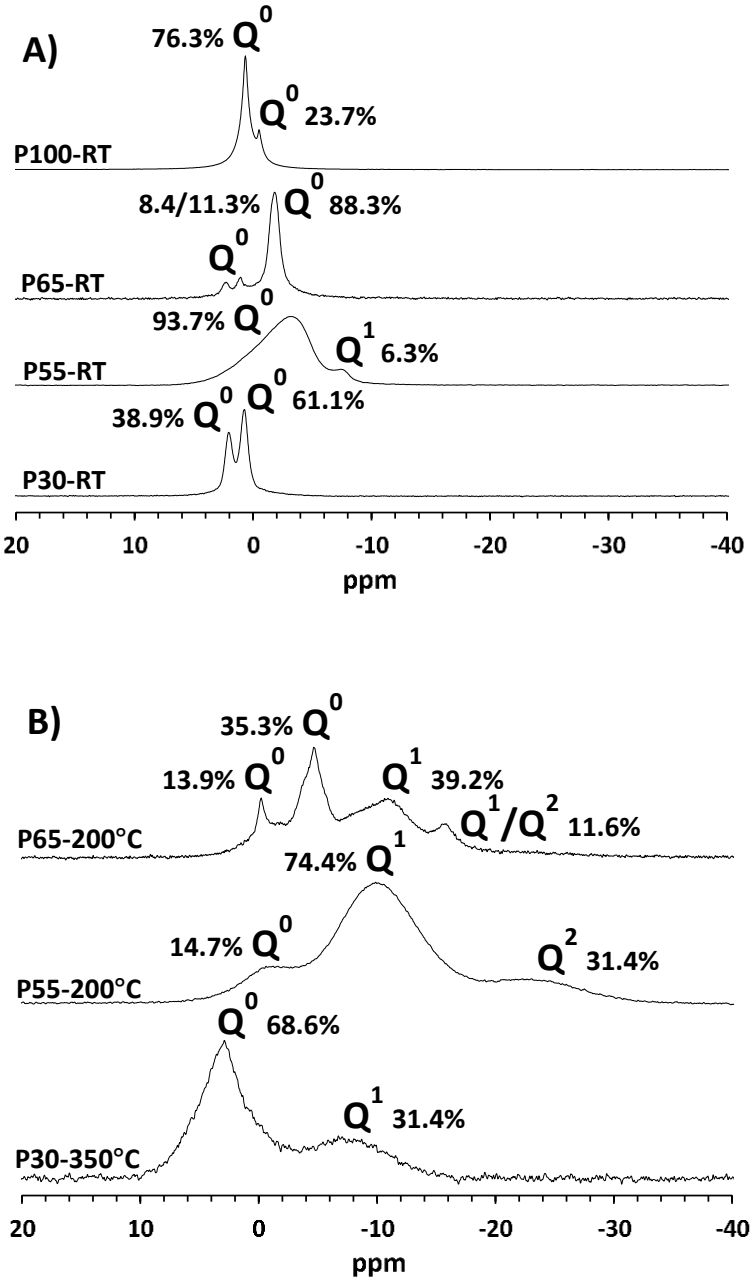

Figure 7. ^{31}P MAS NMR spectra of the particles before **A)** and after thermal treatment **B)**. Relative peak abundance and chemical shifts in Table 3.

Table 3. ^{31}P MAS NMR (Figure 7) chemical shifts, peak assignment and relative abundance of the particles before **A)** and after the thermal treatment **B)**.

A)	Chemical shift (ppm)	Assignment	Relative abundance (%)
P100-RT	0.64	Q^0	76.26
	-0.52	Q^0	23.74
P65-RT	2.27	Q^0	8.41
	1.06	Q^0	11.26
	-1.83	Q^0	80.33
P55-RT	-3.13	Q^0	99.74
	-7.40	Q^1	6.26
P30-RT	2.06	Q^0	38.92
	0.73	Q^0	61.08

B)	Chemical shift (ppm)	Assignment	Relative abundance (%)
P65-200°C	-0.22	Q^0	13.90
	-4.67	Q^0	35.29
	-10.92	Q^1	39.18
	-15.85	Q^1/Q^2	11.62
P55-200°C	-1.31	Q^0	14.74
	-9.89	Q^1	74.35
	-23.05	Q^2	10.91
P30-350°C	2.89	Q^0	68.64
	-8.05	Q^1	31.36

In addition, we identified in the ^{31}P MAS NMR spectra (Figure 7A) a small amount of pyrophosphates (Q^1) for the P55 particles [24]. This small phosphate condensation probably affected in the amorphicity of the particles since condensed phosphate units will tend to decrease atomic mobility.

After thermal treatment, we observed the formation of Q^1 and Q^2 units increasing those with the P content of the particles (Figure 7B) [4,32]. We also observed wide peaks characteristic of amorphous structures. The Q^1 units for the P30 particles were assigned to pyrophosphates, however, the presence of Q^2 units for the P55 particles, indicates the formation of metaphosphates [24]. The high amount of Q^1 units for P55 particles suggests that the metaphosphates were in form of open-chained trimetaphosphates [32,33]. All together indicates that a thermal treatment at 200 ºC was enough to induce the condensation of the orthophosphate units. We hypothesized that the presence of ethoxides may have favored such condensation. It is evident that the amount of Ca^{2+} difficulted the phosphate condensation due to the good affinity of Ca^{2+} with the phosphate oxygen atoms. Surprisingly, P65 particles showed narrower peaks and a less phosphate

condensation rate even having the highest P content. This suggests that low amounts of Ca^{2+} destabilized the condensed phosphate interactions or increased the phosphate condensation temperature above 200 ºC (however, we do not discard a possible oven irreproducibility). Regarding the amount of Ca^{2+}, we observed (and it can also be observed before thermal treatment but not so precisely) a deshielding of the ^{31}P nuclei as the Ca^{2+} content of the particles increased. Comparison with other CPg in the bibliography showed that our particles had a lower phosphate condensation rate. Reported CPg are mainly composed by Q^2 units [25,32]. However, the amount of Ca^{2+} for these glasses is usually inferior, allowing a higher phosphate condensation. Therefore, the phosphate condensation of the current synthesized particles decreased due to a higher Ca^{2+} content.

2.3.5.3. ATR-FTIR spectroscopy

Being consistent with X-ray diffraction analysis (Figure 6A), ATR-FTIR spectroscopy of the particles before thermal treatment (Figure 8A) showed the formation of $Ca(OH)_2$ and $NH_4H_2PO_4$ for P0 and P100 particles respectively. The other particles exhibited the characteristic sharp bands of well-ordered crystalline CP structures (v_4(OPO) bending, v_1(PO) symmetric stretching and v_3(PO) antisymmetric stretching modes) [28–30] plus some extra bands. TEP (Figure 9D) and ethanol IR spectra from database [34,35] suggest that these extra bands were originated from the vibration of the ethoxide groups present in the particles; v_s(C-C-O) symmetric stretching, v_{as}(C-C-O) antisymmetric stretching, v(CH) [4] and other unidentified bands. The emission of some of these extra bands at similar frequencies than the CP ones made difficult in some cases to differentiate them due to overlapping.

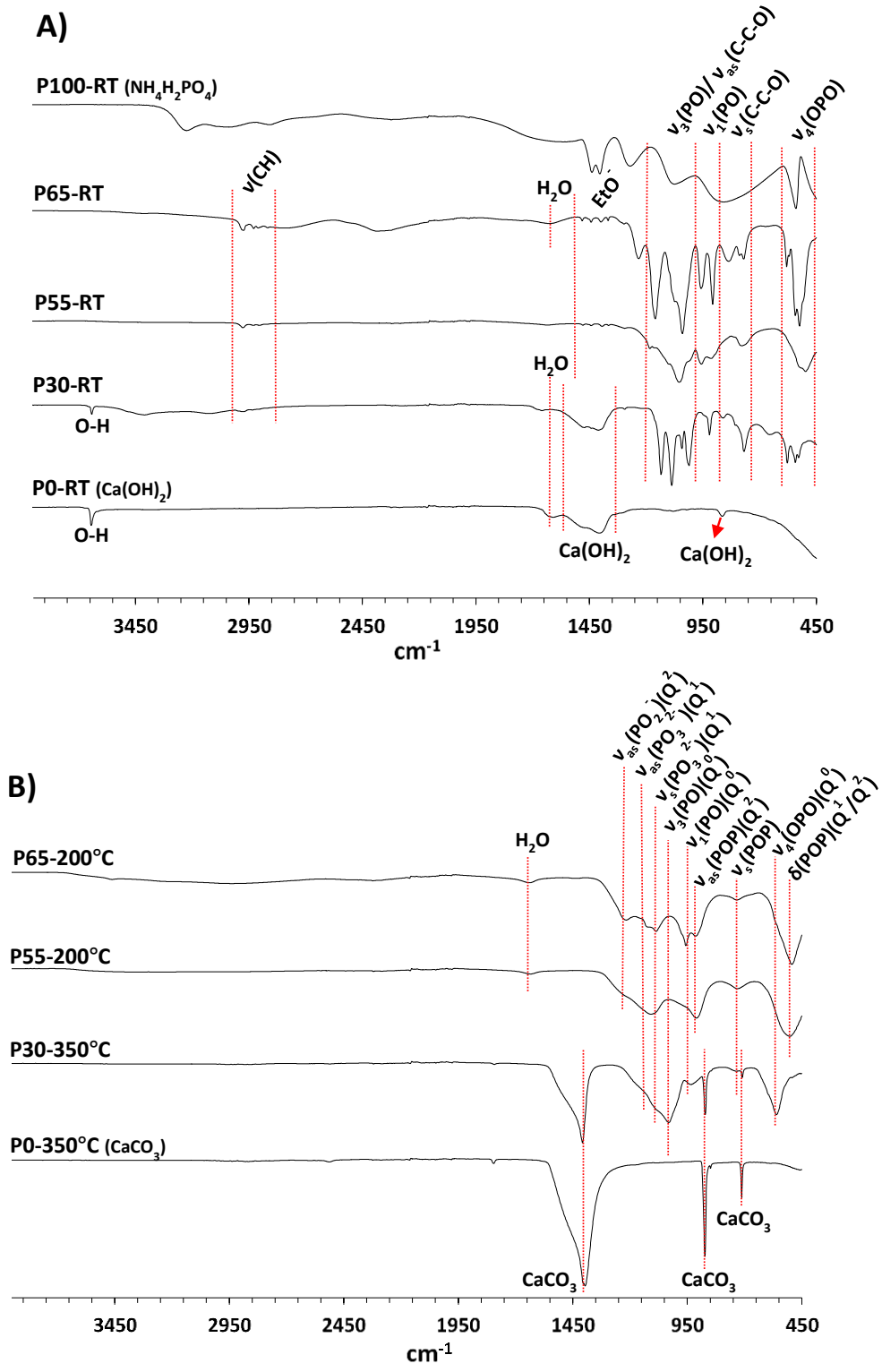

Figure 8. ATR-FTIR spectra of the particles before **A)** and after thermal treatment **B)**.

For exact frequency values and information about band assignment please refer to

Table 4 and Figure 9.

Table 4. ATR-FTIR (Figure 8) band assignment and frequencies (cm^{-1}) of the particles before **A)** and after thermal treatment **B)**.

A)	**P65-RT**	**P55-RT***	**P30-RT**
ν_4(OPO) (Q^0)[28-30] **/δ(POP)**(Q^1)*[4-36]	525, 542; 569, 583	500, 528	532, 546; 581
$\delta(OH^-)$[29,35]			659
Org. (Figure 9D) **/ν_s(POP)** (Q^1)*[4,36]	775; 793	777, 790	772
ν_s(C-C-O)[34]	840	824	812
$Ca(OH)_2$ (Figure 9B)			865
/ν_1(PO)(Q^0)[28-30]	908; 959	917; 958	925; 952
ν_3(PO)(Q^0)[28-30] **/ν_{as}(C-C-O)**[34] **/$\nu_{s,as}(PO_3^{2-})$**(Q^1)*[4,36]	1041, 1078, 1163	1019, 1057, 1104, 1187	1014; 1047, 1090; 1137
EtO- (Figure 9D)	1235	1296	1298
EtO- (Figure 9D)[34]	1371, 1396, 1447, 1483	1369, 1406, 1450, 1483	
$Ca(OH)_2$ (Figure 9B)			1412, 1445, 1476
$\delta(H_2O)$[28-30]	1633		1662
ν(CH)[4,24,34]	2869, 2909, 2930, 2975	2877, 2905, 2933, 2979	2978
$Ca(OH)_2$ (Figure 9B)			3645

B)	**P65-200°C**	**P55-200°C**	**P30-350°C***
δ(P-O-P)(Q^1*,Q^2)[4,36] **/ν_4(OPO)**(Q^0)[28-30]	493	503	563
$CaCO_3$ (Figure 9C)			713
ν_s(POP) (Q^1*,Q^2)[4,36]	730	736	743
$CaCO_3$ (Figure 9C)			875
ν_{as}(POP)(Q^2)[4,36]	910	915	
ν_1(PO)(Q^0)[28-30]	956	957	936
$\nu_s(PO_3^{2-})$(Q^1)[4,36] **/$\nu_3(PO_4^{3-})$**(Q^0)[28-30]	1085	1115	1034, 1078
$\nu_{as}(PO_3^{2-})$(Q^1)[4,36] **/$\nu_3(PO_4^{3-})$**(Q^0)[28-30]	1120	1115	1078, 1156
$\nu_{as}(PO_2^-)$(Q^2)[4,36]	1215	1203	
$\delta(H_2O)$[28-30]	1633	1643	
$CaCO_3$ (Figure 9C)			1411

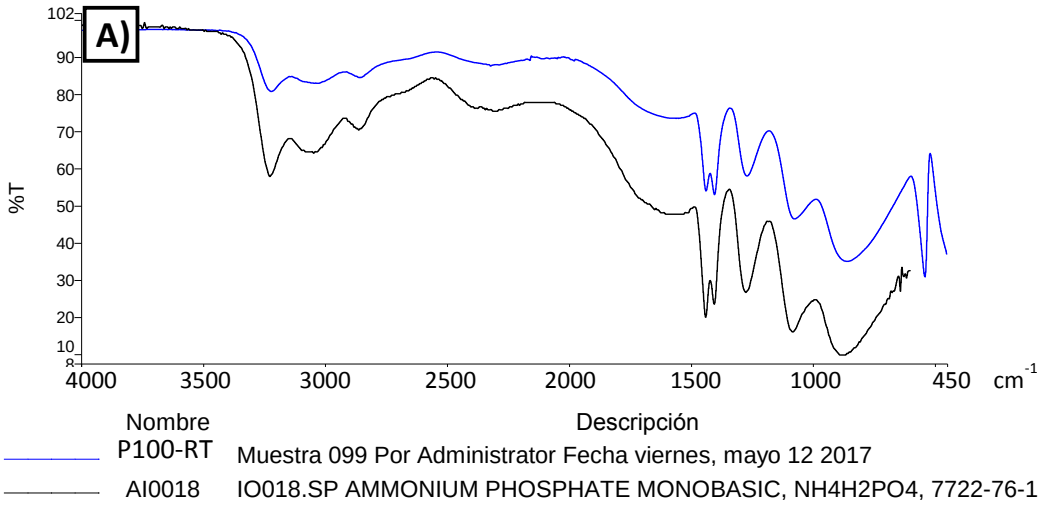

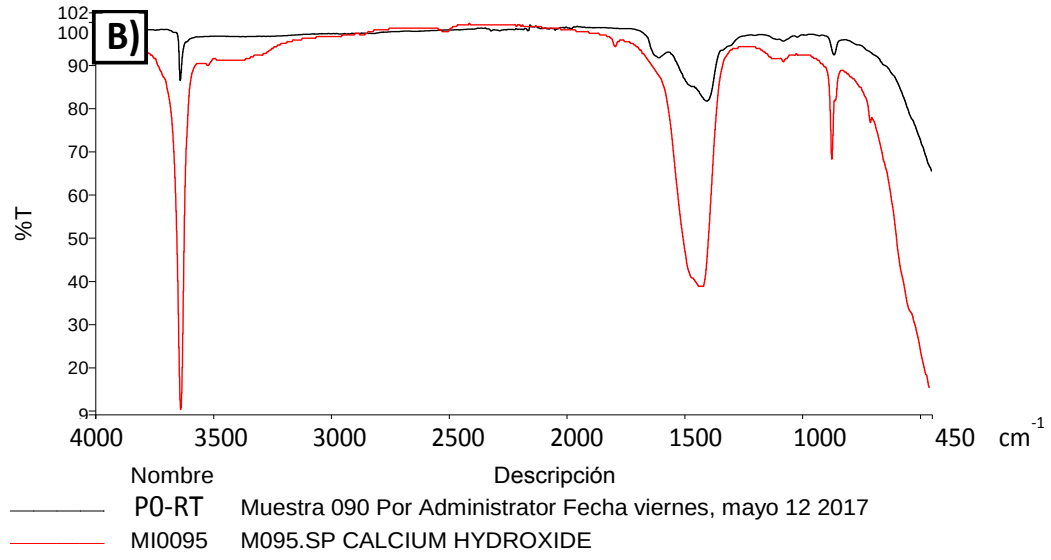
B)
%T
102
100
90
80
70
60
50
40
30
20
0
4000
3500
3000
2500
2000
1500
1000
450
cm-1
Nombre
Descripción
P0-RT Muestra 090 Por Administrator Fecha viernes, mayo 12 2017
MI0095 M095.SP CALCIUM HYDROXIDE

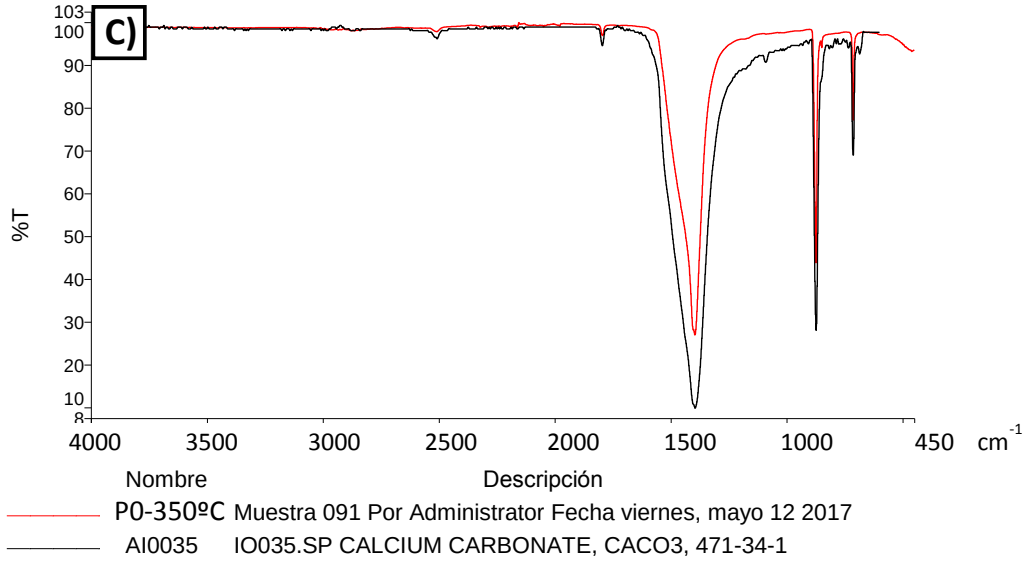
C)
%T
103
100
90
80
70
60
50
40
30
20
10
8
4000
3500
3000
2500
2000
1500
1000
450
cm-1
Nombre
Descripción
P0-350ºC Muestra 091 Por Administrator Fecha viernes, mayo 12 2017
AI0035 IO035.SP CALCIUM CARBONATE, CACO3, 471-34-1

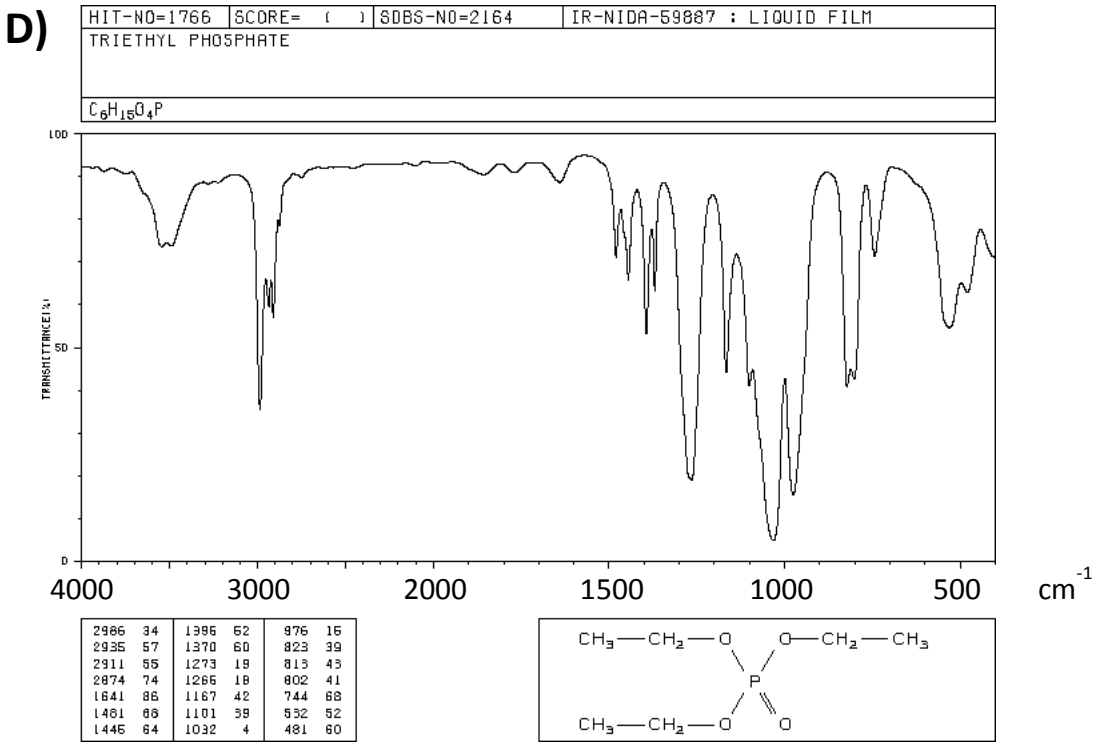

Figure 9. Comparison of the P100-RT **A)**, P0-RT **B)** and P0-350ºC **C)** ATR-FTIR spectra (Figure 8) with the ©2005-2008, Fiveash Data Management, Inc. (PerkinElmer) database. Triethylphosphate FTIR spectrum from online SDBS database [35], showing some of the bands assigned to the ethoxide groups (EtO-) (Table 4A) **D)**.

The identification of Q^1 units for P55 particles (Figure 7A) means that some of its IR bands were originated from the vibration of condensed POP bonds. An interesting observation regarding the P30 and P65 particles is the presence of two different double v_4(OPO) bands at ~530 and ~580 cm^{-1}. This suggests the presence of two different phosphate compounds associated to a possible incorporation of DEP, which could also justify some of the observed extra bands. As we identified in the ^{31}P MAS NMR spectra (Figure 7A), P55 particles exhibited broader bands than P65 and P30 particles, indicating lower atomic mobility and a more disordered structure [36].

In agreement with X-ray diffraction analysis (Figure 6B), we observed the formation of $CaCO_3$ for the thermally treated P0 and P30 particles in the ATR-FTIR spectra (Figure 8B). After thermal treatment, all particles showed much broader bands, characteristic of amorphous CP structures [4,36]. We did not observe the extra bands assigned to the ethoxides any more, confirming their decomposition at 200 ºC. The apparition of Q^2 units, the increase of the Q^1 ones and the decrease of the Q^0 band intensities indicates a higher phosphate condensation for P65 and P55 than for P30 particles. In agreement with the ^{31}P MAS NMR results (Figure 7B), the ATR-FTIR spectrum of the P65 particles showed slightly sharper bands indicating a lower connectivity in the CPg structure. The absence of O-H bands at ~3400 cm^{-1} [4,28,29] before and after thermal treatment indicates the almost absence of absorbed moisture and that all free phosphate oxygens were interacting with Ca^{2+}.

2.3.5.4. ^{1}H NMR characterization of the organic material

To identify the type of organics present in the particles, we dissolved the particles in acidic D_2O and run a ^1H NMR. The spectra of the dissolved particles before thermal treatment (Figure 10A), showed the presence of one single ethoxide, being consistent with the incorporation of only MEP (Figure 3D). We also detected for P55 and P30 particles the presence of a minor amount of another ethylphosphate, which we attributed to the incorporation of a minor amount of DEP. The presence of DEP, apart from MEP, and the incorporation of traces of H_3PO_4 in the particles (Figure 3B) justify the identification of several Q^0 units and a double v_4(OPO) vibration band in the ^{31}P MAS NMR and ATR-FTIR spectra respectively (Figure 7A, 8A). The almost absence of ethanol

in the ^{1}H NMR spectra of the dissolved particles (Figure 10A) indicates a high stability of the MEP under acidic conditions [24].

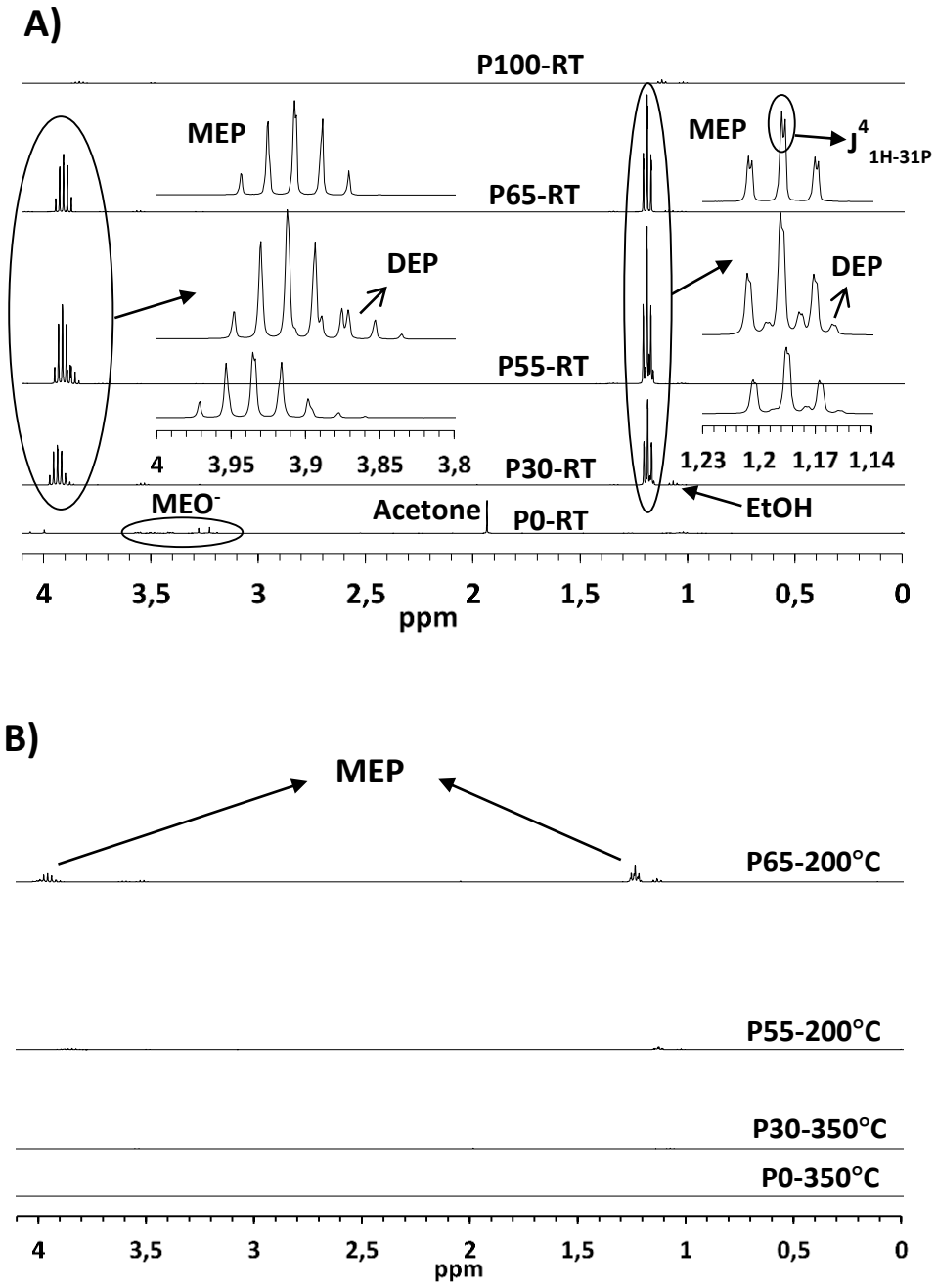

Figure 10 ^{1}H NMR spectra of the dissolved particles before **A)** and after thermal treatment **B)** in acidic D_2O, showing the presence of organics. The acetone identified for P0-RT in **A)** is attributed to impurities from NMR tube cleaning.

We also observed a high stability of the DEP and TEP under alkaline conditions in the particle synthesis process (Figure 3D). This high pH stability indicates that the ethylphosphate condensation is impaired under acidic/alkaline conditions and it only occurs at moderately high temperatures (200 ºC). We did not observe the presence of other organics in the particles except for P0 that contained traces of MEO^-. After thermal treatment, the particles were completely inorganic (Figure 10B) except for a tiny amount of ethoxide in P65 particles. This tiny amount is consistent with the lower phosphate condensation rate observed for P65 than for P55 after thermal treatment (Figure 7B,), despite having P65 a higher P content, and suggests that low Ca^{2+} contents increased the needed phosphate condensation temperature above 200 ºC. We also run a ^{31}P NMR of the dissolved particles in acidic D_2O (Figure 11). Surprisingly, the condensed phosphate units of the thermally treated particles were stable at acidic pH and could be detected. This finding highlights liquid ^{31}P NMR as an alternative to the more expensive and higher sample consuming solid ^{31}P MAS NMR to characterize phosphate glasses. We considered the relative abundances of the ^{31}P NMR spectra (Table 5) more precise than the ^{31}P MAS NMR ones (Table 3) due to their better spectra resolution. The ratio of the different Q^n units was similar than in the ^{31}P MAS NMR analysis (Table 3) except for P65 that this time did not show a lower phosphate condensation rate than the P55 particles (Table 5). However, the particles batch used here was different than the one used in the ^{31}P MAS NMR. The different batch origin contemplates the possibility that an irreproducibility in the oven temperature was the cause of observing a lower phosphate condensation rate for P65 in the ^{31}P MAS NMR spectra (Figure 7B). The high amount of Q^1 units for P65 particles in the ^{31}P NMR spectra (Table 5) suggests the formation of trimetaphosphates rather than longer metaphosphates [33,37]. Notice that the $Q^2/Q^1>1/2$ indicates the formation of cyclic trimetaphosphates for P65 particles.

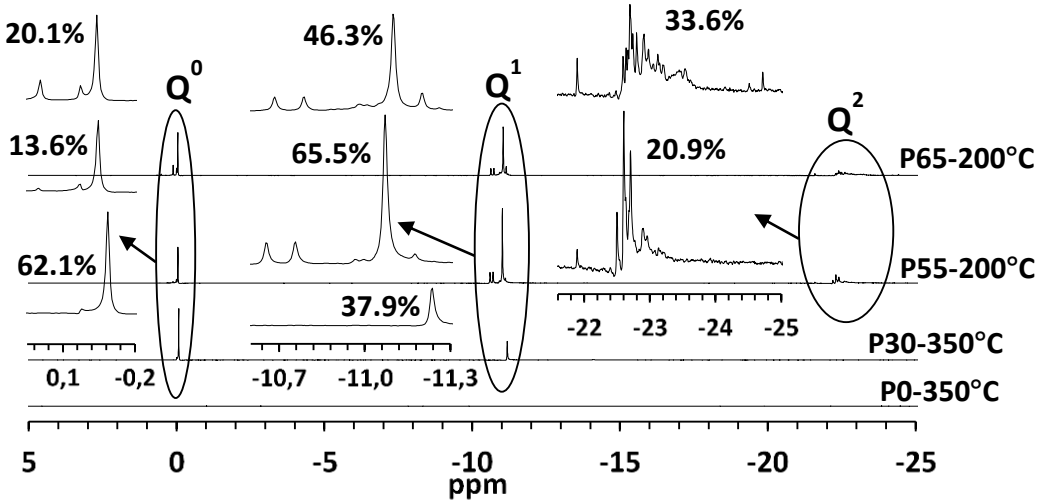

Figure 11. ^{31}P NMR spectra of the dissolved thermally treated particles in acidic D_2O, showing the presence of condensed phosphate units (Q^n). Chemical shifts, relative abundance and peak assignment in Table 5.

Table 5. Chemical shift, Q^n unit, relative abundance and compound assignment of the ^{31}P NMR spectra (Figure 11) of the thermally treated particles in acidic D_2O. Cyclic ($P_3O_9^{3-}$) and open chained ($P_3O_{10}^{5-}$) trimetaphosphate, pyrophosphate ($P_2O_7^{4-}$) and amorphous calcium phosphate (ACP).

	Chemical shift (ppm)	Q^n unit	Relative abundance (%)	Assignment
P65-200°C	(0.51)-(-0.04)	Q^0	20.12	ACP[31]
	(-10.63)-(-11.21)	Q^1	46.28	($P_3O_{10}^{5-}$/$P_2O_7^{4-}$)[32,33]
	(-21.59)-(-24.42)	Q^2	33.6	($P_3O_9^{3-}$/$P_3O_{10}^{5-}$)[32,33]
P55-200°C	(0.12)-(-0.05)	Q^0	13.62	ACP[31]
	(-10.6)-(-11.13)	Q^1	65.53	($P_3O_{10}^{5-}$/$P_2O_7^{4-}$)[32,33]
	(-21.59)-(-22.83)	Q^2	20.85	($P_3O_9^{3-}$/$P_3O_{10}^{5-}$)[32,33]
P30-350°C	(0.00)-(-0.07)	Q^0	62.12	ACP[31]
	-11.19	Q^1	37.89	($P_2O_7^{4-}$)[32,33]

Summarizing the particle characterization section, we achieved before thermal treatment the formation of amorphous calcium MEP with the formation of portlandite or $NH_4H_2PO_4$ when there was an excess or the absence of Ca^{2+} respectively. We could not obtain particles with P≥65% probably due to the high solubility of the calcium DEP in ethanol. The use of more apolar solvents than EtOH in the synthesis process may favor their precipitation. After treating the particles at 200 ºC, we observed a decomposition of the ethoxide groups and a condensation of the orthophosphate units, being higher the condensation as lower was the Ca^{2+} content. We achieved for P65-200ºC and P55-200ºC particles, cyclic (Q^2) and open chained (Q^2/Q^1) amorphous calcium trimetaphosphate (ACTMP) with traces of amorphous calcium pyrophosphate (ACPP) (Q^1) and amorphous calcium phosphate (ACP) (Q^0) [31–33]. In the bibliography, CPg are mainly composed by Q^2 units due to their lower Ca^{2+} content [4,32]. Therefore, P65-200ºC and P55-200ºC should be considered as low-condensed CPg since they have $Q^1>Q^2$. As the Ca^{2+} content of the particles increased, the amount of ACTMP decreased until the predominant phase was ACP for P30-350ºC particles. It was necessary a thermal treatment at 350 ºC to convert most of the portlandite to calcite. The $NH_4H_2PO_4$ decomposed at 200 ºC probably to $NH_{3(g)}$ and $H_3PO_{4(l)}$.

2.3.6. Bioactive degradation of the CPg nanoparticles

We immersed the particles in buffered HEPES medium at pH 7.4 and 37 ºC to measure their ion release in physiological-like conditions. Phosphate buffers were avoided to prevent the precipitation of $CaHPO_4$. Apart from measuring the ion release over two weeks, we also measured possible pH alterations (Figure 12). Before thermal treatment, the particles were very soluble releasing high amounts of Ca^{2+} during 3 days (Figure

12A). The further stabilization of the [Ca^{2+}] and the absence of particles after the experiment (Figure 13) confirmed the high solubility of the particles at physiological conditions. We attribute this high solubility to the presence of ethoxides, which probably disrupted the CP chemical lattice making it less stable and more soluble. The absence of inorganic phosphate (Pi) release (Figure 12B) is attributed to the release of MEP instead, which was not detected by the malachite green colorimetric method (section 2.2.11.) [16]. P100 particles released high amounts of Pi because of the dissolution of inorganic $NH_4H_2PO_4$. Although the dissolution of similar CP particles did not show cytotoxicity in previous studies [3,10,11], the high stability of MEP under acidic conditions (Figure 10A) justifies further studies of how this molecule is metabolized in the body.

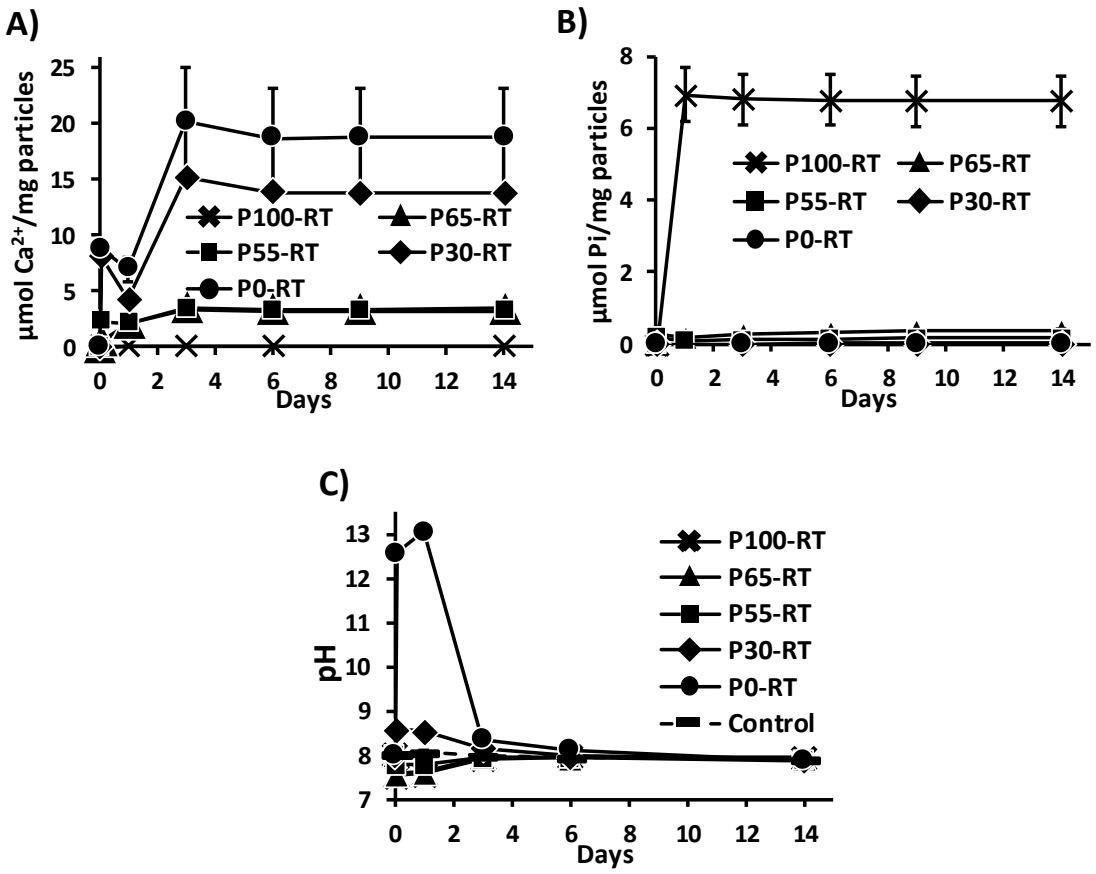

Figure 12. Cumulative Ca^{2+} **A)** and Pi **B)** release and pH changes **C)** after the immersion of the thermally untreated particles, in HEPES media (pH 7.4) at 37 ºC. Media was replaced every time point.

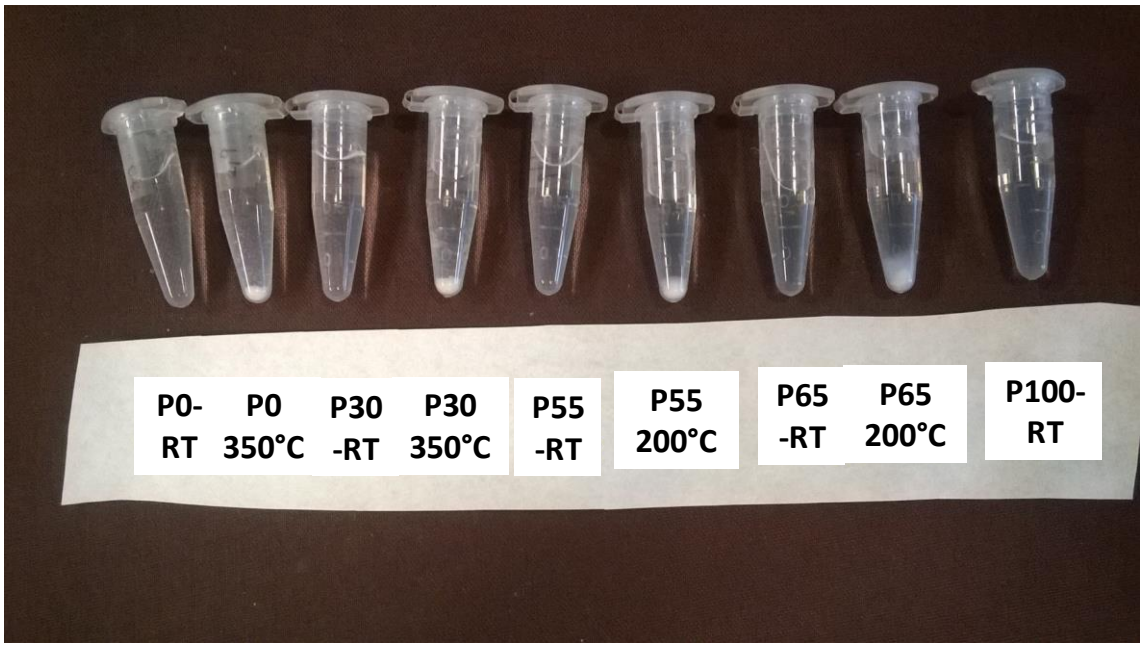

Figure 13. Microcentrifuge tubes containing the particles after two weeks immersed in buffered HEPES media at pH 7.4 and 37 ºC.

There were not significant changes in the pH except for P0 that extremely basified the media due to the dissolution of portlandite (Figure 12C). This strong basification may limit their use as a biological Ca^{2+} source. On the other hand, the rest of the particles did not alter significantly the pH, making them ideal to release high physiological Ca^{2+} amounts in short periods. Initial Ca^{2+} concentration increases have demonstrated to favor several biological responses for tissue repair such as cell migration, attachment and, proliferation, osteogenesis and angiogenesis [2,3,9,10]. If compared with conventional CPg or degradable CP ceramics, the Ca^{2+} release profile of these organically modified particles was faster, suggesting their use to induce earlier biological responses [37–39]. P100 particles can be useful to release high amounts of Pi in short periods without pH modifications but considering the effects of simultaneously releasing substantial NH_4^+ amounts.

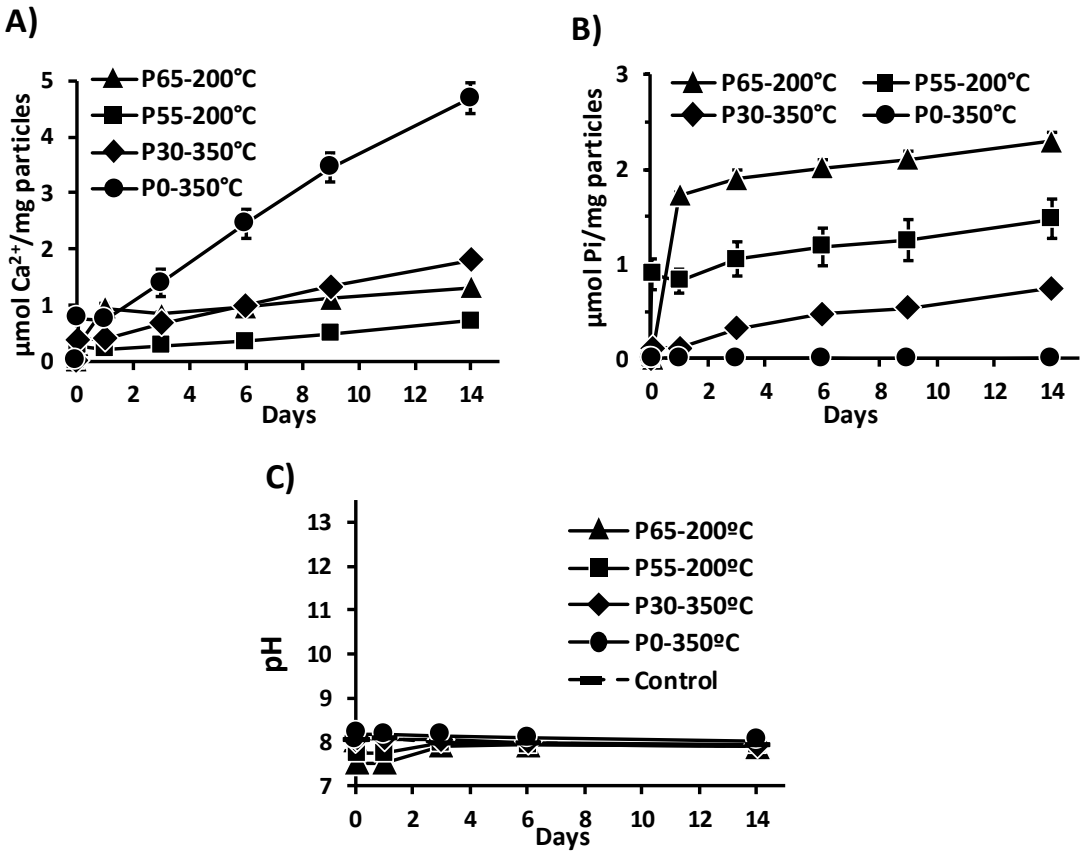

Figure 14. Cumulative Ca^{2+} **A)** and Pi **B)** release, and pH changes **C)** of the immersed thermally treated particles in HEPES media (pH 7.4) at 37 ºC. Media was replaced every time point.

The thermally treated particles showed a steadier degradability (Figure 14). The Ca^{2+} and Pi release was sustained for two weeks indicating that the decomposition of ethoxides and the subsequent increase of CP interactions stabilize the solubility of the particles. This time, we detected Pi due to the conversion of the MEP to Pi after thermal treatment. The presence of particles after the experiment (Figure 13) confirms their higher stability and suggests that further ion release could happen at longer times. Correlating the ion release results with the previous particle characterization, we identified the $CaCO_3$ followed by the ACP as the phases that released higher amounts of Ca^{2+} (P0-350ºC and P30-350ºC). On the other hand, the ACTMP phase (P55/P65-

200ºC) released higher amounts of Pi due to their higher P/Ca ration. Although the release of pyrophosphate has been reported to participate in bone mineralization [40], the stability of higher condensed phosphate units (i.e. trimetaphosphate) under acidic conditions (Figure 11) justifies further studies of how this molecule is metabolized by cells. The absence of significant pH changes (Figure 14C) validates the use of the particles for long-term physiological Ca^{2+} and Pi release. Although comparison with other degradable CP materials is difficult since ion release depends, for instance, on the type of used buffer media, its replacement and the material surface area in contact, the current particles exhibited similar or moderately higher Ca^{2+} and Pi releases than more complex CPg systems [37–39] and conventional ACP [41,42]. Therefore, their use for similar biological applications such as bone regeneration or wound healing is justified [3,10,43].

2.4. Conclusions

In this study we synthesized for the first time binary (P_2O_5-CaO) CPg nanoparticles by a low-cost and feasible sol-gel synthesis, using ethylphosphate and calcium 2-methoxiethoxide as precursors. We also gave precise information about the structure and solubility of the little-known CPg with CaO>50% [1], before and after thermal treatment. We identified by NMR spectroscopy and other complementary techniques the formation of highly soluble amorphous calcium MEP (CMEP) for the thermally untreated particles, with the presence of portlandite or $NH_4H_2PO_4$ for an excess or the absence of Ca, respectively. After a thermal treatment at 200 or 350 ºC, the CMEP and the portlandite of the particles were converted to a more stable, but still degradable, inorganic ACTMP, ACPP, ACP and calcite as the Ca content increase respectively. The use of a binary CPg system allowed us to control the Ca^{2+} and Pi release of the particles in physiological-like conditions without pH alterations by modifying their P/Ca ratio and applying this moderately low thermal treatment. The only presence of biocompatible and bioactive ions suggests a safer use compared to other glasses that include body-foreign stabilizers such as SiO_4^{4-}, or Ti^{4+}. The use of the current particles in biological applications where high or sustained Ca^{2+} and Pi concentrations are needed such as angiogenesis, osteogenesis or wound healing seems very promising. We would like to highlight that the CPg system used in this study is susceptible to allow the incorporation of small amounts of other bioactive ions such as Cu^{2+}, Zn^{2+} or Ag^{+} to introduce or reinforce specific bioactive responses (e.g. angiogenesis, osteogenesis or antimicrobial properties).

2.5. References

[1] J.C. Knowles, Phosphate based glasses for biomedical applications, J. Mater. Chem. 13 (2003) 2395–2401. doi:10.1039/b307119g.

[2] A. Aguirre, A. González, M. Navarro, Ó. Castaño, J.A. Planell, E. Engel, Control of microenvironmental cues with a smart biomaterial composite promotes endothelial progenitor cell angiogenesis, Eur. Cells Mater. 24 (2012) 90–106. doi:10.22203/eCM.v024a07.

[3] H. Oliveira, S. Catros, C. Boiziau, R. Siadous, J. Marti-Munoz, R. Bareille, S. Rey, O. Castano, J. Planell, J. Amédée, E. Engel, The proangiogenic potential of a novel calcium releasing biomaterial: Impact on cell recruitment, Acta Biomater. 29 (2016) 435–445. doi:10.1016/j.actbio.2015.10.003.

[4] D.M. Pickup, P. Guerry, R.M. Moss, J.C. Knowles, M.E. Smith, R.J. Newport, New sol–gel synthesis of a (CaO)0.3(Na2O)0.2(P2O5)0.5 bioresorbable glass and its structural characterisation, J. Mater. Chem. 17 (2007) 4777–4784. doi:10.1039/b709955j.

[5] B. Yu, C.A. Turdean-Ionescu, R.A. Martin, R.J. Newport, J. V Hanna, M.E. Smith, J.R. Jones, Effect of Calcium Source on Structure and Properties of Sol−Gel Derived Bioactive Glasses, Langmuir. 28 (2012) 17465−17476. doi:10.1021/la303768b.

[6] K. Franks, I. Abrahams, J.C. Knowles, Development of soluble glasses for biomedical use part I: In vitro solubility measurement, J. Mater. Sci. Mater. Med. 11 (2000) 609–614. doi:10.1023/A:1008949527695.

[7] K. Lin, Y. Liu, H. Huang, L. Chen, Z. Wang, J. Chang, Degradation and silicon excretion of the calcium silicate bioactive ceramics during bone regeneration

using rabbit femur defect model, J. Mater. Sci. Mater. Med. 26 (2015) 1–8. doi:10.1007/s10856-015-5523-2.

[8] B. Daley, A.T. Doherty, B. Fairman, C.P. Case, Wear debris from hip or knee replacements causes chromosomal damage in human cells in tissue culture., J. Bone Joint Surg. Br. 86 (2004) 598–606. doi:10.1302/0301-620X.86B4.14368.

[9] A. González-Vázquez, J.A. Planell, E. Engel, Extracellular calcium and CaSR drive osteoinduction in mesenchymal stromal cells, Acta Biomater. 10. 10 (2014) 2824–2833. doi:10.1016/j.actbio.2014.02.004.

[10] H. Oliveira, S. Catros, O. Castano, S. Rey, R. Siadous, D. Clift, J. Marti-Munoz, M. Batista, R. Bareille, J.A. Planell, E. Engel, The proangiogenic potential of a novel calcium releasing composite biomaterial : Orthotopic in vivo evaluation, Acta Biomater. 54 (2017) 377–385. doi:10.1016/j.actbio.2017.02.039.

[11] N. Sachot, O. Castaño, H. Oliveira, J. Martí-Muñoz, A. Roguska, J. Amedee, M. Lewandowska, J.A. Planell, E. Engel, A novel hybrid nanofibrous strategy to target progenitor cells for cost-effective in situ angiogenesis, J. Mater. Chem. B. 4 (2016) 6967–6978. doi:10.1039/C6TB02162J.

[12] O. Castaño, N. Sachot, E. Xuriguera, E. Engel, J.A. Planell, J.-H. Park, G.-Z. Jin, T.-H. Kim, J.-H. Kim, H.-W. Kim, Angiogenesis in Bone Regeneration : Tailored Calcium Release in Hybrid Fibrous Scaffolds, ACS Appl. Mater. Interfaces. 6 (2014) 7512−7522. doi:10.1021/am500885v.

[13] Advanced Chemistry Development (ACD), Inc., Toronto, ON, Canada, 2017, (n.d.). http://www.acdlabs.com/.

[14] H.J. Gitelman, An improved automated procedure for the determination of calcium in biological specimens, Anal. Biochem. 18 (1967) 521–531. doi:10.1016/0003-2697(67)90110-8.

[15] E. Gindler, J. King, Rapid colorimetric determination of calcium in biologic fluids with methylthymol blue, Am. J. Clin. Pathol. 58 (1972) 376–382. doi:10.1093/ajcp/58.5.376.

[16] S.G. Carter, D.W. Karl, Inorganic phosphate assay with malachite green: An improvement and evaluation, J. Biochem. Biophys. Methods. 7 (1982) 7–13. doi:10.1016/0165-022X(82)90031-8.

[17] A.F. Ali, P. Mustarelli, E. Quartarone, A. Magistris, Improving the synthesis of alkyl phosphates as sol-gel precursors, J. Mater. Res. 14 (1999) 327–329. doi:10.1557/JMR.1999.0047.

[18] V. Peruzzo, M. Andrea Chiurato, P. Tomasin, N. Brianese, P. Traldi, M. Favaro, Study of challenging calcium alkoxides in solution by electrospray ionisation mass spectrometry (Part 2), Eur. J. Mass Spectrom. 19 (2013) 453–461. doi:10.1255/ejms.1253.

[19] R.R. Biekofsky, S.R. Martin, J.P. Browne, P.M. Bayley, J. Feeney, Ca2+ Coordination to Backbone Carbonyl Oxygen Atoms in Calmodulin and Other EF-Hand Proteins : 15N Chemical Shifts as Probes for Monitoring Individual-Site Ca2+ Coordination, Biochemistry. 37 (1998) 7617–7629. doi:10.1021/bi9800449.

[20] S.C. Goel, M.A. Matchett, M.Y. Chiang, W.E. Buhro, A Very Large Calcium Dialkoxide Molecular Aggregate Having a CdI2Core Geometry: Ca9(OCH2CH2OMe)18(HOCH2CH2OMe)2, J. Am. Chem. Soc. 113 (1991) 1844–1845. doi:10.1021/ja00005a066.

[21] E.C. Hayes, T.R. Porter, C.J. Barrows, W. Kaminsky, J.M. Mayer, S. Stoll, Electronic Structure of a CuII-Alkoxide Complex Modeling Intermediates in Copper-Catalyzed Alcohol Oxidations, J. Am. Chem. Soc. 138 (2016) 4132–4145. doi:10.1021/jacs.5b13088.

[22] K.L. Taft, A. Caneschi, L.E. Pence, C.D. Delfs, G.C. Papaefthymiou, S.J. Lippard, Iron and Manganese Alkoxide Cubes, J. Am. Chem. Soc. 115 (1993) 11753–11766. doi:10.1021/ja00078a014.

[23] C. Kleinlein, S.L. Zheng, T.A. Betley, Ground State and Excited State Tuning in Ferric Dipyrrin Complexes Promoted by Ancillary Ligand Exchange, Inorg. Chem. 56 (2017) 5892–5901. doi:10.1021/acs.inorgchem.7b00525.

[24] D. Carta, J.C. Knowles, M.E. Smith, R.J. Newport, Synthesis and structural characterization of P2O5–CaO–Na2O sol–gel materials, J. Non. Cryst. Solids. 353 (2007) 1141–1149. doi:10.1016/j.jnoncrysol.2006.12.093.

[25] D. Carta, D.M. Pickup, J.C. Knowles, I. Ahmed, M.E. Smith, R.J. Newport, A structural study of sol–gel and melt-quenched phosphate-based glasses, J. Non. Cryst. Solids. 353 (2007) 1759–1765. doi:10.1016/j.jnoncrysol.2007.02.008.

[26] M. Navarro, S. del Valle, S. Martínez, S. Zeppetelli, L. Ambrosio, J.A. Planell, M.P. Ginebra, New macroporous calcium phosphate glass ceramic for guided bone regeneration, Biomaterials. 25 (2004) 4233–4241. doi:10.1016/j.biomaterials.2003.11.012.

[27] N.J. Lakhkar, J.H. Park, N.J. Mordan, V. Salih, I.B. Wall, H.W. Kim, S.P. King, J. V. Hanna, R.A. Martin, O. Addison, J.F.W. Mosselmans, J.C. Knowles, Titanium phosphate glass microspheres for bone tissue engineering, Acta Biomater. 8 (2012) 4181–4190. doi:10.1016/j.actbio.2012.07.023.

[28] A. Taha, M. Akram, Z. Jawad, A.Z. Alshemary, R. Hussain, Strontium doped injectable bone cement for potential drug delivery applications, Mater. Sci. Eng. C. 80 (2017) 93–101. doi:10.1016/j.msec.2017.05.117.

[29] A. Paz, D. Guadarrama, M. López, J.E. González, N. Brizuela, J. Aragón, A comparative study of hydroxyapatite nanoparticles synthesized by different

routes, Quim. Nov. 35 (2012) 1724–1727.

[30] T. Windarti, Taslimah, A. Haris, Y. Astuti, A. Darmawan, Synthesis of β-Calcium Pyrophosphate by sol-gel method, IOP Conf. Ser. Mater. Sci. Eng. 172 (2017) 012058. doi:10.1088/1757-899X/172/1/012058.

[31] R. Mathew, P.N. Gunawidjaja, I. Izquierdo-Barba, K. Jansson, A. García, D. Arcos, M. Vallet-Regí, M. Edén, Solid-State 31P and 1H NMR Investigations of Amorphous and Crystalline Calcium Phosphates Grown Biomimetically From a Mesoporous Bioactive Glass, J. Phys. Chem. C. 115 (2011) 20572–20582. doi:10.1021/jp206237n.

[32] J.P. Fletcher, R.J. Kirkpatrick, D. Howell, S.H. Risbud, 31P Magic-angle Spinning Nuclear Magnetic Resonance Spectroscopy of Calcium Phosphate Glasses, J. Chem. Soc. Faraday Trans. 89 (1993) 3297–3299. doi:10.1039/FT9938903297.

[33] I. Abrahams, K. Franks, G.E. Hawkes, G. Philippou, J. Knowles, T. Nunes, 23Na , 27Al and 31P NMR and X-ray powder diffraction study of Na/Ca/Al phosphate glasses and ceramics, J. Mater. Chem. 7 (1997) 1573–1580. doi:10.1039/A608325K.

[34] B.C. Smith, The C-O Bond, Part I : Introduction and the Infrared Spectra of Alcohols, Spectroscopy. 32 (2017) 14–21.

[35] National Institute of Advanced Industrial Science and Technology, SDBS. (2018). http://sdbs.db.aist.go.jp/sdbs/cgi-bin/cre_index.cgi.

[36] L. Jiang, Y. Li, Y. Shao, Y. Zhang, R. Han, S. Li, W. Wai, Enhanced removal of humic acid from aqueous solution by novel stabilized nano-amorphous calcium phosphate : Behaviors and mechanisms, Appl. Surf. Sci. 427 (2018) 965–975. doi:10.1016/j.apsusc.2017.08.104.

[37] I. Ahmed, M. Lewis, I. Olsen, J.C. Knowles, Phosphate glasses for tissue

engineering : Part 1 . Processing and characterisation of a ternary-based P2O5–CaO–Na2O glass system, Biomaterials. 25 (2004) 491–499. doi:10.1016/S0142-9612(03)00546-5.

[38] M. Navarro, M. Ginebra, J. Clément, M. Salvador, A. Gloria, J.A. Planell, Physicochemical Degradation of Titania-Stabilized Soluble Phosphate Glasses for Medical Applications, J. Am. Ceram. Soc. 86 (2003) 1345–1352. doi:10.1111/j.1151-2916.2003.tb03474.x.

[39] J.C. Knowles, K. Franks, I. Abrahams, Investigation of the solubility and ion release in the glass system K2O-Na2O-CaO-P2O5, Biomaterials. 22 (2001) 3091–3096. doi:10.1016/S0142-9612(01)00057-6.

[40] Z. Zyman, A. Goncharenko, D. Rokhmistrov, Kinetics and mechanisms of the transformation of precipitated amorphous calcium phosphate with a Ca/P ratio of 1:1 to calcium pyrophosphates, J. Cryst. Growth. 478 (2017) 117–122. doi:10.1016/j.jcrysgro.2017.08.031.

[41] M.A.S. Melo, M.D. Weir, V.F. Passos, M. Powers, H.H.K. Xu, Ph-activated nano-amorphous calcium phosphate-based cement to reduce dental enamel demineralization, Artif. Cells, Nanomedicine Biotechnol. 45 (2017) 1778–1785. doi:10.1080/21691401.2017.1290644.

[42] M. Yang, J. Ren, R. Zhang, Novel gallium-doped amorphous calcium phosphate nanoparticles: Preparation, application and structure study, J. Non. Cryst. Solids. 466–467 (2017) 15–20. doi:10.1016/j.jnoncrysol.2017.03.034.

[43] C. Navarro-Requena, J.D. Weaver, A.Y. Clark, D.A. Clift, S. Pérez-Amodio, Ó. Castaño, D.W. Zhou, A.J. García, E. Engel, PEG hydrogel containing calcium-releasing particles and mesenchymal stromal cells promote vessel maturation, Acta Biomater. (2017). doi:10.1016/j.actbio.2017.12.009.

Chapter 3. Development of Ca^{2+} releasing polylactic acid (PLA) nanofiber scaffolds to stimulate angiogenesis in bone healing applications

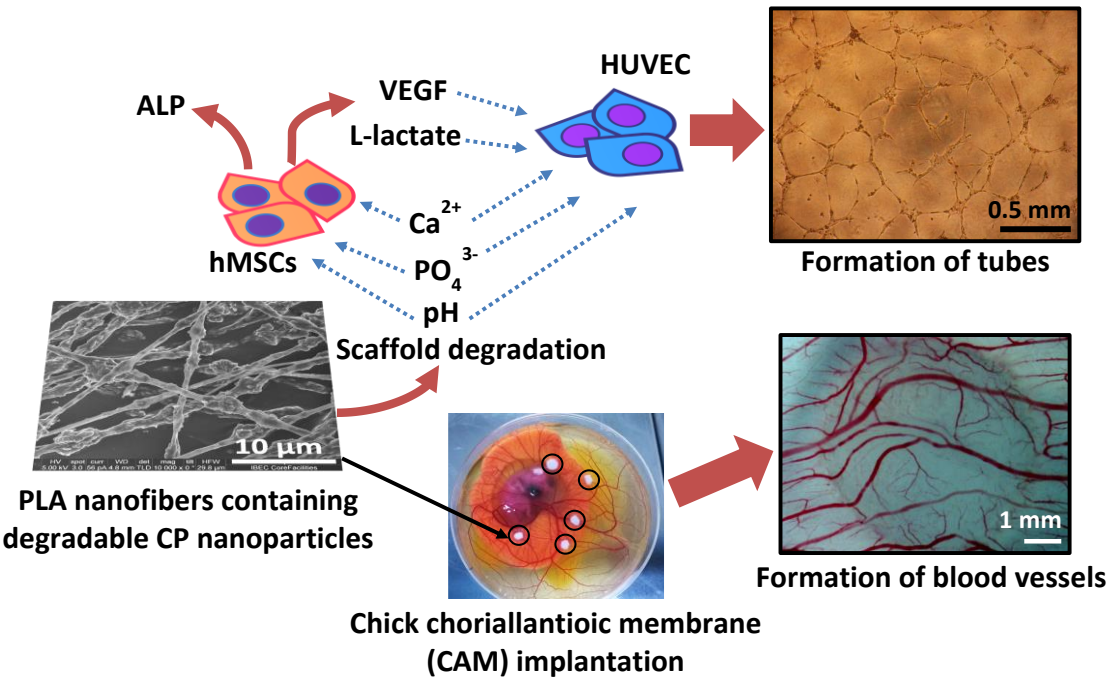

Scheme summarizing the content of the chapter.

A proper integration implant-tissue promoted by a correct vascularization is crucial for any bone graft. Degradable calcium phosphate (CP) materials have gain interest in bone tissue engineering since they stimulate bone formation. However, little is known about their angiogenic potential. Recent findings in our group demonstrated that their Ca^{2+} release stimulates the cellular synthesis of vascular growth factors among other responses that favor angiogenesis. In this chapter, we combined two of the CPg nanoparticles synthesized in Chapter 2 (P55-RT and P30-350ºC), with polylactic acid (PLA) nanofibers to achieve scaffolds with fast and sustained Ca^{2+} release profiles. We would like to remember and highlight that these particles were only composed by well-known biocompatible ions (e.g. Ca^{2+}, PO_4^{3-}), avoiding the incorporation of body-foreign SiO_4^{4-} and Ti^{4+}. Particles and scaffolds characterization includes; ^{31}P MAS NMR, ^{1}H NMR, XRD, EDS, elemental analysis, FE-SEM, tensile-strain assays and DSC. We studied the *in vitro* angiogenic potential of the scaffolds in both regular (RM) and osteogenic media (OM). Finally, we evaluated the *in vivo* formation of new vasculature by using the *ex-ovo* chick choriallantoic membrane (CAM) model**.** We achieved high initial and further sustained Ca^{2+} and PO_4^{3-} releases without pH modifications in both RM and OM. We observed that the presence of the particles enhanced several angiogenic parameters like the VEGF and L-lactate synthesis by hMSCs, the formation of tubes by HUVECs and the stimulation of new vasculature in the CAM model. However, some of these parameters decreased in OM due to the osteogenic differentiation of hMSCs. This study provides an easily tunable Ca^{2+} releasing platform containing no body-foreign ions, with a promising potential not only for bone but also for the regeneration softer tissues in which an initial high vasculature is essential.

3.1. Introduction

Most of the failures of biomaterials in the field of tissue engineering are in a greater or lesser extent due to a bad biointegration with the host tissue. A poor vascularization is often the cause since cell death occurs when there is an insufficient blood supply. Bone is a highly vascularized tissue and it is specially affected by this problem [1,2]. Biodegradable calcium phosphate (CP) materials have been widely used to regenerate bone. It is known that their partial dissolution towards the surrounding tissue stimulates bone formation [3]. Although, CP materials have also shown to stimulate blood vessel formation, which may be one of the reasons of their success as a bone grafts, little is known about their angiogenic potential [2]. Recent findings in our group indicates that their Ca^{2+} release has a close correlation with angiogenesis [1,4–6]. Our studies showed that these Ca^{2+}-releasing materials promoted the survival and migration of endothelial cells as well as the synthesis of angiogenic factors through the stimulation of extracellular calcium-sensing receptors (CaSRs) [4]. Moreover, we also observed that degradable CP nanoparticles increased the formation of blood vessels in different *in vivo* models [1,5]. This direct cell stimulation minimizes or even eliminates the need of using growth factors or exogenous cells with associated risks and elevated money-costs [2]. CP glassy systems (more degradable than crystalline CP) often incorporate the presence of extra ions (e.g. SiO_4^{4-}, Ti^{4+}) [7,8] to control their degradability. However, the metabolization and side effects of these ions is still unclear [9–11]. In this study, we wanted to avoid such ions synthesizing pure CP glasses, whose ion release could be controlled by modifying their Ca/P ratio and applying a moderately low thermal treatment (350 ºC). We synthesized two different sol-gel CP nanoparticles (containing only Ca and P) with different degradability to achieve fast and sustained Ca^{2+} release rates. We combined the particles with electrospun polylactic acid (PLA) nanofibers to obtain implantable scaffolds. Characterization of the particles and the scaffolds includes nuclear magnetic

resonance (^{31}P MAS NMR, ^{1}H NMR), X-ray diffraction (XRD), energy dispersive X-ray spectroscopy (EDS), elemental analysis (EA), field emission scanning electron microscopy (FE-SEM), tensile-strain assays and differential scanning calorimetry (DSC). We evaluated how the released-by-products (i.e. Ca^{2+}, PO_4^{3-}, L-lactate and pH) of the scaffolds in regular (RM) and osteogenic media (OM) affected in the hMSCs adhesion, proliferation, alkaline phosphatase (ALP) activity and VEGF and L-lactate synthesis by hMSCs. Finally, we assessed the capacity of the scaffolds to promote angiogenesis using the *in vitro* HUVEC tube formation assay and the *ex-ovo* chick choriallantoic membrane (CAM) model that allows quantify the formation of new blood vessels.

3.2. Materials and Methods

If not otherwise specified all reagents were purchased from Sigma-Aldrich.

3.2.1. Sol-gel precursors synthesis

4 M ethylphosphate in ethanol and 1M calcium 2-methoxyethoxide in 2-methoxyethanol were synthesized as previously published [1,5]. Briefly, the right amount of phosphorus pentoxide (≥99.99%) and metallic calcium granules PS (98%, Panreac) were refluxed in distilled absolute ethanol PRS (99,5%, Panreac) or anhydrous 2-methoxyethanol (99,8%) respectively under $Ar_{(g)}$ atmosphere for 12 or 24 h respectively. The solutions were filtered using 0.45 µm PTFE hydrophobic Minisart® SRP25 syringe filters (Sartorius AG, Göttingen, Germany) and stored under $Ar_{(g)}$ at -20ºC.

3.2.2. CP particles synthesis

We synthesized two types of degradable CP nanoparticles with different phosphorus (P) contents (P30 and P55). Summarizing, the 4 M ethylphosphate and the 1M calcium 2-methoxyethoxide precursors were mixed together under vigorous stirring in a ratio of 1.5:8.5 mL or 4:6 mL in 90 mL of absolute ethanol PRS (99,5%, Panreac) to achieve P30 or P55 particles respectively. P55 particles were spontaneously obtained after approximately 10 minutes of mixing the two precursors. On the other hand, ~30 mL of Ammonia PA-ACS (30%, Panreac) were slowly added under stirring to obtain a suspension of the P30 particles. Particles were washed/centrifuged at 48384xg for 20 min twice with absolute ethanol PRS (99,5%, Panreac) and once with hexane ACS (≥99%). Afterwards, particles were dried at 70 ºC for 2 h, mild in an agate mortar and stored in a desiccator under vacuum. P30 particles were thermally treated at 350 ºC in a

muffle furnace L9/11 (Nabertherm, Lilienthal, Germany) for 12 h to eliminate unreacted organics and to stabilize their structure. P30-350ºC particles were also stored in a desiccator under vacuum.

3.2.3. Scaffolds fabrication

Three different scaffolds; pure polylactic acid nanofibers (PLA), PLA nanofibers containing a 60% (w/w) of the P30-350ºC particles (PLA+P30) and PLA nanofibers containing a 60% (w/w) of the P30-350ºC particles plus a 20% ($w/w_{PLA+P30}$) of the P55 particles (PLA+P30+P55) were fabricated using the electrospinning technique. The used electrospinning parameters were adapted from previous studies performed by a former PhD student (Dr. Nadège Sachot) [1,5]. Briefly, the right amount of the particles was dispersed in 5 mL of 2,2,2-trifluoroethanol (TFE) (99,8%, Panreac), using a Branson Digital Sonifier S-450 (Branson Ultrasonics, Danbury, CT, USA). Polylactic acid Purasorb PLDL 7038 (Corbion), (70% L-lactate, 30% DL-lactate) inherent viscosity midpoint 3.8 dL/g, molecular mass $85 \cdot 10^4$ Da was added to the suspension under vigorous stirring until reaching a concentration of 4% (w/w_{TFE}). Once the PLA was dissolved (~4 h), the slurries were placed in 5 mL PP/PE syringes and electrospun separately at ~10 KV, ~2 mL/h and ~12 cm distance tip to collector. Fibers were collected in a cylindrical collector covered with parchment paper. The collector spun at 120 rpm to homogenize the scaffold thickness through the rotation direction while maintaining a random fiber distribution.

3.2.4. Particles and scaffolds characterization

3.2.4.1. Energy dispersive X-ray spectroscopy (EDS) of the particles was performed in a Quanta Q200 scanning electron microscope (SEM) (FEI Company, Hillsboro, OR, USA) coupled with an EDS detector to determine their P and Ca content. Particles were

analyzed at 20 KV, 10 mm working distance and were previously coated with a thin carbon layer to improve conductivity. Values express the average of at least three different measurements.

3.2.4.2. Elemental analysis (EA) of the particles was performed by combustion in an elemental analyzer EA CE 1108 (Thermo Fischer Scientific, Waltham, MA, USA) to determine their C and N content. Approximately, 2000 µg of the particles were weighed in a MX5 microbalance (Mettler-Toledo, Greifensee, Switzerland). The samples were analyzed by combustion at 1060 ºC using atropine as standard. A mixture of vanadium pentoxide and lead powder was added to facilitate combustion.

3.2.4.3. X-ray diffraction (XRD) was performed in a PANalytical X'Pert PRO MPD Alpha1 Powder diffractometer (PANalytical, Almelo, the Netherlands) to determine the crystalline phases in the particles. Approximately, 100 mg of the particles were pressed in a cylindrical standard sample holder of 16 mm of diameter and 2.5 mm of height. Samples were analysed in a Bragg-Brentano $\theta/2\theta$ 240 mm radius geometry. We interpreted the spectra with the ©PANalytical X'Pert HighScore software (PANalytical, Almelo, the Netherlands) and the database PDF2 (2001) from the international center of diffraction data (ICDD).

3.2.4.4. ^{31}P MAS NMR spectroscopy of the particles was performed in a 400 MHz-WB Avance-II spectrometer (Bruker, Billerica, MA, USA) externally referenced to H_3PO_4 (85%) to determine the presence of condensed phosphate units. Approximately, 50 mg of the particles were placed in a ZrO_2 4 mm rotor and spun at 12 kHz. HPDEC.AV standard pulse sequence was used to run the experiments with a 5 µs pulse length corresponding to a 90º tip angle. The recovery delay was set to 5 s. A total of 512 scans were accumulated for each spectrum to have a good signal-to-noise ratio. ^{1}H nuclei was

decoupled using Spinal-64 scheme (at 73 watts power level). Data was processed applying a FT exponential function (line broadening, *lb* 15 Hz).

3.2.4.5. ^{1}H NMR spectroscopy of the dissolved particles in acidic heavy water (D_2O) was performed in a Bruker 400 MHz Avance III spectrometer (Bruker, Billerica, MA, USA) equiped with a Prodigy TCI 5 mm cryoprobe to characterize the presence of organics. Approximately, 5 mg of the particles were dissolved separately in 1 mL of D_2O (99.9%) containing 1.5% (v/v) of HCl (37%, Panreac). Spectra were registered between 16 and -3.8 ppm, applying 3.66 µs, 30° pulse, a delay of 1 s between pulses, and an acquisition time of 2.5 s. 32 scans were collected to have a good signal-to-noise ratio. Data was analyzed using the ACD/Spectrus Processor software [12].

3.2.4.6. Field emission scanning electron microscopy (FE-SEM) images of the fibers were performed in a NOVA NanoSEM-230 ultrahigh-resolution field emission scanning electron microscope (FE-SEM) (FEI Company, Hillsboro, OR, USA) to determine the morphology of the scaffolds. Scaffolds were previously coated with a thin carbon layer to improve conductivity. Samples were irradiated at 5 KV at a working distance of 5 mm.

3.2.4.7. Mechanical properties of the scaffolds were characterized by applying tensile-strain tests at room temperature using a Zwick-Roell Z0.5TN testing machine (Zwick Roell Group, Ulm, Germany). Four samples per each scaffold were cut into ISO 257-1/2 standardized test specimens of 50x5 mm using a stainless-steel punch and a surgical blade. The tensile-strain was calculated on the nominal cross-section area of the specimens. We used a caliper and a digital micrometer to measure the exact width and thickness of the samples. The average thickness ranged from 50 to 150 µm. The Young's modulus was considered as the slope of the linear region of the tensile-strain curve. The ultimate strength was considered as the maximum tensile stress supported by the material. The strain to failure was fixed to the previous point before a 40% of loss

of the tensile strength. The tensile-strain test was monitored at a speed of 10 $mm \cdot min^{-1}$ using a force cell of 10 N. We used the testXpert II testing software (Zwick Roell Group, Ulm, Germany) to process the data.

3.2.4.8. Differential scanning calorimetry (DSC) was performed in a DSC Q20 (TA instruments, New Castle, DE, USA) coupled with a nitrogen chiller to determine the thermal properties of the PLA in the scaffolds. Random ~9.4 mg pieces of each scaffold were placed in aluminum hermetic pans and submitted to two heating cycles from -90 to 200 ºC at 10 $ºC \cdot min^{-1}$, with a nitrogen cooling between cycles. We determined the crystallization and melting properties of the PLA from the curve of the first cycle. From the curve of the second cycle we assessed the glass transition temperature (Tg) applying the inflexion point method. We used the Universal Analysis software v4.7A (TA instruments, New Castle, DE, USA) to process de data.

3.2.5. *In vitro* experiments

If not otherwise specified all percentages refer to volume.

3.2.5.1. Cell expansion

Adult human mesenchymal stem cells (hMSCs) from bone marrow passage 2 provided by the Texas A&M Health Science Center College of Medicine Institute for Regenerative Medicine at Scott & White through a grant from NCRR of the NIH, Grant # P40RR017447, were expanded in 175 cm^2 EasyFlask™ Nunclon™ (Thermo Fischer Scientific) with minimum essential medium (αMEM) w/o nucleosides (1X) (Gibco®) complemented with 16.5% of characterized fetal bovine serum (FBS) HyClone™ (GE Healthcare), 1% of L-glutamine (200 mM, Invitrogen™) and 1% of penicillin-streptomycin

(10^4 U/mL, Invitrogen ™). Human umbilical vein endothelial cells (HUVECs) (EndoGRO™) passage 2 were expanded in 175 cm^2 EasyFlask™ Nunclon™ (Thermo Fischer Scientific) with EndoGRO-LS complete culture media (Merck Millipore) plus 1% of penicillin-streptomycin (10^4 U/mL, Invitrogen™). Both cell types were incubated under sterile conditions at 37 ºC, 5% CO_2 and a high moisture level. Medium was replaced every 2-3 days. Before reaching confluence (~5 days) cells were extracted using TrypLE™ Express Enzyme (1x) phenol red (Gibco®) and used for the *in vitro* experiments.

3.2.5.2. hMSCs seeding on the scaffolds

Discs of 6 mm of the different scaffolds (PLA, PLA+P30 and PLA+P30+P55) were cut using a Harris Uni-Core™ 6.0 mm punch (Whatman plc, Little Chalfont, UK) and sterilized under UV-light. The discs were placed in ultra-low attachment 96-well plates Nunclon™ Sphera™ (Thermo Fischer Scientific). We prepared four replicates per condition. Before seeding the cells, discs were wet using a sterile-filtered 30% absolute ethanol PRS (99,5%, Panreac) solution in milli-Q water. The ethanol solution was removed, and the scaffolds discs were cleaned twice with complete αMEM. The discs were left without media but wet in the incubator overnight. 10^4 hMSCs/scaffold were seeded in 80 µL of complete αMEM or osteogenic media (complete αMEM supplemented with 100 nM of dexamethasone (≥97%), 50 µM of L-ascorbic acid 2-phosphate trisodium salt (≥95.0%) and 10 mM of β-glycerophosphate disodium salt hydrate (≥99.0%)). A control of hMSCs (TCP) on 96-well plates Nunclon™ Delta (Thermo Fischer Scientific) was performed to confirm a normal cell behavior. Media was replaced every 2-3 days.

3.2.5.3. Ca^{2+}, PO_4^{3-}, pH, L-lactate, VEGF, total DNA and ALP activity quantification

After 1, 3, 6, 13 and 20 days the media from section 3.2.5.2. were extracted and frozen at -80 ºC for later Ca^{2+}, PO_4^{3-}, pH, L-lactate and VEGF quantification. At the same time points, hMSCs were lysate to measure total DNA and ALP activity. To lysate the hMSCs we followed the instructions provided in the SensoLyte® pNPP Alkaline Phosphatase Assay Kit (AnaSpec Inc.). Briefly, the discs were placed in 1.5 mL centrifuged microtubes with 125 µL of the 10x buffer plus 1x Triton-X (both included in the kit). The tubes were placed on ice to preserve the DNA. The discs were smashed, cut (using a surgical scissors) and sonicated for 10 s with an Ultrasonic Processor UP50H (Hielscher Ultrasonics, Teltow, Germany) to ensure a correct extraction of the DNA and ALP. The hMSCs from the TCP (with 125 µL of the lysate solution) were scratched from the bottom of the wells using PP ultra-micro pipet tips (VWR international), sonicated as before mentioned and the media were transferred into microtubes. All microtubes were centrifuged at 10^4xg for 15 min and 110 µL of the supernatant were frozen at -80 ºC for further DNA and ALP quantification. To measure the DNA we used the Quant-iT™ PicoGreen™ dsDNA Assay kit (invitrogen™). The calibration curve was prepared using the same buffer media (10x buffer + 1x Trito-X) that we used to lysate the cells since Triton-X increases PicoGreen™ fluorescence intensity. To measure the ALP activity, we used the SensoLyte® pNPP Alkaline Phosphatase (ALP) Assay Kit (AnaSpec Inc.). The VEGF, L-lactate and PO_4^{3-} from the extracted media were measured using the Human VEGF DuoSet® ELISA Kit (R&D Systems™), the D/L-Lactate UV method kit (Nzytech) and the Phosphate Colorimetric Assay Kit respectively. To measure the Ca^{2+} content we used an adapted colorimetric method based on the O-Cresolphthalein complexone [13,14], which absorbance intensity was measured at 570 nm (see Chapter 2, section 2.2.11.). Finally, we measured the pH with a Crison 50 28 pH electrode connected to a Crison pH-Meter GLP 22+ (Hach Company, Loveland, CO, USA). Samples were diluted if necessary. All absorbance and fluorescence intensities were measured in an Infinite

M200 Pro Microplate Reader (Tecan Group Ltd., Männedorf, Zürich, Switzerland). Since ALP, VEGF and L-Lactate were cell dependent we normalized them by the total hMSCs DNA.

3.2.5.4. HUVECs tube formation assay

10^4 hMSCs were seeded on the 6 mm scaffolds discs and on the TCP (20 replicates per condition) as previously explained in section 3.2.5.2.. At day 3, 13 and 20, the media from the replicates of each condition were pooled and frozen at 80 ºC for later use. 50 µL of Matrigel® Growth Factor Reduced (Corning Inc.) were placed at 8 ºC on 96-well plates Nunclon™ Delta (Thermo Fischer Scientific) and incubated at 37 ºC for 30 min to allow gelation. When the Matrigel® was set, we seeded $1.5 \cdot 10^4$ HUVECs/well in 80 µL of αMEM, four replicates per condition. Cells were incubated for 1 h to allow their attachment, afterwards the media were removed and replaced with 80 µL of the extracted regular media (ERM). The ERM were previously warmed at 37 ºC and centrifuged to eliminate artifacts that could affect image analysis. After 8 h of incubation, we photographed the HUVECs using an inverted DM IL LED microscope (Leica Microsystem, Wetzlar, Germany). Images were analyzed using the Angiogenesis Analyzer ImageJ plugin [15] to evaluate the tube network produced. A negative control (NC) with complete αMEM (RM) was performed to compare samples with a non-promoting angiogenic condition. We used the average of the statistical differences (P_{value}) with the NC of all the measurements performed by the Angiogenesis Analyzer plugin (Figure 12) to evaluate the quality of the tube network produced.

3.2.6. *Ex-ovo* chick choriallantoic membrane (CAM) model

This protocol was adapted from [16]. Briefly, fertilized chick eggs (Granja Gibert S.A., Cambrils, Spain) were incubated at 37.5 ºC in an SI 24 eggs incubator (Lincu Avitec S.L., Valencia, Spain) with air ventilation and a high humid atmosphere. After 3 days, the eggs were cracked, and the full embryos were placed in Falcon™ standard tissue culture dishes 100x20 mm (Corning Inc.) surrounded with sterile phosphate buffered saline (Gibco®) solution to maintain a high moisture level. After 6 more days of incubation, scaffolds discs (only PLA and PLA+P30+P55) of 6 mm were placed on the CAM near to the big blood vessels (Figure 1). We implanted 30 replicates per condition distributed in 7 different embryos. The discs were previously set on UV-sterilized 6 mm nylon net filters discs (Merck Millipore Ltd.) and fixed with 30 µL of 2 mg/mL Opticol™ Rat Type I Collagen (3.8 mg/mL, Cell Guidance Systems) solution to avoid scaffold shrinkage during implantation. Briefly, the Opticol™ (3.8 mg/mL, Cell Guidance Systems) was mixed with the included neutralizing solution at a ratio of 9:1 (v:v), the mixture was diluted to 2 mg/mL with complete αMEM. 30 µL of this solution were placed on each mounted scaffold on the nylon discs and previously wet as mentioned in the hMSCs seeding section 3.2.5.2.. The Opticol™ was allowed to jellify at 37 ºC for 45 min. A positive control of PLA plus 200 ng of Recombinant Human VEGF 121 (PeproTech®) was implanted to compare samples with a known angiogenic condition. We also implanted the scaffolds with hMSCs after 13 days of culture (PLA+hMSCs and PLA+P30+P55+hMSCs), in which the neutralized Opticol™ solution (2mg/mL) was prepared with the hMSCs ERM at day 13. After 3 days of implantation, the embryos were sacrificed by decapitation and the discs and the surrounding CAM were fixed with Formalin solution neutral buffered (10%). After 25 min, the fixed discs were cut and photographed from the side in contact with the CAM in a MVX10 Macro Zoom Microscope (Olympus Corporation, Tokyo, Japan). The small blood vessels on each scaffold were quantified by using an own-developed ImageJ

macro (Figure 14), which briefly, quantifies the pixels occupied by the small blood vessels and normalizes it by the total area analyzed in pixels.

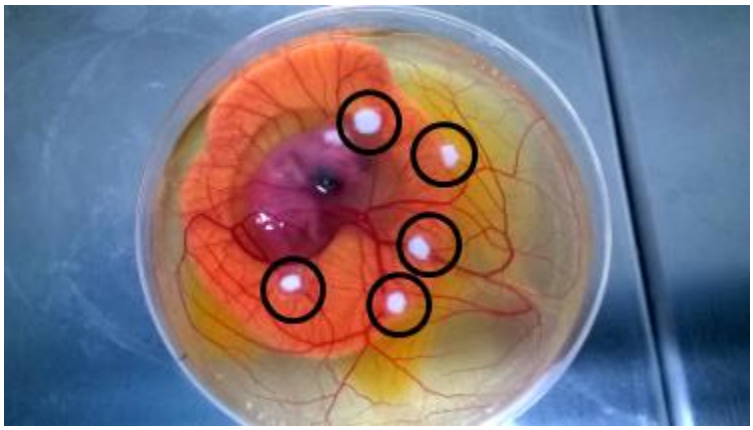

Figure 1. Picture showing the implantation of the scaffolds in the *ex-ovo* CAM model.

3.2.7. Statistical analysis

Statistics were performed using GraphPad Prism 6. A two-way ANOVA and a Tukey's multiple comparison test was used in the *in vitro* experiments to observe both; statistical differences between conditions at each time point, and statistical differences of each condition between consecutive time points. For the tube formation assay (section 3.2.5.4.), we used a Dunnet's multiple comparison test to detect statistical differences with the NC (Figure 12). It was considered that all values in the *in vitro* experiments followed a Gaussian distribution, although not enough replicates (n=4) were taken to perform a D'Agostino-Pearson omnibus normality test. We analyzed statistical differences between conditions in the CAM model (section 3.2.6.) using a one-way ANOVA and a Tukey's multiple comparison test. The D'Agostino-Pearson omnibus normality test confirmed that all values in section 3.2.6. followed a Gaussian distribution. We used the one-tailed t test to confirm the previous hypothesis of observing a statistical higher amount of new blood vessels in the PLA+P30+P55 scaffolds than in the pure PLA

ones [17]. The F test (in the t-test) confirmed no statistical differences between variances. All conditions in all sections were considered unmatched. We considered only P_{values}<0.001 (*) and <0.0001 (**) in section 3.2.5.3. due to the found high amount of statistical differences. We considered P_{value}<0.05 (*), <0.01 (**), <0.001 (***) and <0.0001 (****) for the other sections. Columns in the graphs represent means and error bars the standard error of the mean (SEM).

3.3. Results & discussion

3.3.1. CP particles and scaffolds characterization

As we previously discussed in Chapter 2, we identified the P30-350ºC particles as a mixture of amorphous calcium (pyro)phosphate (ACP and ACPP) and $CaCO_3$, while the P55-RT particles were mainly an amorphous calcium monoethylphosphate salt. ^{31}P MAS NMR spectra (Figure 2A) showed the presence of orthophosphate units (Q^0) and a small amount of pyrophosphates (Q^1) in both particles [18,19]. X-ray diffraction spectrum (Figure 2B) revealed also the formation of calcite ($CaCO_3$) for P30-350ºC.

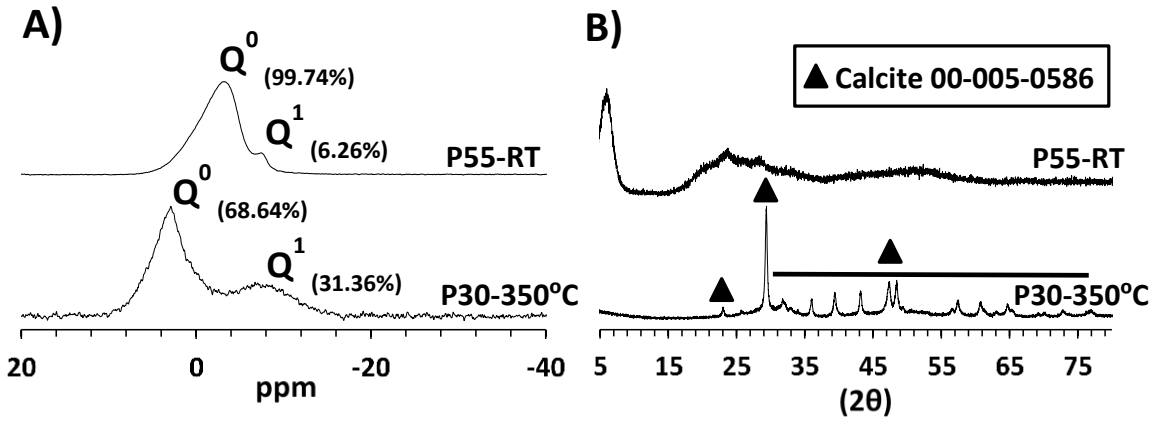

Figure 2. ^{31}P MAS NMR **A)** and X-ray diffraction **B)** spectra of the P30-350ºC and P55-RT particles.

Table 1. Particles P/Ca atomic ratio (%) measured by EDS and C and N mass % measured by EA.

	P /Ca ratio (atomic %)	C (mass %)	N (mass %)
P55-RT	54.2/45.8	17.78	≤ 0.2
P30-350ºC	29.8/70.2	5.66	≤ 0.2

The detection of only P and Ca by EDS (Table 1) indicates that the phosphates were in form of calcium phosphates (CP). The inexistence of crystalline CP phases (Figure 2B) shows that P30-350ºC and P55-RT particles contained amorphous CP. However, we did not consider them as glasses due to their low rate of phosphate condensation (amount of Q^2 and Q^1 units) (Figure 2A) [19–21]. We attribute the carbon (C) detected for P30-350ºC particles (Table 1) to the formation of $CaCO_3$ while the one for P55-RT to the presence of organics.

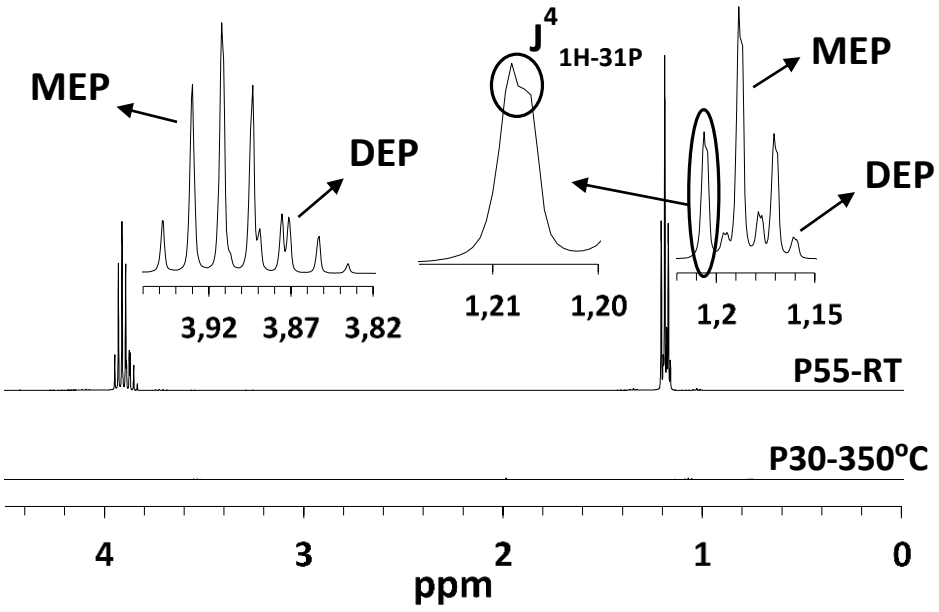

Figure 3. ^{1}H NMR spectra of the dissolved P55-RT and P30-350ºC particles in acidic D_2O. Peak assignment is based on the information obtained in Chapter 2, section 2.3.5.4..

The ^{1}H-NMR spectra of the dissolved P55-RT particles in acidic D_2O (Figure 3) showed that these organics were monoethylphosphate (MEP) and a small amount of diethylphosphate (DEP). On the other hand, the absence of organics for the dissolved P30-350ºC particles confirms that the detected C in Table 1 came from the $CaCO_3$. With this information we conclude that the P30-350ºC particles were a mixture of amorphous CP (ACP) [18], amorphous calcium pyrophosphate (ACPP) [19,22] and calcite ($CaCO_3$).

On the other hand, we considered P55-RT particles as an amorphous calcium MEP salt. We attributed the higher phosphate condensation of P30-350ºC (despite having less P content than P55-RT) to the thermal treatment applied, while the formation of $CaCO_3$ was attributed to the carbonatation of the excess Ca at 350 ºC. Notice that the presence of ethoxides for P55-RT was due to these particles were not thermally treated.

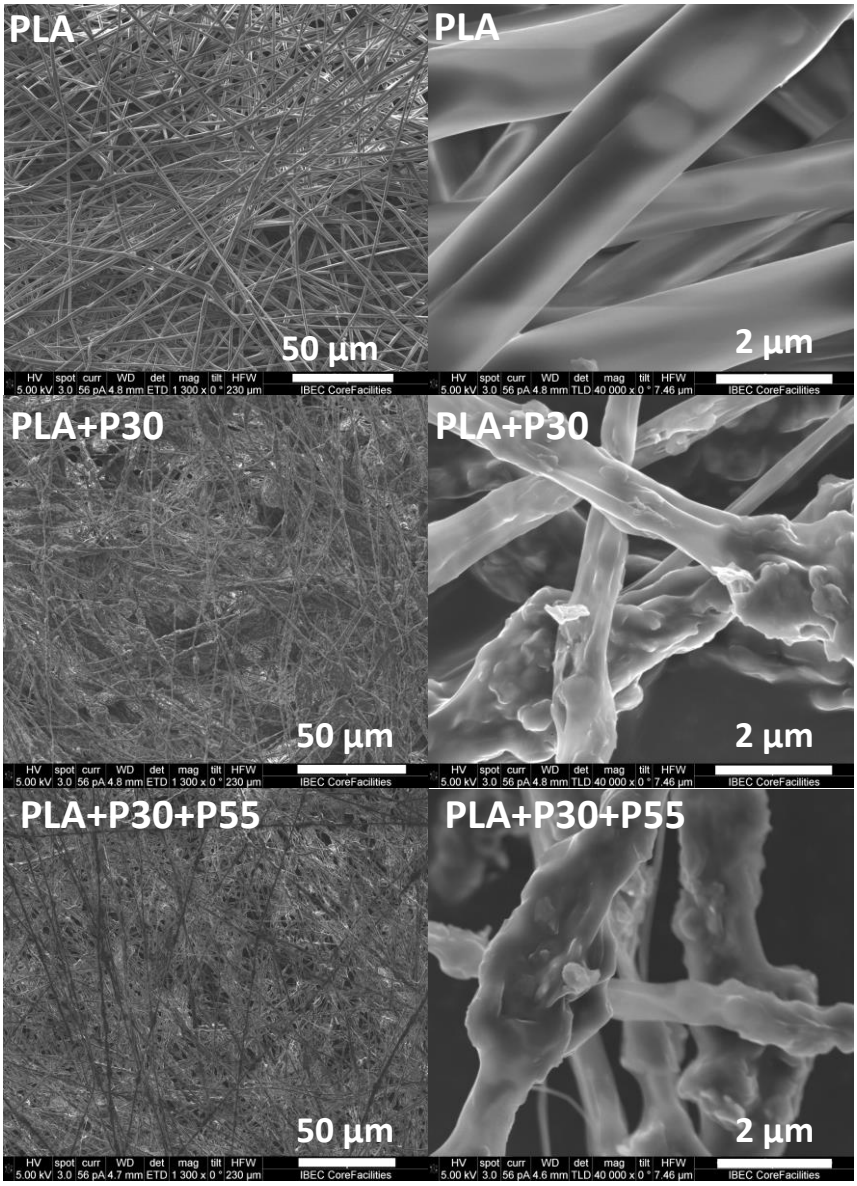

Figure 4. Morphological FE-SEM images of the different PLA nanofiber scaffolds. PLA+P30 scaffolds contained a 60% of the P30-350ºC particles. The PLA+P30+P55 scaffolds contained the same amount of P30-350ºC plus a 20% of the P55-RT particles.

From now on, we will refer to P55-RT and P30-350ºC particles as P55 and P30. FE-SEM images of the electrospun scaffolds (Figure 4) showed significant smaller fibers diameters for the scaffolds containing the particles (~1 vs ~2 µm). It may be that the partial degradation of the particles during the dissolution of the PLA before electrospinning modified the pH or partially degraded the PLA molecules reducing the solution viscosity. Changes in the polymer solution viscosity or conductivity are known to have an effect in the diameter size of the electrospun fibers [23]. Although the fibers contained some particles aggregates of several µm (Figure 4), they were well packaged inside the fibers suggesting no particle detachment after implantation. This good packaging suggests an attractive electrostatic interaction between the PLA and the particles, which is important to integrate the mechanical properties of the particles into the scaffold. This attractive interaction may have affected in the fiber diameter reduction. On the other hand, we observed a random fiber distribution for all scaffolds.

Tensile-strain tests (Figure 5A, Table 2) showed that the scaffolds containing the particles (PLA+P30 and PLA+P30+P55) were mechanically weaker than the pure PLA ones. We attributed this significant decrease to the high amount (≥60%) of particles in the fibers, which most likely reduced and disrupted the continuity of the polymer matrix reducing its capacity to withstand a given stress. We also attribute a contribution in the decrease of the mechanical properties to a PLA fiber diameter reduction, observed in the FE-SEM images (Figure 4). Mechanically speaking, such load of particles does not seem a proper choice to support the stress that bone is submitted. However, we must consider that in tissue regeneration the aim is to stimulate the own body to restore the tissue mechanics and functions rather than to create an ideal substitute, as long as the scaffold withstands the stress of implantation and the hydrostatic pressure of the body [24]. Looking at the osteoid (the unmineralized organic matrix prior to the maturation of bone tissue) our scaffolds had similar mechanical properties [25]. In this thesis, we were focused on increasing the bioactive potential of the scaffolds to accelerate the bone healing process. Since the mechanical properties of the scaffolds allowed their proper

manipulation in the biological experiments (see next sections), we decided to maintain such load of particles and therefore increase the ion release and bioactivity of the scaffolds.

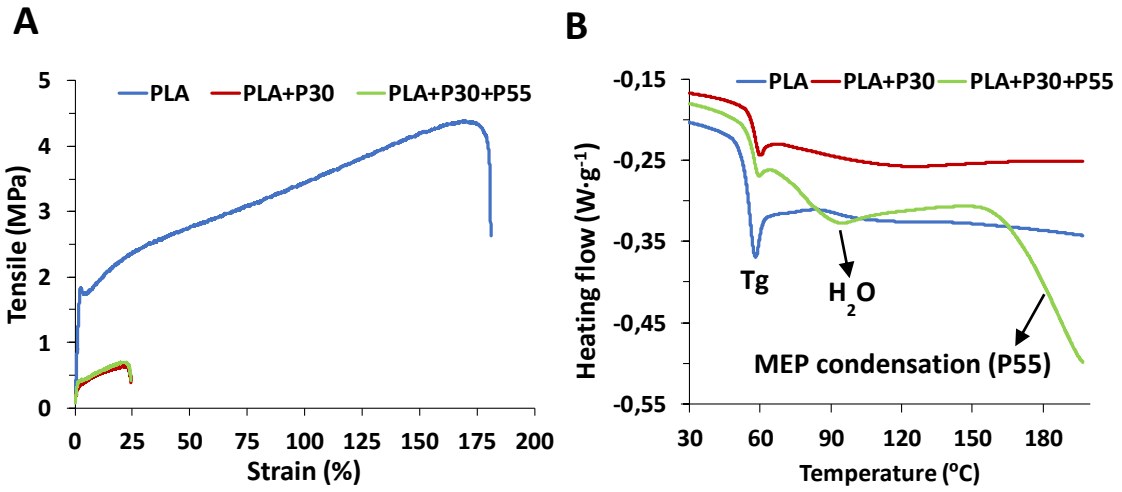

Figure 5. Tensile-strain tests **A)** and differential scanning calorimetry (DSC) measurements **B)** of the different scaffolds.

Table 2. Young's modulus (E), ultimate strength (σ_{Max}), strain to failure (ε_{Max}) and PLA glass transition temperature (Tg) of the different scaffolds.

	E (Mpa)	σ_{Max} (Mpa)	ε_{Max} (%)	Tg (ºC)
PLA	93.4±2.46	4.56±0.27	172.4±8.6	57.8
PLA+P30	19.9±0.9	0.63±0.11	25.9±5.8	58.0
PLA+P30+P55	27.8±1.0	0.69±0.10	25.7±7.5	58.5

On the other hand, the DSC results (Figure 5B, Table 2) showed a similar PLA glass transition temperature (Tg) for all the scaffolds. The absence of crystallization temperature indicates that the PLA in all the scaffolds was amorphous. Both results show up that the partial dissolution of the particles during the electrospinning technique did not

alter the PLA molecular length. Therefore, the observed changes in the mechanical properties (Figure 5B, Table 2) and fiber diameter (Figure 4) were induced more likely by the high amount of the particles in the scaffolds. We observed a significant amount of water for the scaffolds containing the particles (Figure 5B), even though we lyophilized the samples before analysis. This indicates a high affinity of the particles to absorb water, especially for P55 particles. We also observed the calorimetric loss of the decomposition of ethoxides and phosphate condensation of the MEP present in the P55 particles at ~160 ºC, indicating that the condensation process started at lower temperatures than the 200 ºC used in Chapter 2 section 2.2.2..

3.3.2. Ion release and pH modifications of the scaffolds in regular (RM) and osteogenic (OM) media after seeding hMSCs.

The release of bioactive ions (e.g. Ca^{2+}, PO_4^{3-}) and pH changes play an important role in the biological behavior of cells. We measured the ion release and pH modification of the different PLA nanofiber scaffolds in regular (RM) and osteogenic media (OM) after seeding hMSCs (Figure 6). Notice that we expressed the real ion concentration in the medium, not the cumulative one, since we considered this to have an effect in the hMSCs behavior. For cumulative ion release please refer to Figure 7. We chose the P55-RT particles to release high initial Ca^{2+} amounts due to their high solubility without pH alterations (Chapter 2, Figure 12). On the other hand, we used the P30-350ºC particles to release sustained Ca^{2+} amounts. We chose P30-350ºC particles over P0-350ºC particles, even having P30-350ºC a lower Ca^{2+} release profile (Chapter 2, Figure 14A) because P0-350ºC were insoluble in cell culture conditions (Figure 8).

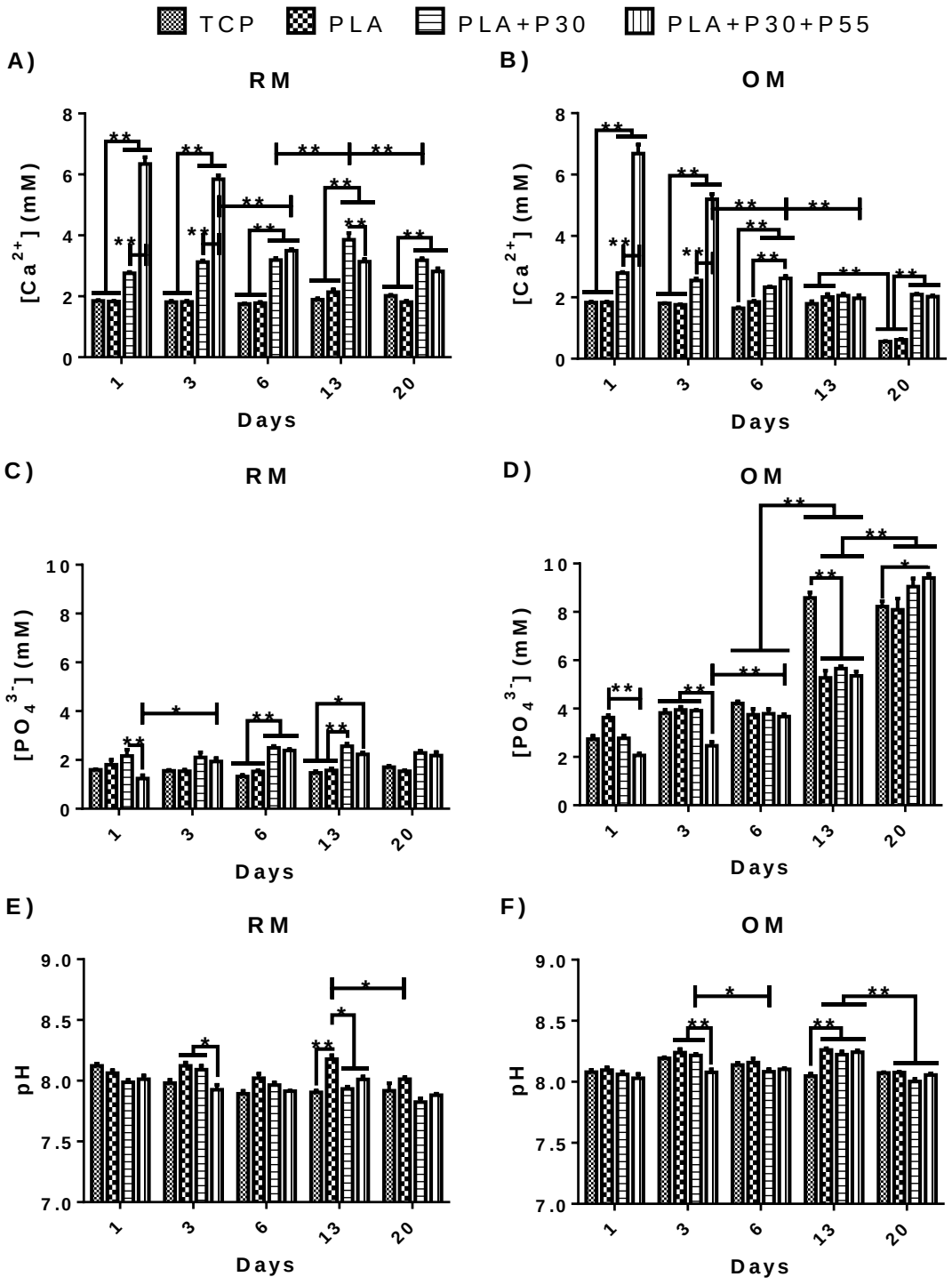

Figure 6. $[Ca^{2+}]$, $[PO_4^{3-}]$ and pH modifications of the different PLA nanofiber scaffolds after seeding hMSCs in RM and OM (n=4). Media was replaced every time point. We only considered P_{value}<0.001 (*) or <0.0001 (**) due to the high number of statistical differences.

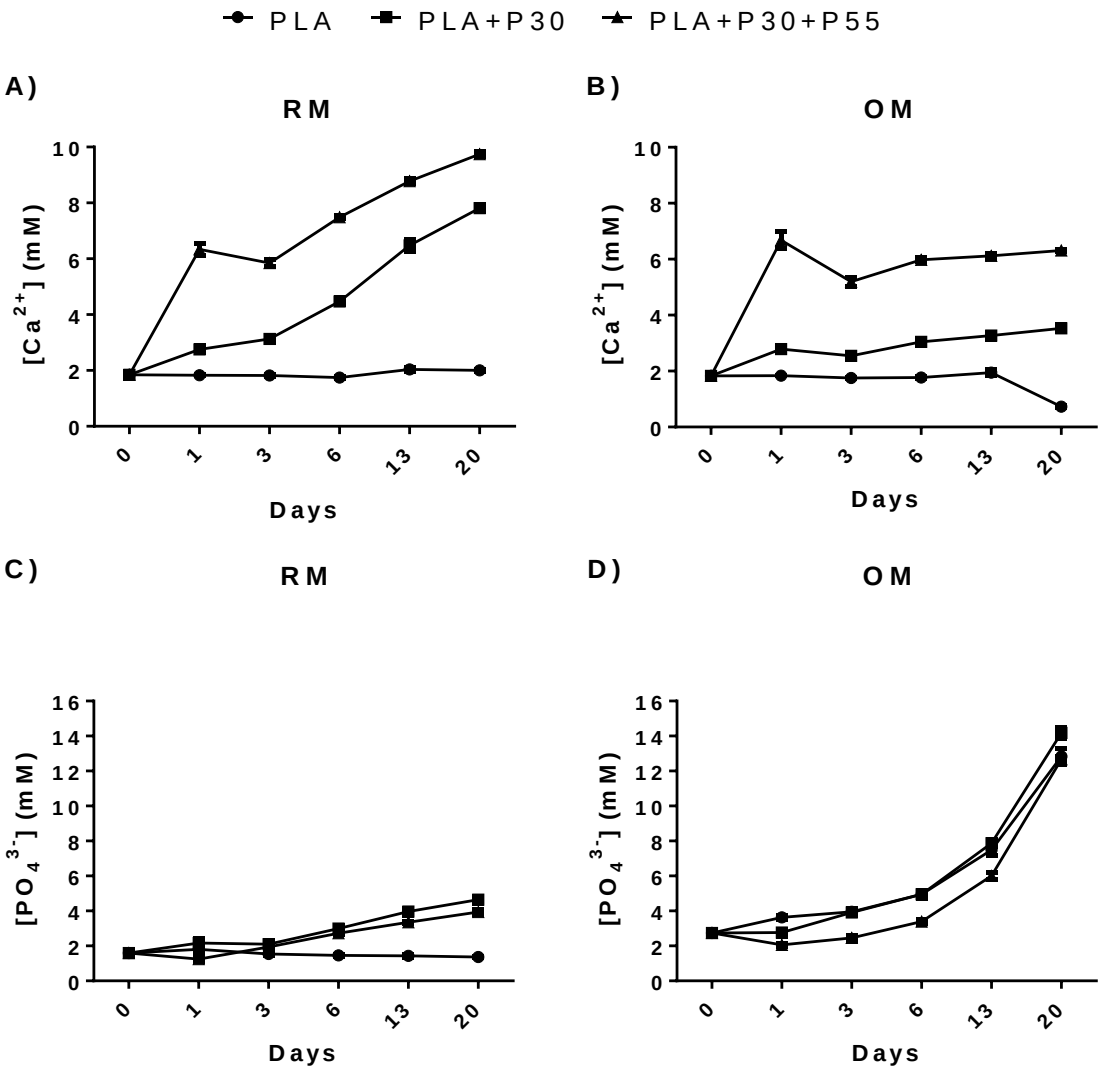

Figure 7. Cumulative Ca^{2+} and PO_4^{3-} release from Figure 6. Notice that the high increase in the PO_4^{3-} release in the OM is attributed to an increase in the ALP activity of the hMSCs.

We hypothesized that the presence of $HCO_{3(aq)}^{-}$ in the cell medium, and the $CO_{2(g)}$ atmospheric saturation of the incubator avoided the dissolution of the $CaCO_3$ present in the P0-350ºC particles [26]. Moreover, P30-350ºC particles also released PO_4^{3-}, which we considered positive due to its participation in bone mineralization. Returning to the scaffolds ion release results, we observed that the PLA+P30+P55 scaffolds released high initial amounts of Ca^{2+} during the 3 first days (Figure 6A), confirming the high solubility of the P55 particles. Then both scaffolds (PLA+P30 and PLA+P30+P55)

released about the same amount of Ca^{2+} and PO_4^{3-} (Figure 6A, 6C) due to the presence of the more stable P30 particles. The lack of PO_4^{3-} burst at day 1 and 3 for the PLA+P30+P55 scaffolds was attributed to the release of MEP by the dissolution of the P55 particles (Figure 3).

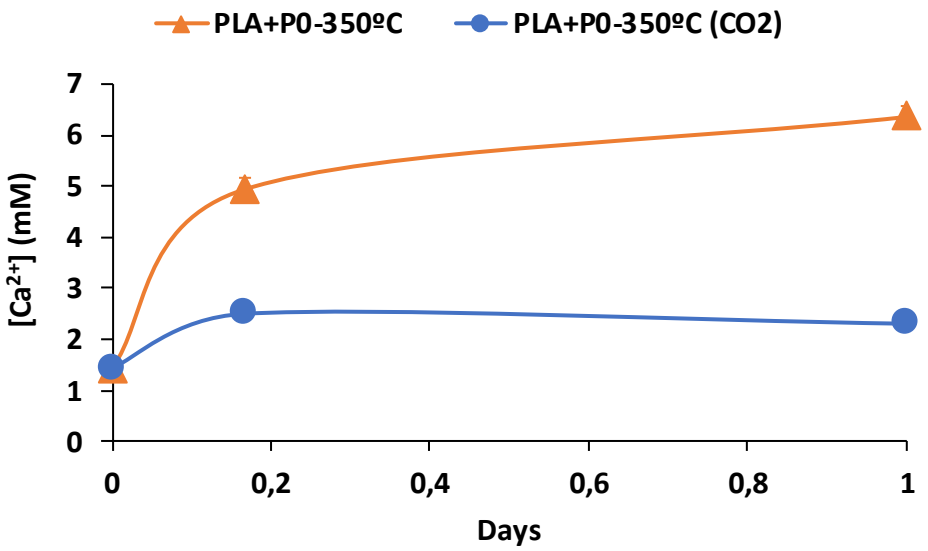

Figure 8. Cumulative Ca^{2+} release of PLA nanofiber scaffolds containing a 20% of P0-350ºC particles, immersed in 0.05 M HEPES buffered media (pH 7.4) plus ~1.4 mM $CaCl_2$ at 37 ºC. Fibers were incubated separately in normal (PLA+P0-350ºC) and 5% $CO_{2(g)}$ incubators (PLA+P0-350ºC (CO2)). We observed the absence of Ca^{2+} release in the presence of 5% $CO_{2(g)}$, suggesting that its absorption in the medium avoided the dissolution of the P0-350ºC particles.

The pure PLA fibers showed similar Ca^{2+} and PO_4^{3-} values than the tissue culture plate (TCP), indicating no Ca^{2+} or PO_4^{3-} absorption by the PLA fibers. Notice that the media initially contained about 1.8 mM of Ca^{2+} and 1.6 mM of PO_4^{3-}. The higher PO_4^{3-} concentration for the PLA scaffolds and the TCP at day 1 in the OM (Figure 6C, 6D), is attributed to the presence of β-glycerophosphate. The Ca^{2+} and PO_4^{3-} release by the scaffolds in the OM was similar than in the RM during the 6 first days (Figure 6B, 6D), demonstrating that the scaffolds could maintain such ion concentration in an osteogenic

environment. Then we observed a significant decrease of the Ca^{2+} concentration in the OM that suggests a Ca^{2+} precipitation. This precipitation matches with an increase in the PO_4^{3-} concentrations from day 13 (Figure 6D) that we correlate with an increase in the ALP activity of the hMSCs. The Ca^{2+} concentration values in both RM and OM were in the described range to stimulate the extracellular calcium-sensing receptor (CaSR) involved in cell chemotactic responses such as cell migration, proliferation or angiogenesis [4,5]. We did not observe changes in the pH for any condition, validating their use for biomedical applications (Figure 6E, 6F). Notice that the pH values were slightly basic because they were measured outside the incubator where the lower $P_{CO2(g)}$ affected in the $CO_{2(g)}/HCO_{3^-(aq)}$ buffer equilibrium of the medium.

3.3.3. hMSCs adhesion and proliferation

hMSCs are present in many tissues and have the ability to differentiate into different cell types. One of these differentiated hMSCs are osteoblast, the cells in charge of extracellular matrix production in bone remodeling and bone healing. For this reason, hMSCs are object of study for bone regenerative applications. Moreover, hMSCs participate in the formation of blood vessels releasing several angiogenic factors that guide endothelial cells to produce blood vessels. We measured the hMSCs adhesion and proliferation from section 3.3.2.. We observed that the presence of the particles enhanced the hMSCs adhesion in both RM and OM (Figure 9A, 9B). Notice that the lower cell adhesion in the OM is attributed to a cell loss during the seeding process. The lack of relevant differences between the PLA+P30 and the PLA+P30+P55 scaffolds suggests that the P55 particles and hence higher initial Ca^{2+} concentrations (Figure 6A, 6B) did not increase cell adhesion. The hMSCs proliferation results showed a low increase in RM (Figure 9C), which was unexpected due to the high proliferative capacity of MSCs. However, the absence of significant differences with the TCP discards the

scaffolds as the responsible. Some *in vitro* studies have shown low hMSCs proliferative rates indicating that hMSCs not always have a strong proliferative behavior [27–29].

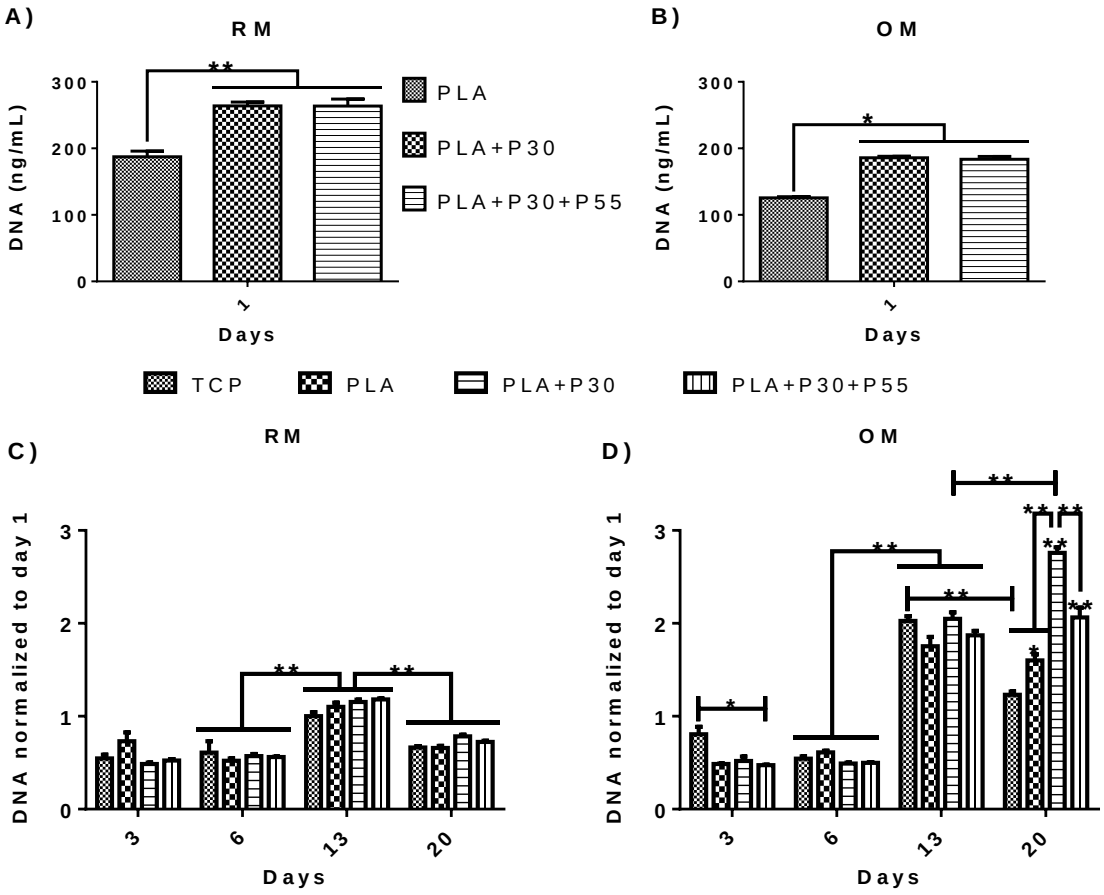

Figure 9. hMSCs adhesion **A), B)** and proliferation **C)**, **D)** on the PLA nanofiber scaffolds in RM and OM (n=4). P_{value}<0.001 (*), <0.0001 (**). Stars (*) on columns refer to differences with the TCP.

In contrast, we observed a significant higher proliferation when the hMSCs were cultured in the OM (Figure 9D), which was neither expected since the differentiation of hMSCs should decrease cell proliferation. However, we must consider that the osteogenic differentiation of hMSCs is a long process that takes several steps and some of them may allow cell proliferation. Moreover, in accordance to some studies, the dexamethasone present in the OM induces hMSCs proliferation [30–35]. We observed a significant higher hMSCs proliferation on the fibers containing the particles than on the

pure PLA ones and the TCP at day 20 in OM (Figure 9D), indicating that the presence of the particles increased the hMSCs proliferation in OM. The lower proliferation observed at the same day for the PLA+P30+P55 scaffolds compared to the PLA+P30 suggests that the initial increase in Ca^{2+} concentration (Figure 6B) did not increase the hMSCs proliferation.

3.3.4. Increase in the ALP activity

Alkaline phosphatase (ALP) is an enzyme early expressed in the osteogenic differentiation of hMSCs. It participates in bone mineralization, increasing the local concentration of PO_4^{3-}. Its early expression is the reason of being one of the most measured markers to identify the osteogenic differentiation of hMSCs. We measured the ALP activity of the hMSCs from the previous sections. As expected, we only observed an increase in the ALP activity in the OM (Figure 10B), suggesting that the scaffolds were not osteoinductive but supported the differentiation of hMSCs in an osteogenic environment. However, the ALP activity did not increase until day 13, being in accordance with the increase in the PO_4^{3-} concentration (Figure 6D). Although, it is standardized that the ALP activity normally rises at earlier stages, some studies also reported late increases [33,34,36,37]. It is difficult to stablish a standard pattern for the ALP activity or other metabolic activities (e.g. cell proliferation) since hMSCs biology can present big differences depending, for instance, on donor metabolism, heterogeneity of the extracted cell population or type of serum used [38–40]. We observed that the PLA+P30 scaffolds supported the highest increase in the ALP activity at day 20 in OM (Figure 10B) suggesting that the P30 particles induced a stronger differentiation. Again, we failed to observe that the initial increase of $[Ca^{2+}]$ induced by the PLA-P30-P55 scaffolds (Figure 6A) had a positive effect in the increase of ALP activity.

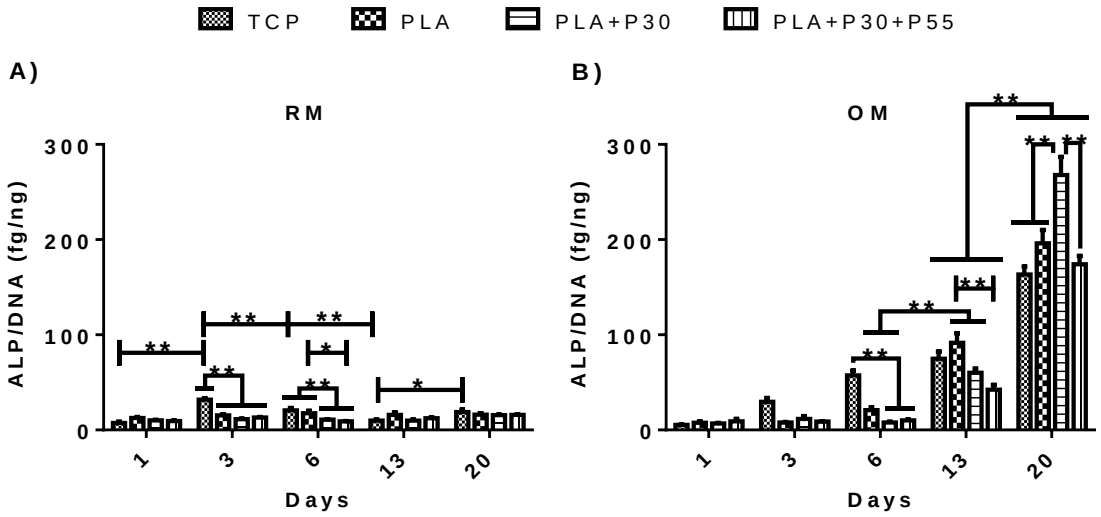

Figure 10. Increase of ALP activity by the hMSCs seeded in the different PLA nanofiber scaffolds in RM **A)** and OM **B)** (n=4). P_{value}<0.001 (*), <0.0001 (**).

3.3.5. L-lactate production

We measured the L-lactate released by the PLA nanofibers (Figure 11) since L-lactate have been reported to be angiogenic [41–44]. However, the L-lactate concentration in the media was overly too high to only stem from the dissolution of the PLA nanofibers. We assigned these high values to the production of L-lactate by the own hMSCs. It has been reported that hMSCs undergo anaerobic glycolysis increasing the [L-lactate] even in normoxia conditions due to their adaptation to hypoxia stresses *in vivo* [45–47]. We normalized the L-lactate concentration by the total DNA since it was cell dependent. Notice that we considered insignificant the L-lactate released by the fibers. We observed that the L-lactate production in RM (Figure 10A) was statistically higher in all the scaffolds than in the TCP, indicating a higher metabolic activity due to a scaffold-hMSCs interaction. After 6 days, we detected a lower L-lactate production for the pure PLA scaffolds without particles, indicating that the P30 particles prolonged this higher hMSCs metabolic activity.

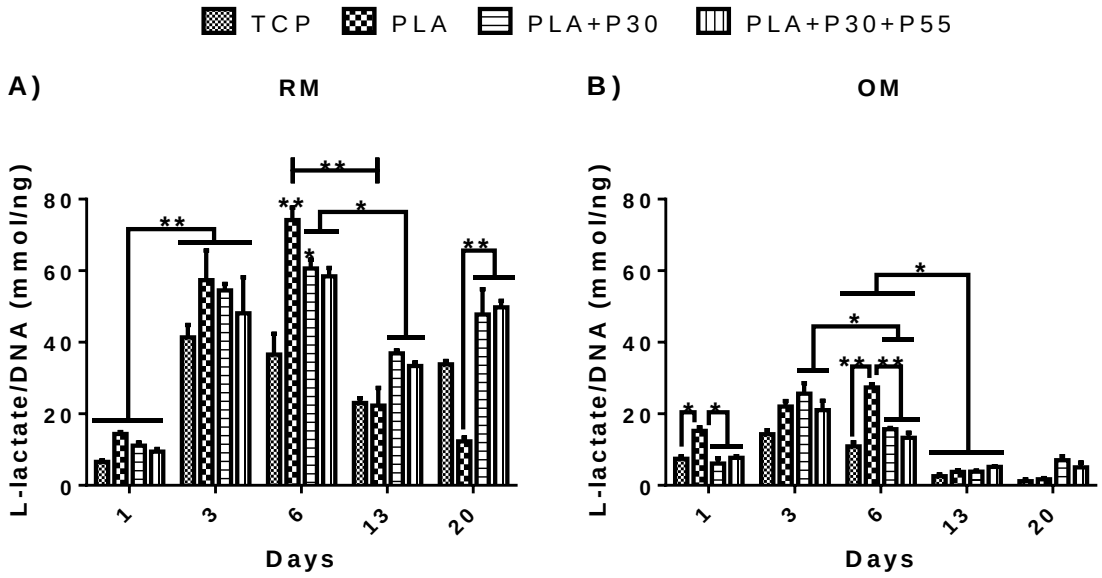

Figure 11. L-lactate production by the hMSCs seeded on the different PLA nanofiber scaffolds in RM **A)** and OM **B)** (n=4). P_{value}<0.001 (*), <0.0001 (**).

L-lactate has been identified as an angiogenic promoter for both wound healing and brain [41–44]. Hence releasing high amounts of L-lactate may stimulate the formation of initial vasculature. The decrease in L-lactate production in OM (Figure 11B) indicates that even though we did not observe an increase in the ALP activity until day 13 (Figure 10B), from day 3 the metabolic activity of the hMSCs was completely different, suggesting cell differentiation at earlier stages. Indeed, it has been reported a decrease in the anaerobic glycolysis for the osteogenic differentiation of hMSCs, which results in a decrease of the L-lactate production [45,46]. The decrease of L-lactate concentration for all conditions from day 13 in both media matches with an increase in cell proliferation (Figure 9C, 9D) and ALP activity (Figure 10B), suggesting a close correlation.

3.3.6. VEGF synthesis

Vascular endothelial growth factor (VEGF) is one of the most well-known angiogenic factors that regulates the formation, maintenance and sprouting of blood vessels [48]. hMSCs are known to participate in the stimulation of new vasculature by synthesizing different growth factors, among them the VEGF [6,49,50]. Therefore, we measured the synthesized VEGF by the seeded hMSCs as an *in vitro* marker of the angiogenic potential of the scaffolds (Figure 12).

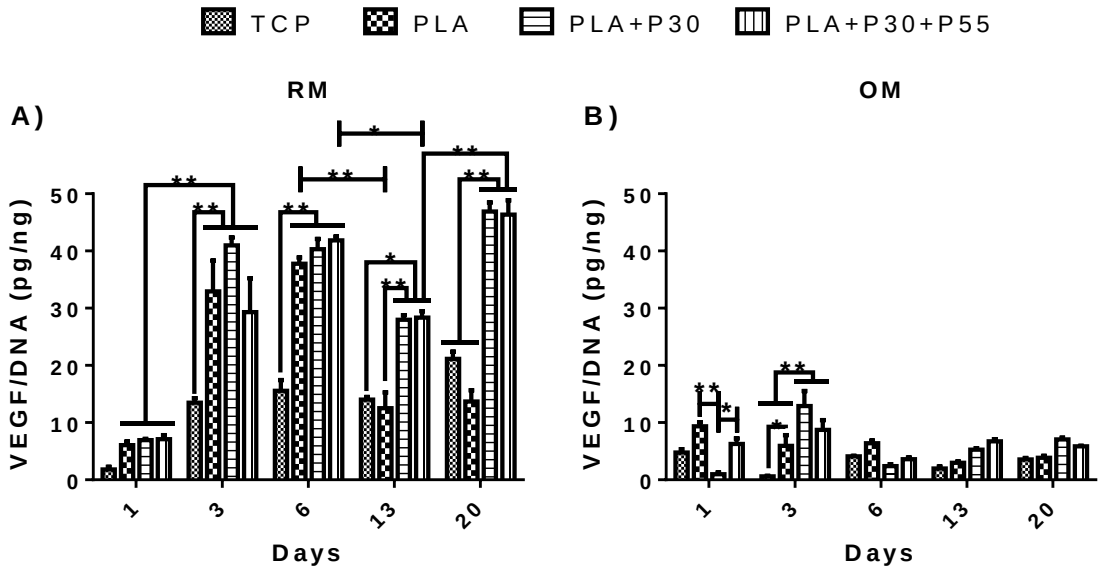

Figure 12. VEGF synthesis by the hMSCs seeded on the different PLA nanofiber scaffolds in RM **A)** and OM **B)** (n=4). P_{value}<0.001 (*), <0.0001 (**).

We observed that the VEGF synthesis followed an almost identical tendency than the L-lactate production (Figure 11). It has been stated for wound healing that the release of high amounts of L-lactate may induce to the hMSCs the biological perception of a hypoxia state even in normoxia conditions [42]. This can activate several angiogenic mechanisms among them the synthesis of VEGF [42]. The high VEGF synthesis in RM by all the scaffolds in comparison to the TCP until day 6 (Figure 12A) suggests a high

angiogenic potential. However, only the particle-containing scaffolds prolonged higher [VEGF] until day 20. We could not correlate an increase in the VEGF synthesis with a [Ca^{2+}] increase (Figure 6A, 6B). Nevertheless, the angiogenic effects of the released L-lactate [41–44] may have masked those from the Ca^{2+} [4]. The low synthesis of VEGF in the OM (Figure 12B) suggests a lower angiogenic stimulation due to the osteogenic differentiation of the hMSCs. However, we must consider that the formation of blood vessels is a complex process that involves other parameters apart from hMSCS and the synthesis of VEGF.

3.3.7. HUVECs tube formation assay

In angiogenesis, endothelial progenitor cells are assembled together producing a tube-like network structure that later will mature into micro blood vessels [51]. This network producing capacity is evaluated *in vitro* to test the angiogenic potential or inhibition of different substances. Human umbilical vein endothelial cells (HUVECs) are widely used for this purpose since they are from a human origin and easy to obtain. Here (Figure 13), we evaluated the tube network assembly of HUVECs after being cultured during 8 h with extractions of the regular media (ERM) from the previous experiments (sections 3.3.2. to 3.3.6.). The OM was discarded for this assay due to the significant lower VEGF synthesis by the hMSCs (Figure 12B). We used the free available ImageJ plugin Angiogenesis Analyzer [15] to evaluate the quality of the produced tube network. Selected images of the assay (Figure 13) showed that the HUVECs only produced tubes when they were cultured with the ERM, indicating that the release of pro-angiogenic factors by the hMSCs was crucial. The absence of tubes when the HUVECs were cultured just with regular medium (RM) validates this condition as a negative control (NC).

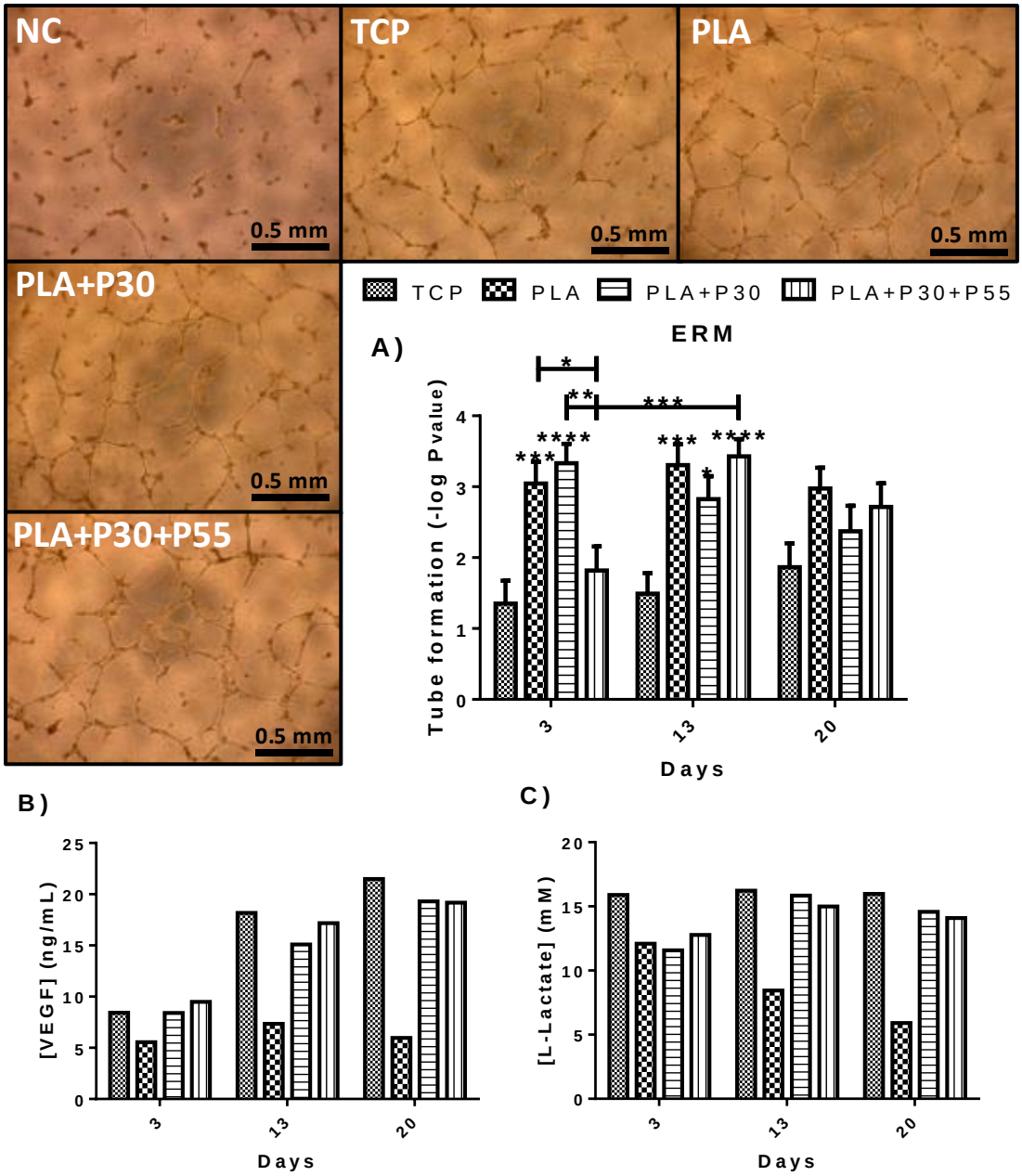

Figure 13. Selected images of the HUVECs forming tubes after being 8 h with the extracted RM (ERM) form section 3.3.2.. Negative control (NC) consisted of regular medium (RM). Quantification of the quality of the tube network using the Angiogenesis Analyzer ImageJ plugin [15] **A)** (n=4). For more information about the analysis please refer to Figure 14. Total VEGF **B)** and L-lactate concentration **C)** of the different ERM. The absence of SEM in **B)** and **C)** is due to the media from the different conditions were pooled before the assay (see section 3.2.5.4.). P_{value}<0.5 (*), < 0.01 (**), <0.001 (*), <0.0001 (**). Stars (*) on columns refer to differences with the TCP.

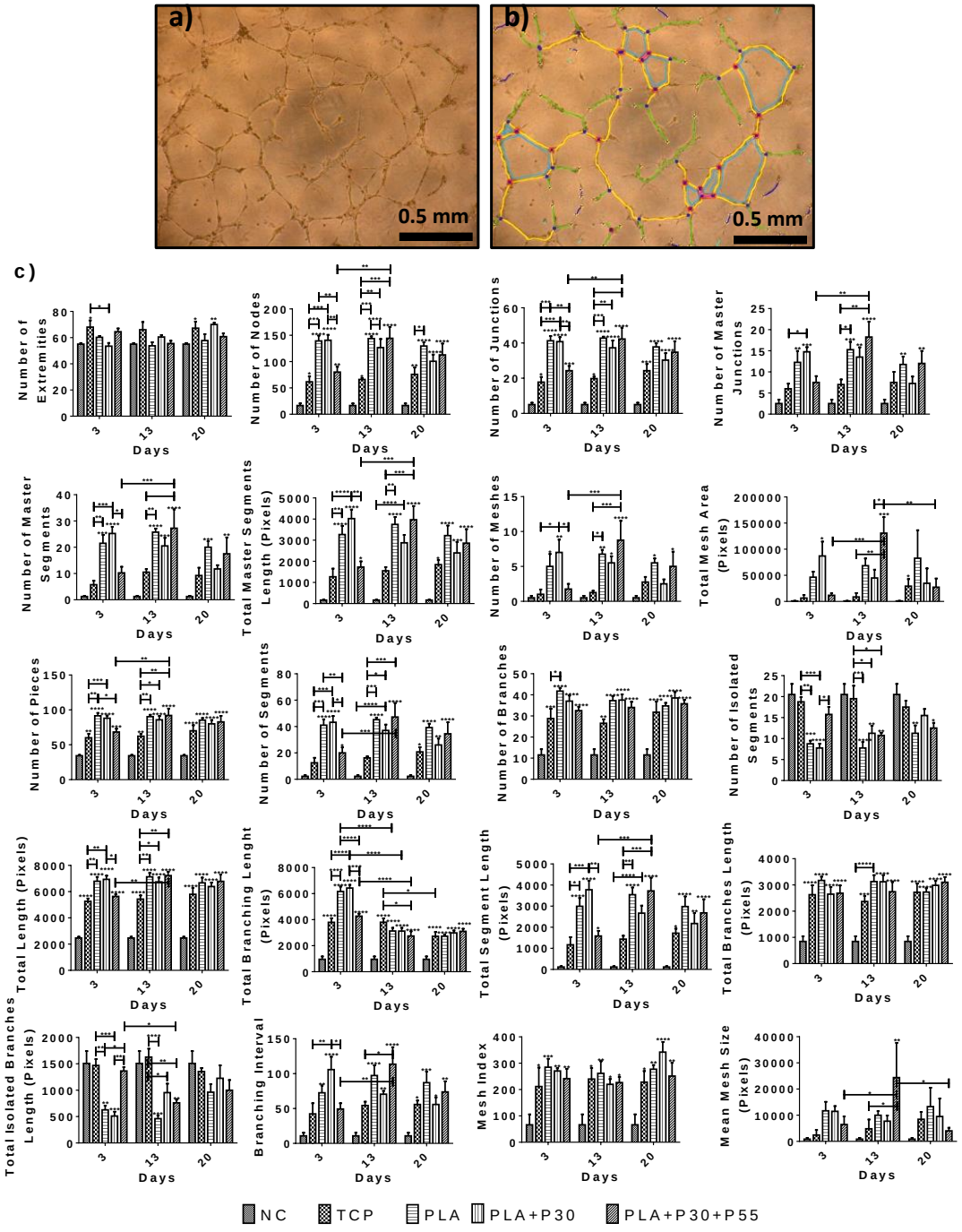

Figure 14. Selected image of the HUVECs forming tubs before **A)** and after **B)** being analyzed with the Angiogenesis Analyzer ImageJ plugin [15]. The different parameters measured by the plugin **C)** (n=4). We used the average of the significant difference (P_{value}) with the negative control (NC) of the different parameters, to quantify the quality of the tube network in Figure 13A. We considered all the parameters as equal important. P_{value}<0.5 (*), < 0.01 (**), <0.001 (*), <0.0001 (**). Stars (*) on columns refer to differences with the NC.

Analyzing the images with the Angiogenesis Analyzer (Figure 13A), we quantified a statistical better tube formation for the ERM from the different scaffolds at day 3 and 13 than for the ERM from the TCP. This indicates that the contact hMSCs-scaffold induced a significant higher angiogenic response. We attributed the lower tube formation for the PLA+P30+P55 scaffolds at day 3 to a possible cytotoxic effect of the released MEP (Figure 3). The failure in observing cytotoxicity for this scaffold with hMSCs (Figure 9) suggests that the HUVECs were much more sensitive to this compound. The lower tube formation for the ERM from the scaffolds at day 20 suggests a normalization of the angiogenic-promoting effects and a return to a normal state, which we considered positive since an excessive blood vessel formation can indicate an abnormal stimulation (e.g. tumors) [52]. We could not correlate the tube formation results with an increase in the VEGF concentration (Figure 13B). Notice that this time the VEGF was not normalized by the total hMSCs DNA since it was considered the total VEGF concentration to have an effect in angiogenesis. Although, VEGF is a known angiogenic factor some studies have shown it failed to induce *in vitro* tube formation [48,53,54]. It has been described that the VEGF has a role in HUVECs migration, proliferation and tube-maintenance, avoiding blood vessel regression rather than stimulating their production [48], and only when it was combined with other angiogenic factors such as basic fibroblast growth factor (bFGF) or tumor necrosis factor (TNFα) positive results regarding tube formation were observed [53]. We could neither correlate the enhancement of tube formation with an increase of Ca^{2+} (Figure 6A) or total L-lactate concentration (Figure 13C), two known angiogenic ions [4,5,43,44], which reinforces the hypothesis that other released angiogenic factors participated in the tube formation.

3.3.8. Formation of initial vasculature in the CAM model

The CAM model is a widely used pre-*in vivo* test to evaluate the formation of blood vessels [16]. It is not subjected to the strict regulations of *in vivo* experiments due to the incapacity of the chick embryo to feel pain during the two first weeks. This facilitates and reduces the cost of the experiment, making it available for most research groups. In this section, we used the CAM model to evaluate the stimulation of new vasculature by the different PLA nanofiber scaffolds (Figure 15). We excluded the PLA+P30 scaffolds due to the complexity of the experiment. We used an own developed Image macro to identify and quantify the formation of new blood vessels (Figure 16). Analyzing the results (Figure 15), we observed that the PLA+P30+P55 scaffolds had a similar response than a VEGF-loaded PLA positive control (PLA+VEGF). On the other hand, the pure PLA nanofibers showed a statistical lower amount of blood vessel, validating the PLA+VEGF as a positive control and indicating that the particles induced a similar response that such angiogenic VEGF doses [55,56]. We did not observe statistical differences between the PLA and PLA+P30+P55 scaffolds. However, having the initial hypothesis that the particles will increase the formation of blood vessels, the one tailed t-test showed that the PLA+P30+P55 scaffolds induced a statistical higher amount [17]. We must also consider that the release of L-lactate by the PLA may have smoothen such differences due to its angiogenic effect [41–44]. These results indicate that even having similar results in the HUVECs tube formation assay (Figure 13A), the scaffolds showed differences when implanted in an *in vivo*-like environment. This supports the statement that other factors apart from endothelial cells and the release of angiogenic factors (e.g. VEGF) by MSCs were involved in the formation of blood vessels. We also decided to implant the scaffolds with hMSCs (Figure 15) since we observed that they released significant amounts of VEGF (Figure 12A). Moreover, it has been identified a crosstalk between endothelial cells and MSCs in the formation of blood vessels [49,50].

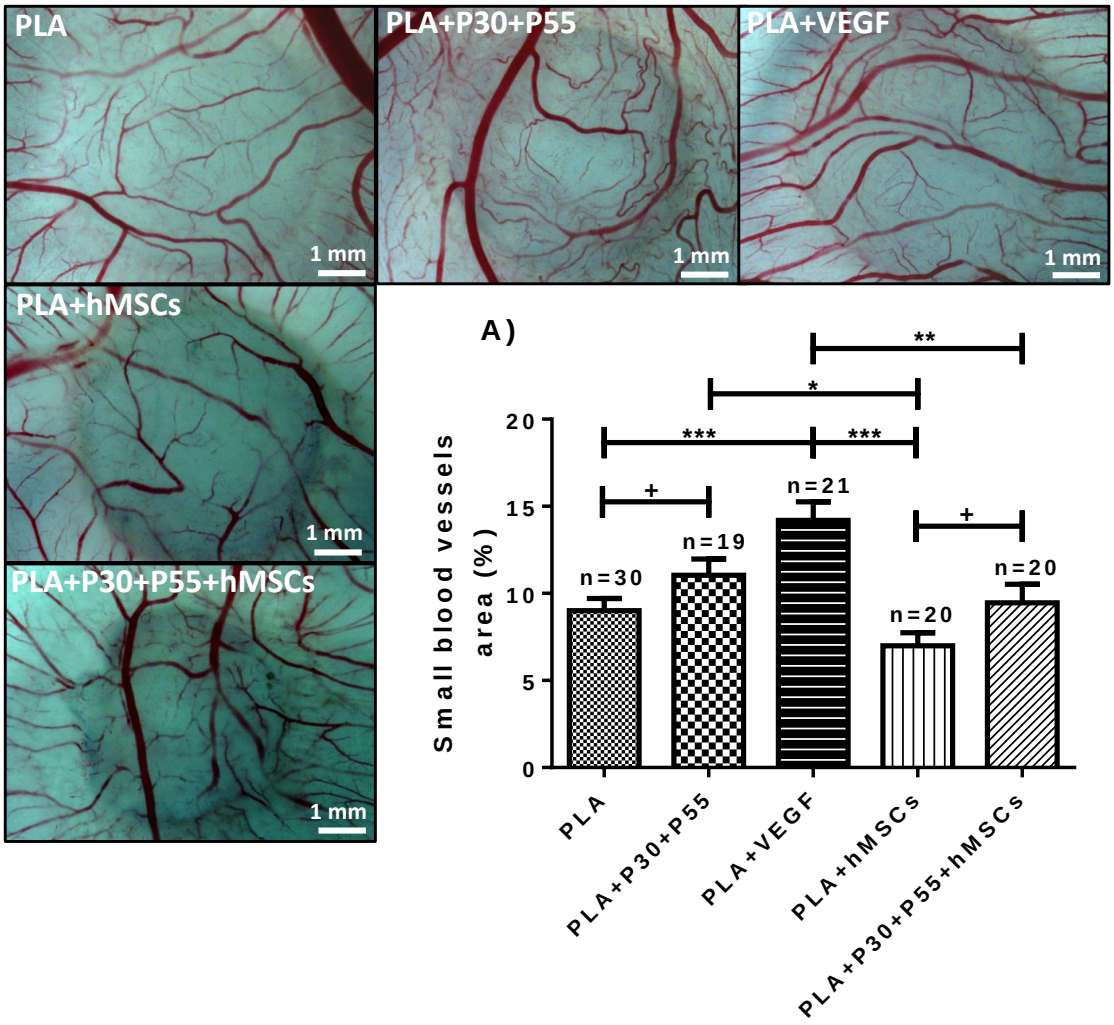

Figure 15. Selected images of the different scaffolds showing the formation of blood vessels in the CAM model. Quantification of the small blood vessels within the area of the scaffolds using an own developed ImageJ macro **A)**. "+" marked statistical differences following a one-tailed t-test. For more information about the macro please refer to Figure 16. P_{value}<0.5 (*/+), < 0.01 (**), <0.001 (*), <0.0001 (**).

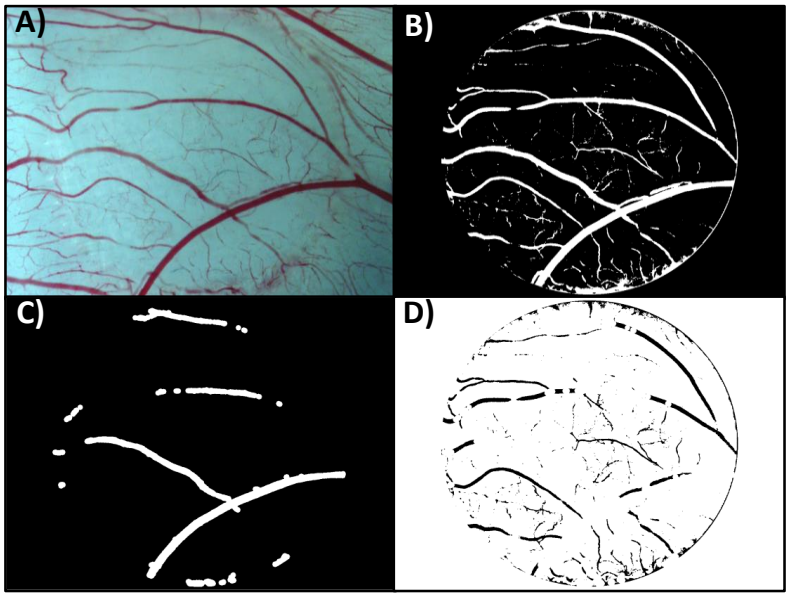


```
rename("original");
run("Split Channels");
selectWindow("original (red)");
run("Close");
selectWindow("original (blue)");
run("Close");
selectWindow("original (green)");
beep();
waitForUser("Select your scaffold");
run("Cut");
newImage("Untitled", "8-bit black", 1360, 1024, 1);
run("Paste");
selectWindow("original (green)");
run("Close");
run("Set Scale...", "distance=0 known=0 pixel=1 unit=pixel");
run("Measure");
run("Set Scale...", "distance=0 known=0 p.ixel=1 unit=pixel");
selectWindow("Untitled");
run("Enhance Contrast...", "saturated=0.3 equalize");
run("Invert");
run("Subtract Background...", "rolling=50");
run("Auto Threshold", "method=IsoData white");
run("Duplicate...", " ");
run("Canvas Size...", "width=1360 height=1024 position=Center zero");
run("Gray Morphology", "radius=8 type=circle operator=open");
setOption("BlackBackground", false);
run("Erode");
imageCalculator("Subtract create", "Untitled", "Untitled-1");
run("Invert");
run("Analyze Particles...", "exclude include summarize add");
```

Figure 16. ImageJ macro used to analyze the CAM images in Figure 15. CAM image before analysis **A)**. Analyzed images showing all the blood vessels **B)**, the big ones **C)** and the difference **D)** between **B)** and **C)**. The macro quantified the pixels from **D)** and from the total area analyzed (selected circle). We normalized **D)** by the total area analyzed. The area occupied by **C)** was subtracted from the total area analyzed since

the big blood vessels were considered artifacts. Notice that the resolution of the macro must be set to the one of the image (here 1360x1024). Parameters like "rolling" and "Auto Threshold" can be adjusted to fit better the images. However, all images must be treated following the same parameters. Here, we used "rolling=50" and "IsoData white". "Radius=8" extracted the big blood vessels (it can be adjusted). The higher the "Radius" the lower the size of the big blood vessels extracted. We used "radius=40" to know the pixels occupied by **B)** and then we calculated the ones from **C)**. The macro was mainly developed by Irene Cano Torres, a PhD candidate from the same research group.

We implanted the scaffolds after 13 days of culture with the hMSCs because it was then when we started to observe significant differences in the VEGF released between both scaffolds (Figure 12A). Surprisingly, we observed that even releasing high amounts of VEGF, the presence of hMSCs decreased the formation of blood vessels (Figure 15), which was unexpected considering the angiogenic stimulation of the PLA+VEGF positive control. However, the amount of the VEGF released by the hMSCs *in vitro* (~5-20 ng/mL, Figure 13B) was significantly smaller than the one from the PLA+VEGF condition (200 ng/30 µL, see section 3.2.6.). We hypothesize that the hMSCs may have died during the CAM experiment by an incorrect supply of nutrients, affecting negatively to the formation of blood vessels. Another hypothesis is that the formation of extracellular matrix (ECM) by hMSCs and the cleaning of the scaffolds during 13 days of culture prior to the CAM implantation may have produced a more biocompatible structure that did not need as many blood supply, or that the penetration of the blood vessels within this ECM difficulted its image analysis. In any case, these results suggest that the incorporation of cells may not be a positive choice for the stimulation of initial vasculature and hence a better *in vivo* integration of the scaffolds [57–59]. Despite the lower blood vessel production, we

observed again a significant higher amount of blood vessels for the scaffolds containing the particles (Figure 15), validating once more their angiogenic potential.

3.4. Conclusions

We developed a cost-effective scaffold with angiogenic properties and a promising potential in the regeneration/integration of bone and highly vascularized softer tissues. The scaffolds released substantial amounts of Ca^{2+} and PO_4^{3-} over long periods and consisted of electrospun PLA nanofibers with embedded degradable CP nanoparticles synthesized by the sol-gel method. We showed a good biocompatibility of the scaffolds with hMSCs and a neutral pH under culture condition. Based on the hypothesis that the release of Ca^{2+} would stimulate the formation of blood vessels, we identified that the presence of degradable CP nanoparticles enhanced several angiogenic parameters such as; the VEGF synthesis by hMSCs, the formation of tubes by HUVECs and the production of similar amounts of blood vessels than angiogenic VEGF doses in the CAM model. However, we could not correlate such results with increases in the Ca^{2+} concentration. Parallelly, we observed that the presence of the particles increased the metabolic activity of hMSCs, resulting in the production of high amounts of L-lactate. The high L-lactate concentrations may have had also a role in the observed angiogenic stimulation, masking the effects of the Ca^{2+}. The particles also increased the ALP activity of hMSCs in an osteogenic medium, suggesting a stronger osteoinductive potential and validating their use for bone regenerative applications. However, there was a reduction in the VEGF synthesis that suggests a lower blood vessel stimulation in osteogenic-like environments.

3.5. References

[1] H. Oliveira, S. Catros, O. Castano, S. Rey, R. Siadous, D. Clift, J. Marti-Munoz, M. Batista, R. Bareille, J.A. Planell, E. Engel, The proangiogenic potential of a novel calcium releasing composite biomaterial : Orthotopic in vivo evaluation, Acta Biomater. 54 (2017) 377–385. doi:10.1016/j.actbio.2017.02.039.

[2] A. Malhotra, P. Habibovic, Calcium Phosphates and Angiogenesis: Implications and Advances for Bone Regeneration, Trends Biotechnol. 34 (2016) 983–992. doi:10.1016/j.tibtech.2016.07.005.

[3] A. Barradas, H. Yuan, C. van Blitterswijk, P. Habibovic, Osteoinductive biomaterials: current knowledge of properties, experimental models and biological mechanisms, Eur. Cells Mater. 21 (2011) 407–429. doi:10.22203/eCM.v021a31.

[4] A. Aguirre, A. González, M. Navarro, Ó. Castaño, J.A. Planell, E. Engel, Control of microenvironmental cues with a smart biomaterial composite promotes endothelial progenitor cell angiogenesis, Eur. Cells Mater. 24 (2012) 90–106. doi:10.22203/eCM.v024a07.

[5] H. Oliveira, S. Catros, C. Boiziau, R. Siadous, J. Marti-Munoz, R. Bareille, S. Rey, O. Castano, J. Planell, J. Amédée, E. Engel, The proangiogenic potential of a novel calcium releasing biomaterial: Impact on cell recruitment, Acta Biomater. 29 (2016) 435–445. doi:10.1016/j.actbio.2015.10.003.

[6] C. Navarro-Requena, J.D. Weaver, A.Y. Clark, D.A. Clift, S. Pérez-Amodio, Ó. Castaño, D.W. Zhou, A.J. García, E. Engel, PEG hydrogel containing calcium-releasing particles and mesenchymal stromal cells promote vessel maturation, Acta Biomater. (2017). doi:10.1016/j.actbio.2017.12.009.

[7] J.R. Jones, Review of bioactive glass : From Hench to hybrids, Acta Biomater. 23 (2015) S53–S82. doi:10.1016/j.actbio.2015.07.005.

[8] M. Navarro, M. Ginebra, J. Clément, M. Salvador, A. Gloria, J.A. Planell, Physicochemical Degradation of Titania-Stabilized Soluble Phosphate Glasses for Medical Applications, J. Am. Ceram. Soc. 86 (2003) 1345–1352. doi:10.1111/j.1151-2916.2003.tb03474.x.

[9] K. Franks, I. Abrahams, J.C. Knowles, Development of soluble glasses for biomedical use part I: In vitro solubility measurement, J. Mater. Sci. Mater. Med. 11 (2000) 609–614. doi:10.1023/A:1008949527695.

[10] K. Lin, Y. Liu, H. Huang, L. Chen, Z. Wang, J. Chang, Degradation and silicon excretion of the calcium silicate bioactive ceramics during bone regeneration using rabbit femur defect model, J. Mater. Sci. Mater. Med. 26 (2015) 1–8. doi:10.1007/s10856-015-5523-2.

[11] B. Daley, A.T. Doherty, B. Fairman, C.P. Case, Wear debris from hip or knee replacements causes chromosomal damage in human cells in tissue culture., J. Bone Joint Surg. Br. 86 (2004) 598–606. doi:10.1302/0301-620X.86B4.14368.

[12] Advanced Chemistry Development (ACD), Inc., Toronto, ON, Canada, 2017, (n.d.). http://www.acdlabs.com/.

[13] H.J. Gitelman, An improved automated procedure for the determination of calcium in biological specimens, Anal. Biochem. 18 (1967) 521–531. doi:10.1016/0003-2697(67)90110-8.

[14] E. Gindler, J. King, Rapid colorimetric determination of calcium in biologic fluids with methylthymol blue, Am. J. Clin. Pathol. 58 (1972) 376–382. doi:10.1093/ajcp/58.5.376.

[15] G. Carpentier, Angiogenesis Analyzer for ImageJ, (2012). http://image.bio.methods.free.fr/ImageJ/?Angiogenesis-Analyzer-for-ImageJ&lang=en.

[16] E.I. Deryugina, J.P. Quigley, CHAPTER TWO: Chick Embryo Chorioallantoic Membrane Models to Quantify Angiogenesis Induced by Inflammatory and Tumor Cells or Purified Effector Molecules, Methods Enzym. 444 (2009) 21–41. doi:10.1016/S0076-6879(08)02802-4.

[17] GraphPad, index, One-Tail vs. Two-Tail P Values. (2018). https://www.graphpad.com/guides/prism/6/statistics/index.htm?one-tail_vs__two-tail_p_values.htm.

[18] R. Mathew, P.N. Gunawidjaja, I. Izquierdo-Barba, K. Jansson, A. García, D. Arcos, M. Vallet-Regí, M. Edén, Solid-State 31P and 1H NMR Investigations of Amorphous and Crystalline Calcium Phosphates Grown Biomimetically From a Mesoporous Bioactive Glass, J. Phys. Chem. C. 115 (2011) 20572–20582. doi:10.1021/jp206237n.

[19] J.P. Fletcher, R.J. Kirkpatrick, D. Howell, S.H. Risbud, 31P Magic-angle Spinning Nuclear Magnetic Resonance Spectroscopy of Calcium Phosphate Glasses, J. Chem. Soc. Faraday Trans. 89 (1993) 3297–3299. doi:10.1039/FT9938903297.

[20] D.M. Pickup, P. Guerry, R.M. Moss, J.C. Knowles, M.E. Smith, R.J. Newport, New sol–gel synthesis of a (CaO)0.3(Na2O)0.2(P2O5)0.5 bioresorbable glass and its structural characterisation, J. Mater. Chem. 17 (2007) 4777–4784. doi:10.1039/b709955j.

[21] D. Carta, J.C. Knowles, M.E. Smith, R.J. Newport, Synthesis and structural characterization of P2O5–CaO–Na2O sol–gel materials, J. Non. Cryst. Solids. 353 (2007) 1141–1149. doi:10.1016/j.jnoncrysol.2006.12.093.

[22] I. Abrahams, K. Franks, G.E. Hawkes, G. Philippou, J. Knowles, T. Nunes, 23Na , 27Al and 31P NMR and X-ray powder diffraction study of Na/Ca/Al phosphate glasses and ceramics, J. Mater. Chem. 7 (1997) 1573–1580. doi:10.1039/A608325K.

[23] Q.P. Pham, U. Sharma, A.G. Mikos, Electrospinning of Polymeric Nanofibers for Tissue Engineering Applications: A Review, Tissue Eng. 12 (2006) 1197–1211. doi:10.1089/ten.2006.12.1197.

[24] A.J. Salgado, O.P. Coutinho, R.L. Reis, Bone tissue engineering: State of the art and future trends, Macromol. Biosci. 4 (2004) 743–765. doi:10.1002/mabi.200400026.

[25] N. Sachot, E. Engel, O. Castaño, Hybrid Organic-Inorganic Scaffolding Biomaterials for Regenerative Therapies, Curr. Org. Chem. 18 (2014) 2299–2314. doi:10.2174/1385272819666140806200355.

[26] C.B.S.S. Danoux, D.C. Bassett, Z. Othman, A.I. Rodrigues, R.L. Reis, J.E. Barralet, C.A. Van Blitterswijk, P. Habibovic, Elucidating the individual effects of calcium and phosphate ions on hMSCs by using composite materials, Acta Biomater. 17 (2015) 1–15. doi:10.1016/j.actbio.2015.02.003.

[27] C. Loebel, E.M. Czekanska, J. Staudacher, G. Salzmann, R.G. Richards, M. Alini, M.J. Stoddart, The calcification potential of human MSCs can be enhanced by interleukin-1β in osteogenic medium, J Tissue Eng Regen Med 2017. 11 (2017) 564–571. doi:10.1002/term.1950.

[28] S. Ajami, M.J. Coathup, J. Khoury, G.W. Blunn, Augmenting the bioactivity of polyetheretherketone using a novel accelerated neutral atom beam technique, J Biomed Mater Res Part B. 105B (2017) 1438–1446. doi:10.1002/jbm.b.33681.

[29] J. Yang, C. Cao, W. Wang, X. Tong, D. Shi, F. Wu, Q. Zheng, C. Guo, Z. Pan, C. Gao, J. Wang, Proliferation and osteogenesis of immortalized bone marrow-derived mesenchymal stem cells in porous polylactic glycolic acid scaffolds under perfusion culture, J Biomed Mater Res Part A. 92 (2010) 817–829. doi:10.1002/jbm.a.32378.

[30] F. Langenbach, J. Handschel, Effects of dexamethasone, ascorbic acid and β-glycerophosphate on the osteogenic differentiation of stem cells in vitro, Stem Cell Res. Ther. 4 (2013) 117. doi:10.1186/scrt328.

[31] H. Wang, B. Pang, Y. Li, D. Zhu, T. Pang, Y. Liu, Dexamethasone has variable effects on mesenchymal stromal cells, Cytotherapy. 14 (2012) 423–430. doi:10.3109/14653249.2011.652735.

[32] Y. Xiao, V. Peperzak, L. van Rijn, J. Borst, J.D. de Bruijn, Dexamethasone treatment during the expansion phase maintains stemness of bone marrow mesenchymal stem cells, JJ Tissue Eng Regen Med. 4 (2010) 374–386. doi:10.1002/term.250.

[33] M. Stefanic, M. Peroglio, A.-M. Stanciuc, G.C. Machado, I. Campbell, M.M. Kržmanc, M. Alini, X. Zhang, The influence of strontium release rate from bioactive phosphate glasses on osteogenic differentiation of human mesenchymal stem cells, J. Eur. Ceram. Soc. 38 (2017) 887–897. doi:10.1016/j.jeurceramsoc.2017.08.005.

[34] H.J. Kim, U.J. Kim, G.G. Leisk, C. Bayan, I. Georgakoudi, D.L. Kaplan, Bone regeneration on macroporous aqueous-derived silk 3-D scaffolds, Macromol. Biosci. 7 (2007) 643–655. doi:10.1002/mabi.200700030.

[35] X. Xin, M. Hussain, J.J. Mao, Continuing differentiation of human mesenchymal stem cells and induced chondrogenic and osteogenic lineages in electrospun PLGA nanofiber scaffold, Biomaterials. 28 (2007) 316–325. doi:10.1016/j.biomaterials.2006.08.042.

[36] K.G. Jain, S. Mohanty, A.R. Ray, R. Malhotra, B. Airan, Culture & differentiation of mesenchymal stem cell into osteoblast on degradable biomedical composite scaffold: In vitro study, Indian J Med Res. 142 (2015) 747–758. doi:10.4103/0971-5916.174568.

[37] E. Della Bella, A. Parrilli, A. Bigi, S. Panzavolta, S. Amadori, G. Giavaresi, L. Martini, V. Borsari, M. Fini, Osteoinductivity of nanostructured hydroxyapatite-functionalized gelatin modulated by human and endogenous mesenchymal stromal cells, J Biomed Mater Res Part A. 106 (2018) 914–923. doi:10.1002/jbm.a.36295.

[38] D.G. Phinney, G. Kopen, W. Righter, S. Webster, N. Tremain, D.J. Prockop, Donor variation in the growth properties and osteogenic potential of human marrow stromal cells, J. Cell. Biochem. 75 (1999) 424–436. doi:10.1002/(SICI)1097-4644(19991201)75:3<424::AID-JCB8>3.0.CO;2-8.

[39] G. Friedl, R. Windhager, H. Schmidt, R. Aigner, The osteogenic response of undifferentiated human mesenchymal stem cells (hMSCs) to mechanical strain is inversely related to body mass index of the donor, Acta Orthop. 80 (2009) 491–498. doi:10.3109/17453670903171883.

[40] H.S. Cho, I.H. Song, S.-Y. Park, M.C. Sung, M.-W. Ahn, K.E. Song, Individual Variation in Growth Factor Concentrations in Platelet-rich Plasma and Its Influence on Human Mesenchymal Stem Cells, Korean J Lab Med. 31 (2011) 212–218. doi:10.3343/kjlm.2011.31.3.212.

[41] K.K. Chereddy, A. Lopes, S. Koussoroplis, V. Payen, C. Moia, H. Zhu, P. Sonveaux, P. Carmeliet, A. des Rieux, G. Vandermeulen, V. Préat, Combined effects of PLGA and vascular endothelial growth factor promote the healing of non-diabetic and diabetic wounds, Nanomedicine Nanotechnology, Biol. Med. 11 (2015) 1975–1984. doi:10.1016/j.nano.2015.07.006.

[42] O. Trabold, S. Wagner, C. Wicke, H. Scheuenstuhl, M.Z. Hussain, N. Rosen, A. Seremetiev, H.D. Becker, T.K. Hunt, Lactate and oxygen constitute a fundamental regulatory mechanism in wound healing, WOUND REP REG. 11 (2003) 504–509. doi:10.1046/j.1524-475X.2003.11621.x.

[43] C. Morland, K.A. Andersson, Ø.P. Haugen, A. Hadzic, L. Kleppa, A. Gille, J.E. Rinholm, V. Palibrk, E.H. Diget, L.H. Kennedy, T. Stølen, E. Hennestad, O. Moldestad, Y. Cai, M. Puchades, S. Offermanns, K. Vervaeke, M. Bjørås, U. Wisløff, J. Storm-Mathisen, L.H. Bergersen, Exercise induces cerebral VEGF and angiogenesis via the lactate receptor HCAR1, Nat. Commun. 8 (2017) 1–9. doi:10.1038/ncomms15557.

[44] Z. Álvarez, O. Castaño, A.A. Castells, M.A. Mateos-Timoneda, J.A. Planell, E. Engel, S. Alcántara, Neurogenesis and vascularization of the damaged brain using a lactate-releasing biomimetic scaffold, Biomaterials. 35 (2014) 4769–4781. doi:10.1016/j.biomaterials.2014.02.051.

[45] G. Pattappa, H.K. Heywood, J.D. de Bruijn, D.A. Lee, The metabolism of human mesenchymal stem cells during proliferation and differentiation, J. Cell. Physiol. 226 (2011) 2562–2570. doi:10.1002/jcp.22605.

[46] S.-H. Hsu, C.-T. Chen, Y.-H. Wei, Inhibitory Effects of Hypoxia on Metabolic Switch and Osteogenic Differentiation of Human Mesenchymal Stem Cells, Stem Cells. 31 (2013) 2779–2788. doi:10.1002/stem.1441.

[47] P. Prieto, M. Fernández-Velasco, M.E. Fernández-Santos, P.L. Sánchez, V. Terrón, P. Martín-Sanz, F. Fernández-Avilés, L. Boscá, Cell expansion-dependent inflammatory and metabolic profile of human bone marrow mesenchymal stem cells, Front. Physiol. 7 (2016) 1–12. doi:10.3389/fphys.2016.00548.

[48] N. Ilan, S. Mahooti, J.A. Madri, Distinct signal transduction pathways are utilized during the tube formation and survival phases of in vitro angiogenesis, J. Cell Sci. 111 (1998) 3621–3631.

[49] A. Scherzed, S. Hackenberg, K. Froelich, K. Rak, P. Schendzielorz, T. Gehrke, R. Hagen, N. Kleinsasser, The differentiation of hMSCs counteracts their migration capability and pro-angiogenic effects in vitro, Oncol. Rep. 35 (2016) 219–226.

doi:10.3892/or.2015.4383.

[50] M. Buitinga, K. Janeczek Portalska, D.-J. Cornelissen, J. Plass, M. Hanegraaf, F. Carlotti, E. de Koning, M. Engelse, C. van Blitterswijk, M. Karperien, A. van Apeldoorn, J. de Boer, Coculturing Human Islets with Proangiogenic Support Cells to Improve Islet Revascularization at the Subcutaneous Transplantation Site, Tissue Eng. Part A. 22 (2016) 375–385. doi:10.1089/ten.tea.2015.0317.

[51] E.J. Smith, C.A. Staton, Tubule formation assays, in: Angiogenes. Assays A Crit. Apprais. Curr. Tech., 2007: pp. 65–87. doi:10.1002/9780470029350.ch4.

[52] S.A. Lowndes, A.L. Harris, The role of copper in tumour angiogenesis, J. Mammary Gland Biol. Neoplasia. 10 (2005) 299–310. doi:10.1007/s10911-006-9003-7.

[53] P. Koolwijk, M.G.M. van Erck, W.J.A. de Vree, M.A. Vermeer, H.A. Weich, R. Hanemaaijer, V.W.M. van Hinsbergh, Cooperative effect of TNFalpha, bFGF, and VEGF on the formation of tubular structures of human microvascular endothelial cells in a fibrin matrix. Role of urokinase, J. Cell Biol. 132 (1996) 1177–1188. doi:10.1083/jcb.132.6.1177.

[54] T. Shimo, T. Nakanishi, T. Nishida, M. Asano, M. Kanyama, T. Kuboki, T. Tamatani, K. Tezuka, M. Takemura, T. Matsumura, M. Takigawa, Connective Tissue Growth Factor Induces the Proliferation, Migration, and Tube Formation of Vascular Endothelial Cells In Vitro, and Angiogenesis In Vivo, J. Biochem. 126 (1999) 137–145. doi:10.1093/oxfordjournals.jbchem.a022414.

[55] G. Eke, N. Mangir, N. Hasirci, S. MacNeil, V. Hasirci, Development of a UV crosslinked biodegradable hydrogel containing adipose derived stem cells to promote vascularization for skin wounds and tissue engineering, Biomaterials. 129 (2017) 188–198. doi:10.1016/j.biomaterials.2017.03.021.

[56] S.S. Edwards, G. Zavala, C.P. Prieto, M. Elliott, S. Martínez, J.T. Egaña, M.R. Bono, V. Palma, Functional analysis reveals angiogenic potential of human mesenchymal stem cells from Wharton's jelly in dermal regeneration, Angiogenesis. 17 (2014) 851–866. doi:10.1007/s10456-014-9432-7.

[57] S. Roura, C. Gálvez-Montón, A. Bayes-Genis, Fibrin, the preferred scaffold for cell transplantation after myocardial infarction? An old molecule with a new life, J Tissue Eng Regen Med. 11 (2017) 2304–2313. doi:10.1002/term.2129.

[58] I. Caron, F. Rossi, S. Papa, R. Aloe, M. Sculco, E. Mauri, A. Sacchetti, E. Erba, N. Panini, V. Parazzi, M. Barilani, G. Forloni, G. Perale, L. Lazzari, P. Veglianese, A new three dimensional biomimetic hydrogel to deliver factors secreted by human mesenchymal stem cells in spinal cord injury, Biomaterials. 75 (2016) 135–147. doi:10.1016/j.biomaterials.2015.10.024.

[59] P. Rosset, F. Deschaseaux, P. Layrolle, Cell therapy for bone repair, Orthop. Traumatol. Surg. Res. 100 (2014) S107–S112. doi:10.1016/j.otsr.2013.11.010.

Chapter 4. Evaluating Ca^{2+} releasing proangiogenic sol-gel nanoparticles for the healing of chronic skin wounds

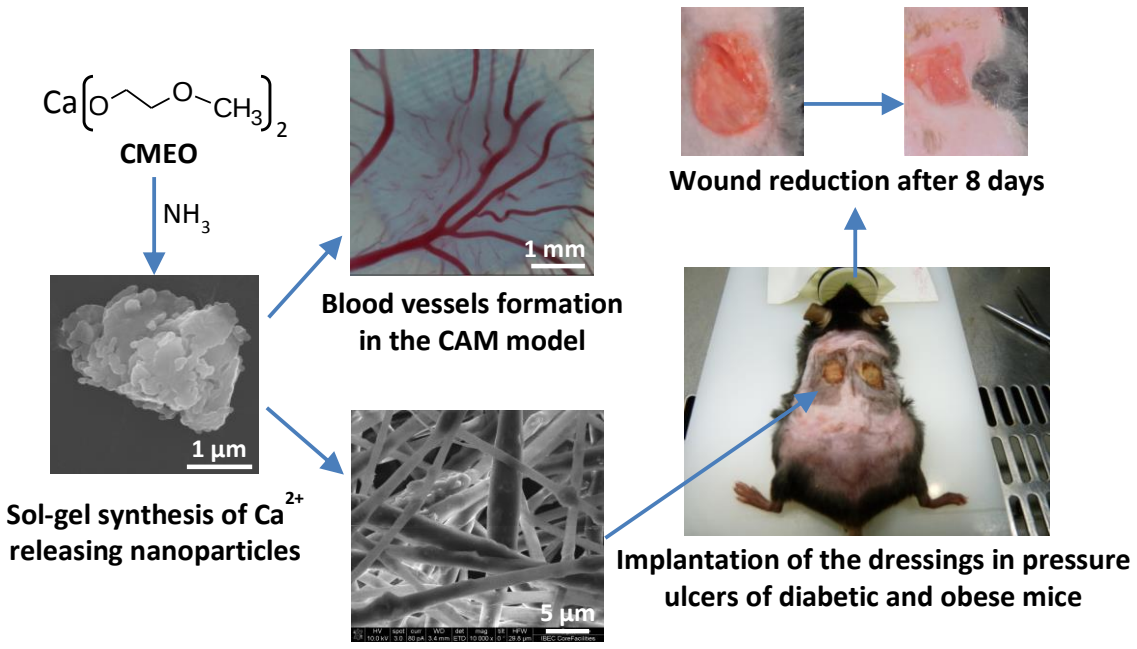

Scheme illustrating the content of the chapter

The development of efficient strategies to accelerate the healing of chronic skin wounds is still an important challenge. Although several disorders occur in its healing process, one of the most significant is an inefficient vascularization (ischemia). Nowadays, the use of growth factors (e.g. VEGF) is risky, expensive and difficult to store. Therefore, the development of cost-effective and safer strategies is necessary. Our group has demonstrated in previous studies that specific Ca^{2+} concentrations play a role in angiogenesis. We observed that the stimulation of extracellular Ca^{2+}-sensing receptors (CaSRs) regulates the synthesis of paracrine angiogenic factors. In this chapter, we used the P0 particles (here coded as Ca particles) synthesized in Chapter 2 to develop Ca^{2+} releasing platforms in form of dressings for wound healing applications. The presented method and product have been protected by means of patent (Ref. N. PCT/EP2018/064378). We synthesized the Ca^{2+} releasing nanoparticles by the sol-gel method and tuned their degradability by applying different thermal treatments. We combined the nanoparticles with electrospun polylactic acid (PLA) nanofibers to achieve easily removal dressings. Particles and scaffolds were characterized by several techniques. We demonstrated that the Ca^{2+} release of the particles could be controlled by applying different thermal treatments. The particles treated at 400 ºC (Ca400ºC) did not show cytotoxicity when cultured with human dermal fibroblasts (hDFs) and they increased the hDFs metabolic activity. We observed a significant improvement in the angiogenic response in the *ex-ovo* chick choriallantoic membrane (CAM) model. Finally, we showed that PLA-Ca400ºC electrospun dressings significantly accelerated the healing of generated skin pressure ulcers in diabetic and obese mice in comparison to conventional Mepilex® dressings, already used in the clinics to treat chronic skin wounds. These results highlight Ca^{2+} releasing dressings as an effective and feasible strategy for the treatment of chronic skin wounds. In addition, preliminary *in vivo* results of the dressings in a porcine skin model were very promising.

4.1. Introduction

The process of skin wound healing can be described as the biological recovery of injured "skin", which comprises the epidermis and dermis [1]. Skin wounds will naturally heal if there are not complications such as damage of the deep dermis [2], burns [3], infections [4] or alterations of the skin healing mechanisms due to disorders such as diabetes [5] or obesity [6]. In such cases, the recovery is much slower and painful, and the wounds often become chronic needing constant medical care. To date there are not efficient healing treatments for chronic skin wounds [2]. Although the origin of the wound can differ (e.g. a deep injure, diabetes, infection, etc.), the difficulty of healing often relies in an inefficient vascularization (i.e. ischemic wounds) [1]. Therefore, there is a necessity in developing effective treatments to improve the vascularization of ischemic wounds. In adults, vascularization occurs through different mechanisms being angiogenesis one of the main involved in the regeneration of damaged tissue. Angiogenesis consists on the sprouting of microvessels from preexisting capillaries of the surrounding healthy tissue [7,8]. The use of growth factors such as the VEGF or certain drugs [9] has demonstrated to induce angiogenesis. However, the strict regulations to translate these strategies to the clinics due to possible side effects on overdoses, and storage limitations, elevates their money-cost and limits their current success [5,7]. Among alternative strategies to overcome these drawbacks our group has been focused on the release of certain ions (e.g. Ca^{2+}) concentrations to stimulate angiogenesis [10]. It is known that modifications in the physiological Ca^{2+} level play a role in the chemotaxis and proliferation of specific cells such as MSCs or EPCs through the stimulation of extracellular Ca^{2+}-sensing receptors (CaSRs) [10,11]. What is not as well-understood, is that these CaSRs are also involved in the synthesis-regulation of angiogenic factors such as the VEGF [10]. Our group has proposed a mechanism which describes it [10], and has showed that Ca^{2+} releasing materials increased the formation of initial vasculature in different animal

models [12–14]. In such models, we used degradable calcium phosphate glasses synthesized by the sol-gel method to achieve optimal extracellular Ca^{2+} concentrations. However, the simultaneous release of PO_4^{3-} by these materials can also induce mineralization and the stimulation of ectopic bone formation, which would not be ideal for the treatment of chronic skin wounds [11,15]. To avoid such responses, we prescinded from the use of PO_4^{3-} and synthesized pure degradable Ca^{2+} releasing nanoparticles. We synthesized the particles by the alkaline precipitation of calcium 2-methoxyethoxide in an ethanolic medium and we tuned their degradability by applying different thermal treatments between 100 and 500 ºC. The presented method and product have been protected by means of patent registration under the title "CONTROLLABLE ION RELEASE CALCIUM PARTICLES, METHOD FOR PRODUCING SAME AND USE THEREOF" (Ref. N. PCT/EP2018/064378). Currently, commercial activities are being carried out to out-license the patent to a company interested on acquire the related intellectual property (IP) rights. Particle characterization includes X-ray diffraction (XRD), infrared spectroscopy (ATR-FTIR), elemental analysis (EA), energy dispersive X-ray spectroscopy (EDS), nuclear magnetic resonance (^{1}H NMR), scanning electron microscopy (FE-SEM), dynamic light scattering (DLS) and Z-potential. We evaluated the Ca^{2+} release of the particles treated at the different temperatures in buffered 4-(2-hydroxyethyl)-1-piperazineethanesulfonic acid (HEPES) medium (pH 7.4) at 37 ºC. We chose the treated particles at 400 ºC (Ca400ºC) for the biological evaluation. Such evaluation included cytotoxicity and viability of the particles with human dermal fibroblasts (hDFs) and quantification of the formation of new vasculature in the *ex-ovo* chick choriallantoic membrane (CAM) model. Finally, we electrospun such particles in polylactic acid (PLA) nanofibers to produce an easily removal dressing. The dressings were characterized by FE-SEM, tensile-strain tests and differential scanning calorimetry (DSC). We evaluated the wound healing capacity of the dressings by their implantation in generated skin pressure ulcers in diabetic and obese male mice and later in a preliminary porcine skin model still under development.

4.2. Materials and methods

If not otherwise specified all reagents were purchased from Sigma-Aldrich.

4.2.1. Precursor synthesis

1M calcium 2-methoxyethoxide in 2-methoxyethanol was synthesized as previously described [12,13]. Briefly, the right amount of metallic calcium granules PS (98%, Panreac) was oxidized in 2-methoxyethanol (99,8%) by refluxing it at the solvent boiling point under $Ar_{(g)}$ atmosphere for 24 h. The alkoxide solution was filtered with 0.45 µm PTFE hydrophobic Minisart® SRP25 syringe filters (Sartorius AG, Göttingen, Germany) and stored under $Ar_{(g)}$ atmosphere at -20 ºC.

4.2.2. Ca^{2+} releasing nanoparticles synthesis

10 mL of the 1M calcium 2-methoxyethoxide were dissolved in 90 mL of absolute ethanol PRS (99,5%, Panreac) at room temperature (RT). Ammonia PA-ACS (30%, Panreac) was added dropwise (~30 mL) until a suspension of particles appeared. The suspension was left overnight and then we applied two cycles of centrifuged/cleaning at 48384xg for 20 min with absolute ethanol PRS (99,5%, Panreac) and one last with hexane ACS (≥99%). Particles were dried at 70 °C for 2 h and ground in an agate mortar. We coded the particles as “Ca” due to their calcium content. The particles were thermal treated at 100, 200, 300, 400 or 500 °C in a muffle furnace L9/11 (Nabertherm, Lilienthal, Germany) for 12 h to study changes in their chemical structure and degradability. Particles were weight in a Sartorius CP224S analytical balance (Sartorius AG, Göttingen, Germany) before and after thermal treatments to know mass loss. All particles were stored in a desiccator under vacuum until characterization analysis.

4.2.3. Particle characterization

4.2.3.1. Energy dispersive X-ray spectroscopy (EDS) of the particles at room temperature (RT) and 400 °C was performed in a Quanta Q200 scanning electron microscopy (SEM) (FEI Company, Hillsboro, OR, USA) coupled with an EDS detector to quantify the approximate atomic composition. Measurement parameters include 20 KV of emission voltage and 10 mm of working distance. Particles were previously coated with a thin carbon layer to improve conductivity.

4.2.3.2. X-ray diffraction (XRD) of the particles at 25, 100, 300 and 500 °C was performed in a PANalytical X'Pert PRO MPD Alpha1 Powder diffractometer (PANalytical, Almelo, the Netherlands) to determine the crystalline phases. Approximately, 100 mg of the particles were pressed in a cylindrical standard sample holder of 16 mm of diameter and 2.5 mm of height. Samples were analyzed in a Bragg-Brentano $\theta/2\theta$ 240 mm radius geometry. We analyzed the data with the ©PANalytical X'Pert HighScore software (PANalytical, Almelo, the Netherlands) and the database PDF2 (2001) from the international center of diffraction data (ICDD).

4.2.3.3. Attenuated total reflectance infrared spectroscopy (ATR-FTIR) of the particles at 25 and 400 °C was performed in a Spectrum Two FT-IR Spectrometer (PerkinElmer, Waltham, MA, USA) and compare with standards of the database ©2005-2008, Fiveash Data Management, Inc. Approximately 5 mg of the particles were pressed in a UATR Diamond/ZnSe accessory (1 reflection). A background without particles was performed before each measurement. We used the ©PerkinElmer Spectrum (PerkinElmer, Waltham, MA, USA) software to analyze the spectra.

4.2.3.4. ^{1}H nuclear magnetic resonance (^{1}H NMR) of the dissolved particles at 25 and 400 °C in D_2O (99.9%) plus 1.5% (v/v) HCl (37%, Panreac) was performed in a Bruker 400 MHz Avance III spectrometer (Bruker, Billerica, MA, USA) equiped with a Prodigy TCl 5 mm cryoprobe to determine the presence of organics. The spectra were registered between 16 and -3.8 ppm, applying 3.66 µs, 30° pulse, a delay of 1 s between pulses, and an acquisition time of 2.5 s. 32 scans were collected to have a good signal-to-noise ratio. Spectra were referenced to the ^{1}H of the deuterium solvent. Data was analyzed using the ACD/Spectrus Processor software [16].

4.2.3.5. Elemental analysis (EA) of the particles at the different temperatures was performed by combustion in an elemental analyzer EA CE 1108 (Thermo Fischer Scientific, Waltham, MA, USA) to determine the C mass percentage. Approximately, 2000 µg of the particles were weight in a MX5 microbalance (Mettler-Toledo, Greifensee, Switzerland). The samples were analyzed by combustion at 1060 ºC using atropine as a standard. A mixture of vanadium pentoxide and lead powder was added to facilitate the combustion. To determine the organic C content, samples were previously treated with 6N HCl in Ag capsules to eliminate carbonates.

4.2.3.6. Field emission electron microscopy (FE-SEM) images of the particles at 25 and 400 °C were performed in a Nova Nano SEM-230 ultra-high resolution field emission scanning electron microscopy (FEI Company, Hillsboro, OR, USA). Approximately 1 mg of the particles was dispersed in 1 mL of absolute ethanol (99.5%, Panreac) with an Ultrasonic Processor UP50H (Hielscher Ultrasonics, Teltow, Germany). 2 µL of the dispersion were added on silicon substrates and left to dry at RT. Samples were irradiated at 5 KV at a working distance of 5 mm. Particles were coated with a thin carbon layer to improve conductivity.

4.2.3.7. Dynamic light scattering (DLS) and Z potential of the particles at 400 °C were performed in a Zetasizer Nano ZS (Malvern, Worcestershire, UK) to determine particle size and surface charge. The particles were dispersed in absolute ethanol (99.5%, Panreac), using an Ultrasonic Processor UP50H (Hielscher Ultrasonics, Teltow, Germany). Measurements were done in a 10x2 mm precision Quartz Suprasil® cell 115F-QS (Hellma®Analytics, Müllheim, Germany) or a disposable capillary cell (DTS1070) (Malvern Instruments, Worcestershire, UK) for the Z-potential respectively. Results were treated with the Zetasizer 7.12 (07/12/2016) (Malvern, Worcestershire, UK) software for Windows 7. Size population was expressed in percentage of number of particles.

4.2.3.8. Inductively coupled plasma mass spectroscopy (ICP-MS) analysis was performed in an Optima 3200 ICP-OES Spectrometer (PerkinElmer, Waltham, MA, USA) to determine the Ca^{2+} release of the particles in aqueous solution. 1 mg of the particles at each temperature (25, 100, 200, 300, 400 and 500 °C) was dispersed in 10 mL of 0.05 M 4-(2-hydroxyethyl)piperazine-1-ethanesulfonic acid (HEPES) solution at pH 7.4 in 15 mL centrifuged tubes. Tubes were kept at 37 °C with gentle agitation. After 1, 5, 25, 45, 69, 94 and 120 h tubes were centrifuged, and 9 mL of the solutions were extracted. The tubes were refilled with 9 mL of the HEPES solution and the particles were smoothly resuspended using a vortex orbital. Tubes were placed again at 37 °C. 1 mL of each extraction was diluted in 9 mL of a 1% (v/v) HNO_3 (60%, Panreac) aqueous solution and stored at 4 °C for the ICP-MS analysis. The pH of the extractions was measured before dilution in a Crison pH-Meter GLP 22+ coupled with a Crison 50 28 pH electrode (Hach Company, Loveland, CO, USA).

4.2.4. Biological evaluation

Dr. Soledad Perez-Amodio (Senior researcher) and Dr. Claudia Navarro-Requena (former PhD candidate) currently working in the same research project, supported me with the design and interpretation of the biological evaluation due to their high expertise in the biological field. My support in these assays consisted of the supply and characterization of the different materials, the support in some of the assays and the discussion of the results in this chapter.

4.2.4.1. Human dermal fibroblast (hDFs) viability

We assessed the viability of hDFs with extractions of cell culture media (ECM) in contact with the Ca400ºC particles for 24 h. Viability was assessed using alamarBlue ™ (Thermo Scientific) reagent, following the manufacturer's instructions. ECM were obtained by incubating 3 mg of the Ca400°C particles in 1.5 mL tubes with 1 mL of culture media consisting on DMEM no calcium (Gibco) supplemented with 10 % of sterile-filtered fetal bovine serum non-USA origin (FBS), 1% of L-glutamine (200 mM, Invitrogen™) and 1% of penicillin-streptomycin (10^4 U/mL, Invitrogen™) at 37 ºC for 1 day. Tubes were then centrifuged and the Ca^{2+} concentration of the ECM was measured by absorbance following a colorimetric method based on the O-Cresolphthalein complexone (Chapter 2, section 2.2.11.) [17,18]. hDFs from healthy donors (Promocell) at passage 5 were seeded on 24-well plates Nunclon™ Delta (ThermoFischer Scientific) at a density of 15000/well with 380 µL of ECM previously sterilized by filtration. After 1 day of culture the ECM was replaced with complete DMEM supplemented with 10% of alamarBlue®. The fluorescence intensity of the metabolized alamarBlue® was measured after 3 h at 560/590 nm in an Infinite M200 Pro Microplate Reader (Tecan Group Ltd., Männedorf, Zürich, Switzerland). In addition, we performed a live/dead cell imaging assay to qualitatively evaluate cell viability. A live/dead solution was prepared with 4µM of calcein

AM (≥96%) and 2μM of ethidium bromide in phosphate buffered saline (Gibco®) solution (PBS). Prior to the addition of the live/dead stain, cells were washed with PBS to remove any remaining culture media and FBS. Cells were incubated with the live/dead solution in dark conditions for 20 minutes prior to imaging. Images were obtained with an Eclipse E200 fluorescence microscope (Nikon, Shinagawa, Tokyo, Japan) fitted with a digital camera.

4.2.4.2. *Ex-ovo* choriallantoic membrane (CAM) angiogenic model

We assessed the angiogenic capacity of the Ca400ºC particles using an *ex-ovo* CAM model adapted from [19]. Briefly, fertilized chick eggs (Granja Gibert S.A., Cambrils, Spain) were incubated at 37.5 ºC in an SI 24 eggs incubator (Lincu Avitec S.L., Valencia, Spain) with air ventilation and a high humid atmosphere. After 3 days the eggs were cracked, and the full embryos were placed in Falcon™ standard tissue culture dishes 100x20 mm (Corning Inc.) surrounded with sterile PBS solution to maintain a high moisture level. After 6 more days of incubation, the Ca400ºC particles were dispersed using an Ultrasonic Processor UP50H (Hielscher Ultrasonics, Teltow, Germany) in a 2 mg/mL Opticol™ Rat Type I Collagen (3.8 mg/mL, Cell Guidance Systems) aqueous solution at a concentration of 0.5 and 1 % (w/w) of particles respectively. 30 μL of the dispersion were added on 6 mm nylon net filters discs (Merck Millipore Ltd.). We also included a negative and a positive control of 2mg/mL Opticol™ solution with or without 200 ng of Recombinant Human VEGF 121 (PeproTech®) respectively. We implanted 32 replicates per condition in 8 different embryos. The implants were sterilized with UV and placed near to the big blood vessels. After 3 days of implantation the embryos were sacrificed by decapitation and the discs and the surrounding CAM were fixed with Formalin solution neutral buffered (10%). After 25 min, the fixed discs were cut and photographed in a MVX10 Macro Zoom Microscope (Olympus Corporation, Tokyo,

Japan). The small blood vessels on each scaffold were quantified by using an improved version of the ImageJ macro used in Chapter 3, section 3.2.6. (Figure 9).

4.2.4.3. *In vivo* wound healing

We assessed the wound healing capacity of the Ca400ºC particles by incorporating them in polylactic acid (PLA) nanofiber dressings and implanting them in generated skin ulcers in diabetic and obese mice.

4.2.4.3.1. Pressure ulcer animal model

Eight obese and diabetic mice (8 weeks old) with a db/db mutation in the leptin receptor, were ordered from Charles River Laboratories (Wilmington, Massachusetts, USA). Upon arrival mice were acclimated in a pathogen-free environment for one week and fed with a LabDiet® 5K52 formulation (6% fat) and *ad libitum* water. Only male mice were used to avoid hormonal interference in wound healing due to different animal gender [20–22]. Pressure ulcers were performed, as previously reported [23–25], by applying ischemic-reperfusion cycles using two magnets. Briefly, mice were anesthetized with 5% gas isoflurane and maintained slept with a remaining 2% at day 1. The mice backs were gently shaved and cleaned with 70% ethanol aqueous solution. The back skin was pinched and gently placed between two round ceramic magnets (12x5 mm) for 12 h. Mice were monitored until they showed a complete normal awakened state. Six cycles of 12 h of magnet-skin-pressure followed by 12 h of rest were performed to generate pressure ulcers covered by necrotic tissue. A space of 1 cm of skin exceeded the two magnets to obtain two symmetric ulcers per mice separated by healthy tissue. Magnets were sterilized with 70% ethanol solution and UV. Mice were not anesthetized for magnet replacement and they were treated separately to avoid magnet sticking. During the six

magnets-cycles, mice did not show signs of pain. Wounds were treated separately with the Ca400°C particles embedded in PLA nanofiber dressings or with conventional Mepilex® (Mölnlycke Health Care) already used in the clinics to treat chronic skin wounds [26,27], as positive control. During all the experiment we followed the approval of the animal care committee of the Catalan government.

4.2.4.3.2. Dressing fabrication

We electrospun the Ca400°C particles with polylactic acid (PLA) nanofibers (PLA-Ca400ºC) to have a wound dressing that could be easily replaced every day. To do so we weighed the right amount of Ca400°C particles to have a mass percentage of 40%. The used electrospinning parameters were adapted from previous studies [12,13]. We added 15 mL of 2,2,2-trifluoroethanol (TFE) (99,8%, Panreac) and dispersed the particles using a Branson Digital Sonifier S-450 (Branson Ultrasonics, Danbury, CT, USA). Then we added the right amount of PLA Purasorb PLDL 7038 (Corbion) under agitation to have a mass percentage of 4% regarding the TFE solution. Once the PLA was dissolved (~4 h) the solution was placed in a 15 mL PP/PE syringe and electrospun at ~10 KV and ~12 cm distance tip-to-collector. Fibers were collected on parchment paper placed in a grounded cylindrical collector that spun at 120 rpm to homogenize the fiber-mat thickness along the rotatory direction while maintaining a random fiber distribution.

4.2.4.3.3. Mechanical properties of the dressings

Tensile-strain tests were applied at room temperature using a Zwick-Roell Z0.5TN testing machine (Zwick Roell Group, Ulm, Germany) to characterize the mechanical properties of the dressings. Four samples per each scaffold were cut into ISO 257-1/2 standardized test specimens of 50x5 mm, using a stainless-steel punch and a surgical

blade. The tensile-strain was calculated on the nominal cross-section area of the specimens. We used a caliper and a digital micrometer to measure the exact width and thickness of the samples. The average thickness ranged from 50 to 90 µm. The Young's modulus was considered as the slope of the linear region of the tensile-strain curve. The ultimate strength was considered as the maximum tensile stress supported by the material. The strain to failure was fixed to the previous point before a 40% of loss of the tensile strength. The tensile-strain test was monitored at a speed of 10 $mm \cdot min^{-1}$ using a force cell of 10 N. We used the testXpert II testing software (Zwick Roell Group, Ulm, Germany) to process the data.

4.2.4.3.4. Differential scanning calorimetry (DSC)

We used a DSC Q20 (TA instruments, New Castle, DE, USA) coupled with a nitrogen chiller to determine the thermal properties of the PLA in the scaffolds. Random ~9.4 mg pieces of each scaffold were placed in aluminum hermetic pans and were submitted to two heating cycles from -90 to 200 ºC at 10 $ºC \cdot min^{-1}$ with a nitrogen cooling between cycles. We determined the crystallization and melting properties of the PLA from the curve of the first cycle. From the curve of the second cycle, we assessed the glass transition temperature (Tg) applying the inflexion point method. We used the Universal Analysis software v4.7A (TA instruments, New Castle, DE, USA) to process de data.

4.2.4.3.5. Dressing implantation

Squares of 1.7x1.7 cm of the PLA-Ca400°C and Mepilex® were used for the implantation. Prior to the implantation mice were anesthetized and the necrotic tissue from the wounds was mechanically removed using surgical scissors. The 1.7x1.7 cm square dressings were sterilized by UV, wet with a 0.9%(w/v) NaCl solution and carefully

placed on the wounds. Dressings were covered with adhesive Plaster (Coverplast® Latex-free, BSNmedical) and secured with an elastic gauze (Genové Dermatologics). Dressings were changed every 24 h placing the animals under anesthesia. After 8 days, all mice were sacrificed by cervical dislocation under anesthesia. The wounds were excised leaving 2 mm of margin, cut in half and fixed with 10% neutral buffered formalin solution for 24 h for histological analysis.

4.2.4.3.6. Wound imaging

At day 0 and before every dressing replacement, wounds were photographed with a Mavica FD91 digital camera (Sony, Minato, Tokyo, Japan) and the ORCA-2BT Imaging System (Hamamatsu Photonics, Shizuoka, Japan) provided with a C4742-98-LWG-MOD camera fitted with 512x512-pixel charge-couple device (CCD) cooled at -80 °C. The wound area from the images was quantified using the Wasabi image analysis software (Hamamatsu Photonics, Shizuoka, Japan) and normalized by the wound area at day 0.

4.2.4.3.7. CD31 immunohistochemistry

Histological changes of the fixed wounds at day 8 were evaluated in the full dermis and hypodermis. In each sample four regions of interest –ROI- (non-lesioned dermis, lesioned dermis, non-lesioned hypodermis, and lesioned hypodermis) were manually selected in each tissue section. Formalin-fixed wounded skin tissues were embedded in paraffin, cut at 4-5 μm and stained with anti-CD31 antibody (ab28364) or the corresponding isotype (ab27478) for the negative control. CD31 antibody was used as a marker of endothelial cells to quantify the area of blood vessels. Vessels were defined

as CD31 positive labeling. Samples stained with the isotype control tested negative (data not shown). Full images of CD31 immunostained sections were acquired by a NanoZoomer-2.0 HT C9600 scanner (Hamamatsu Photonics, Hamamatsu, Japan) at 20X magnification, in which 1 pixel corresponds to 0.46um. QuPAth software [28] was used to perform image analysis.

4.2.5. Preliminary porcine model

One female pig (Sus scorfa large white) of 32.4 kg was selected and submitted to one-week of acclimation period. Preoperatively, the animal was sedated with intramuscularly azaperone (4 mg/kg) + ketamine (10 mg/kg) and trachea-intubated. Anesthesia and analgesia were induced and maintained with propofol (4 mg/kg), isoflurane (1.5-2%, oxygen), and buprenorphine (0.01 mg/kg), respectively. Pre-surgical antibiotic therapy was performed with intravenous cephalothin (22 mg/kg). Four skin lesions (2x5 cm^2) were surgically generated in the dorsal area of the pig. The PLA-Ca400ºC dressings were applied in two lesions (treatment) and the other two were left as a control. The dressings were replaced at days 4, 8, 12, 18 and 22. The size of the different lesions was macroscopically measured by imaging and normalized by the area at day 0. The experiment was performed in the Pharmacology, Therapeutics and Toxicology department at the Universitat Autonòma de Barcelona (UAB)**.** We obtained the approval of the UAB Ethical Committee prior to start the experiment. The animal did not show any symptom of disability or morbidity during the experiment.

4.2.6. Statistical analysis

Statistical analysis was performed using GraphPad Prism 6 software. We used a two-tailed t-test to evaluate statistical differences in section 4.2.4.1. The F-test did not show statistical differences between variances. We used a one-way ANOVA Tukey's multiple comparison test for section 4.2.4.2. and 4.2.4.3.5., and a two-way ANOVA Tukey's multiple comparison test for section 4.2.4.3.4.. Values in sections 4.2.4.2., 4.2.4.3.4. and 4.2.4.3.5. passed the D'Agostino-Pearson omnibus normality test, suggesting a Gaussian distribution for the values. There were not enough replicates to perform the D'Agostino-Pearson omnibus normality test in section 4.2.4.1.. Columns in the graphs represent means and error bars show the standard error of the mean (SEM). Statistical differences include P_{value}<0.05 (*), <0.01 (**), <0.001 (***) and <0.0001 (****).

4.3. Results and discussion

4.3.1. Particles characterization

As we characterized in Chapter 2, section 2.3.5.1. Ca25ºC particles (labeled as P0-RT in Chapter 2) contained the presence of portlandite as a main crystalline phase (Figure 1A). The X-ray diffraction (XRD) spectrum showed the simultaneous presence of sharp and broad diffraction peaks suggesting an anisotropic nanometric crystal size for the portlandite [29,30]. Most of these diffraction peaks were highly broad indicating a very small nanometric size. However, the sharp peaks referred to bigger diffraction planes showing anisotropic crystal dimensions. We attributed the two unidentified XRD peaks (marked with a star) to the possible diffraction of some calcium 2-methoxyethoxide (CMEO) crystalline planes, although they could also derive from effects on the nanometric crystalline size of the portlandite.

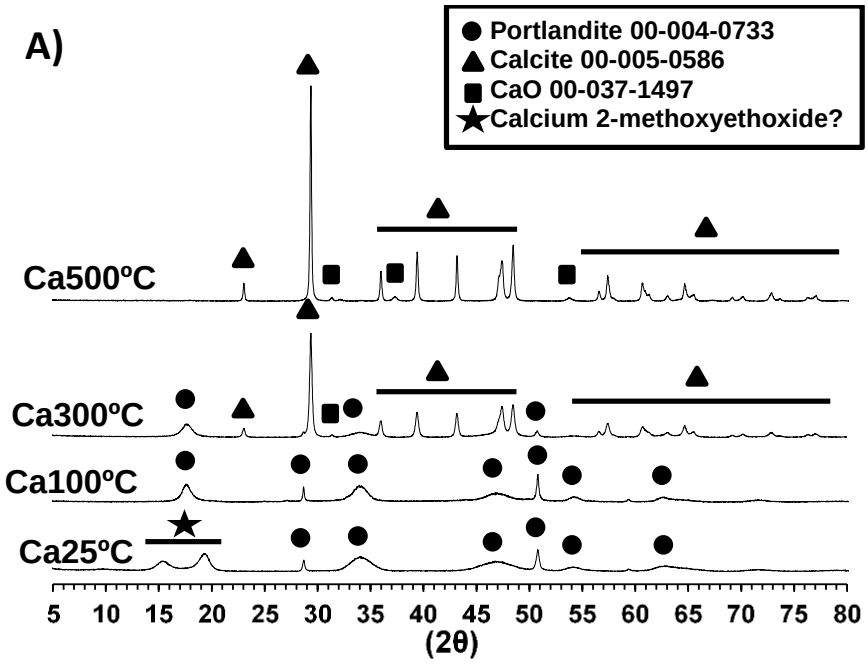

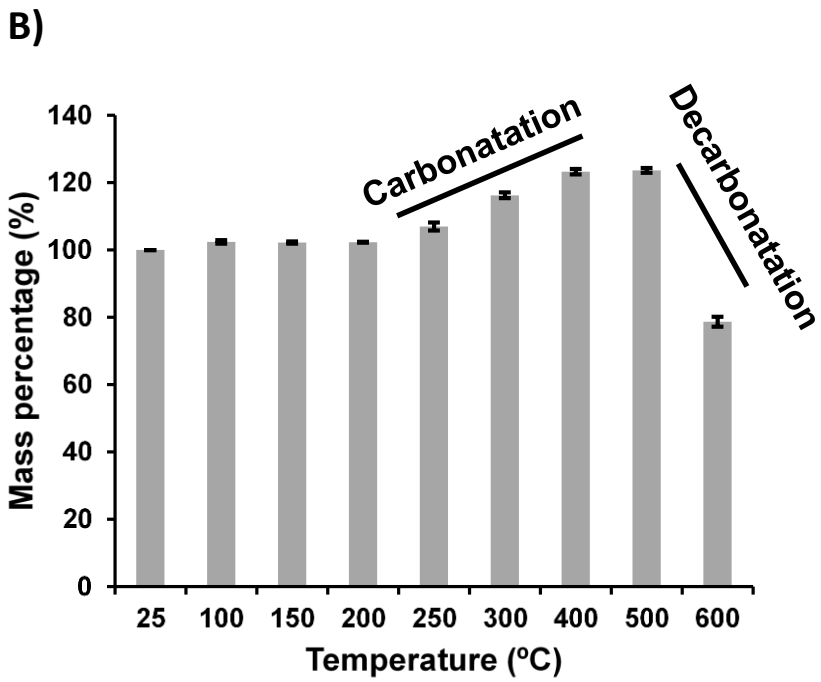

Figure 1. X-ray diffraction spectra **A)** and thermogravimetric analysis **B)** of the particles treated at different temperatures.

After the thermal treatment at 100ºC (Ca100ºC), we observed the elimination of such peaks, suggesting the degradation of the CMEO. We observed that most of the portlandite ($Ca(OH)_2$) was carbonated to calcite ($CaCO_3$) at 300ºC. However, there were still traces of portlandite that were not totally carbonated until 500 ºC. We started to observe a tiny decarbonation of the calcite to CaO at 500 ºC. The thermogravimetric results (Figure 1B) supported this information revealing an increased weight from 250 ºC to 400 ºC due to the carbonatation of the $Ca(OH)_2$. Then we observed a significant decrease at 600ºC indicating the decarbonation of the $CaCO_3$ to CaO.

The ^1H NMR spectra of the dissolved Ca25ºC particles in acidic D_2O (Figure 2A) showed the presence of CMEO and EtOH, suggesting that the unidentified peaks form the XRD spectra (Figure 1A) could represent some crystalline diffraction planes of the CMEO. We observed the elimination of such organics after the thermal treatment at 400ºC (Figure 2A). The elemental analysis (EA) showed that the total amount of organic carbon (TOC) for the Ca25ºC particles was only a ~0.51% of the total weight, indicating a small amount

of CMEO (~1.5%) (Figure 2B). We observed a gradual reduction of the TOC with the temperature indicating the decomposition of the CMEO. However, there was a tiny amount of TOC (~0.2-0.1 %) from 300ºC to 500ºC, which we attributed to the calcination of the CMEO to graphite at such temperatures. This was consistent with the ^{1}H NMR results (Figure 2A) that did not show the presence of any organic at 400ºC. In the elemental analysis (Figure 2B), we also identified the presence of the carbon form the carbonated portlandite ($CaCO_3$) that was included in the total carbon content (TCC). We observed an increase of the TCC with the temperature being consistent with an increase in carbonatation. Notice that the ~12% of TCC (considering almost no TOC) for the Ca500ºC particles means a composition of ~100% of $CaCO_3$. On the other hand, the presence of ~3% of TCC and ~0.5% of TOC for the Ca25ºC particles indicates the presences of ~20% of $CaCO_3$. We attributed this significant amount of $CaCO_3$ at 25ºC to a considerable $CO_{2(g)}$ absorption during particle synthesis or grinding. The absence of calcite in the XRD spectrum (Figure 1A) for the Ca25ºC particles indicates an amorphous structure for this $CaCO_3$.

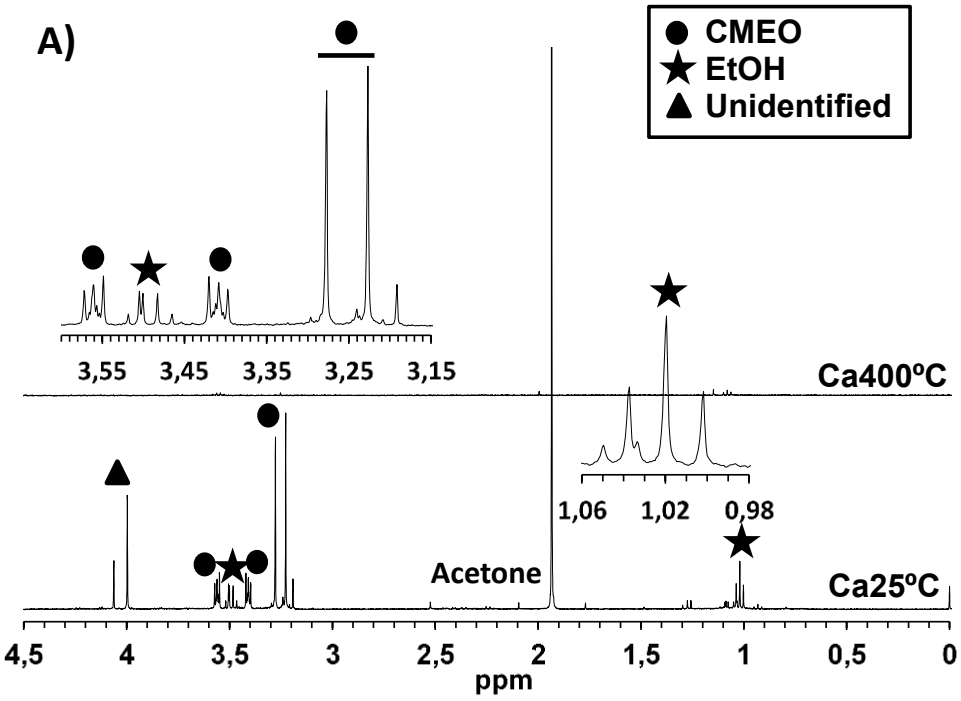

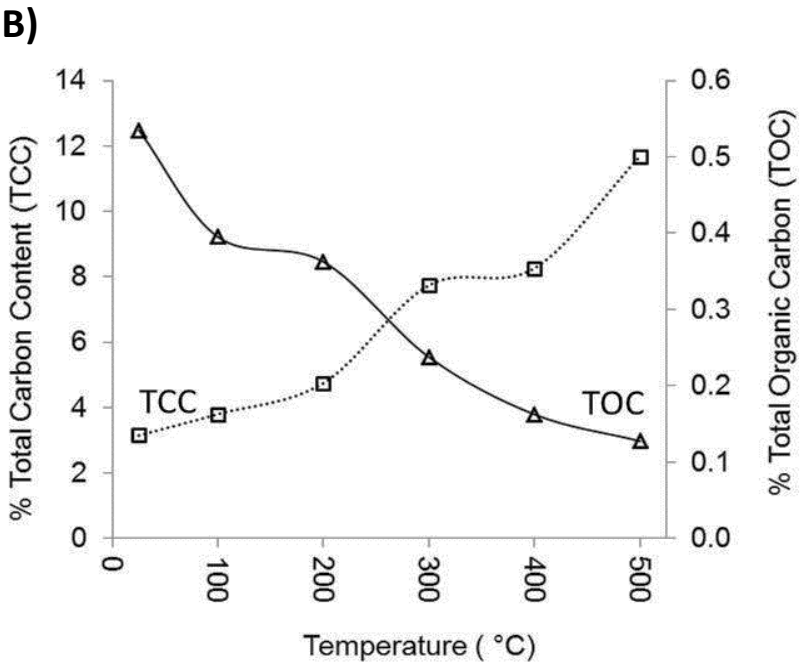

Figure 2. ^{1}H NMR spectra of the Ca25ºC and Ca400ºC particles dissolved in acidic D_2O **A)**. Total carbon content (TCC) and total organic carbon (TOC) of the particles treated at the different temperatures **B)**. Notice that the identified acetone in **A)** is attributed to impurities in NMR tube cleaning.

In fact, the ATR-FTIR spectrum of the Ca25ºC particles (Figure 3A) showed the presence of C-O frequency bands, confirming the existence of $CaCO_3$ at 25ºC [31,32]. It also revealed Ca-O and O-H bands from the presence of portlandite and some absorbed moisture, respectively. We identified an increase in the $CaCO_3$ frequency bands intensity at 400ºC indicating a higher amount of $CaCO_3$. The sharper C-O bands at 400 ºC also indicate a more well-ordered structure due to crystallization. We did not identify other compounds apart from $Ca(OH)_2$ and $CaCO_3$ in the ATR-FTIR spectra, being consistent with the EDS analysis of the Ca25ºC and Ca400ºC particles (Figure 3B) that only showed the presence of Ca, O and C. Notice that the C detected in the EDS analysis also involves the previous graphite coating to improve conductivity (section 4.2.3.1.).

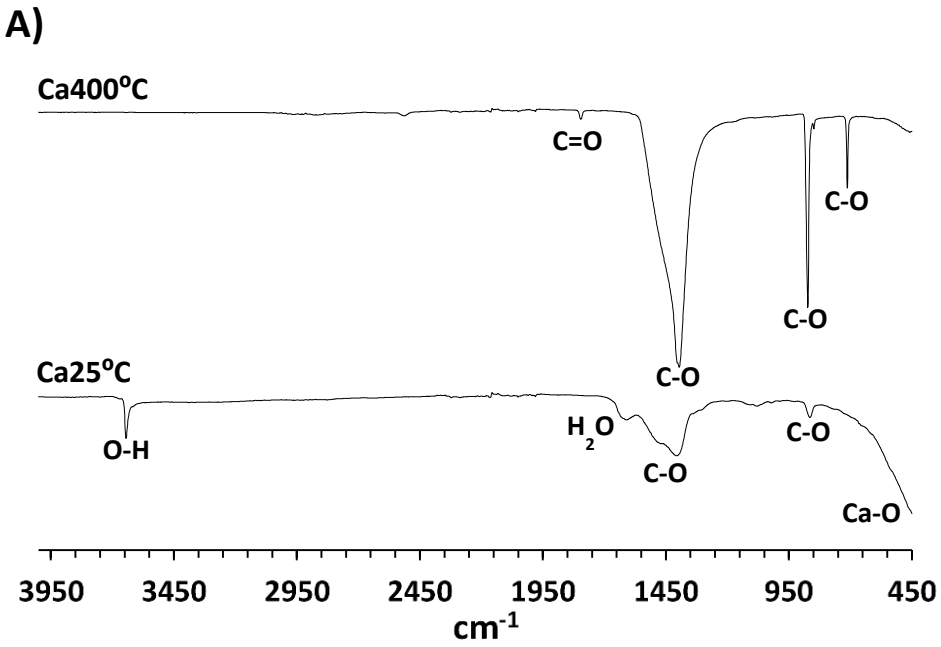

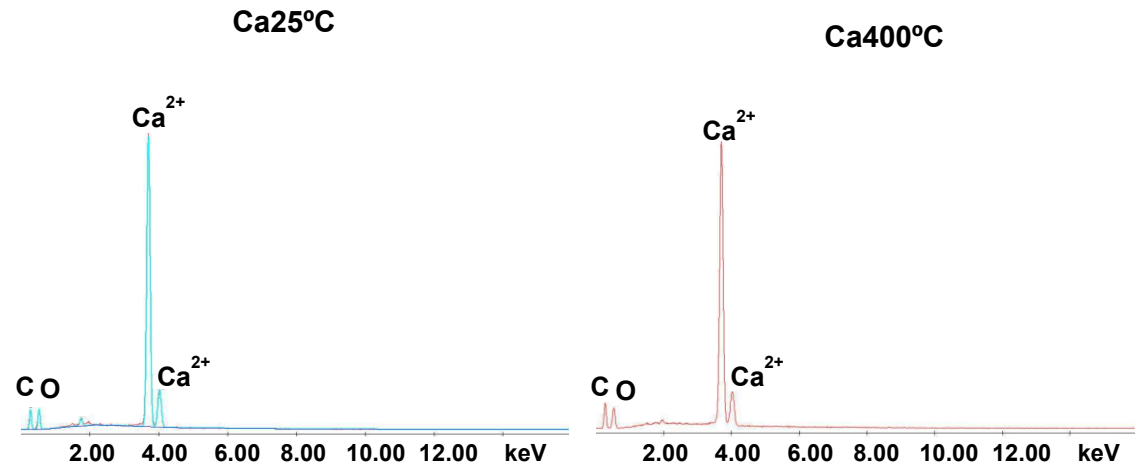

Figure 3. ATR-FTIR **A)** and EDS **B)** spectra of the Ca25ºC and Ca400ºC particles.

FE-SEM images showed a particle size slightly >1µm for Ca25ºC and Ca400ºC particles (Figure 4). However, the DLS measurements (Figure 5A) of a dispersion of the Ca400ºC particles in ethanol showed a smaller size average (324.1±103.9 nm), suggesting an aggregation of smaller particles at dried conditions. In fact, we can identify the presence

of smaller particles in the aggregates observed in FE-SEM images (Figure 4). The Z-potential (30.6±10.3 mV) of an ethanolic suspension of the Ca400ºC particles (Figure 5B) was in the limit range of colloidal stability (~30 mV), suggesting a propensity of the particles to form aggregates [33,34] due to the absence of electrostatic repulsion. We would like to add that this positive surface charge may enhanced the interaction of the particles with aliphatic polyesters with negative Z-potentials such as PLA [35,36], resulting in the formation of composites with better wettability and improved mechanical resistance.

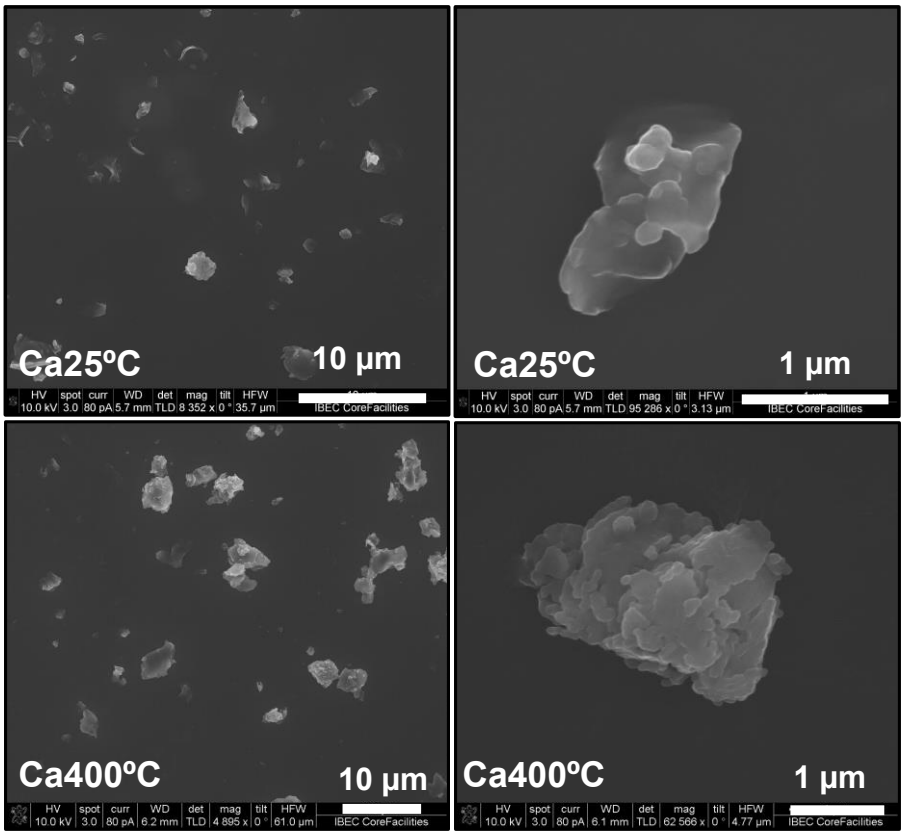

Figure 4. FE-SEM images of the Ca25ºC and Ca400ºC particles.

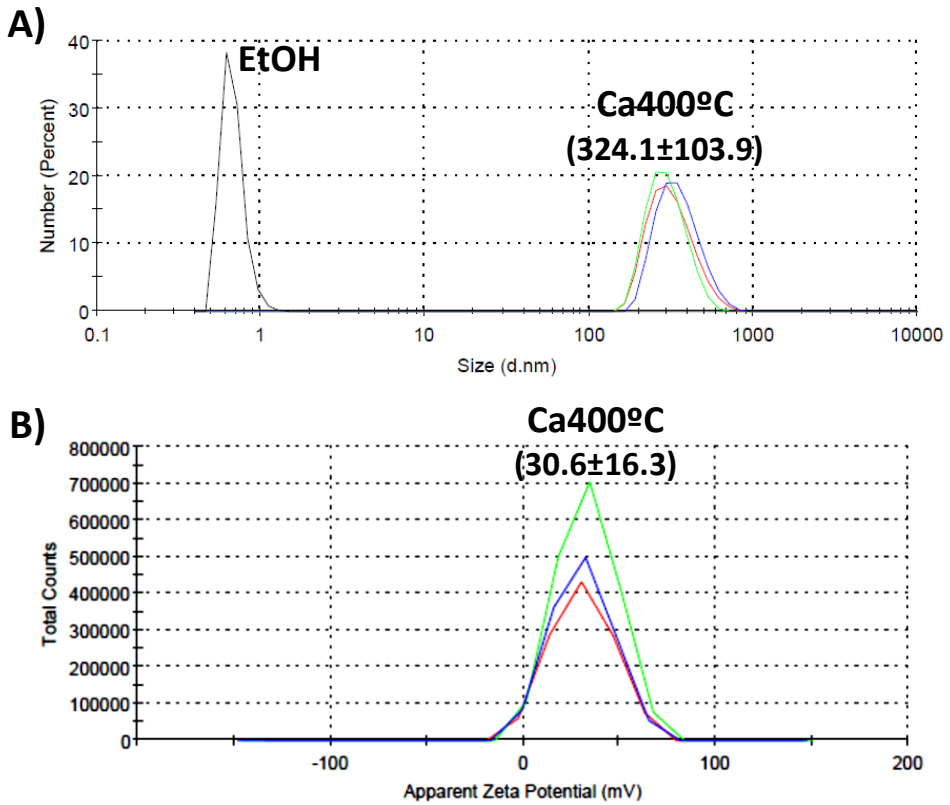

Figure 5. DLS **A)** and Z-potential **B)** measurements of the Ca400ºC particles. The different colors refer to three different measurements.

Summarizing this particle characterization section, we identified the Ca25ºC particles as a mixture of nanocrystalline portlandite with a ~20% of amorphous $CaCO_3$ and a possible ~1.5% of CMEO. All this calcium phases were carbonated to calcite at 300ºC. However, there were still traces of portlandite until 500 ºC. The calcite started to decarbonate to CaO between 500 and 600 ºC. The particle size was of several hundreds of nm, however, their low positive surface charge (~30 mV) induced the formation of bigger aggregates of sizes slightly >1µm.

4.3.2. Bioactive degradation of the particles

We measured the Ca^{2+} release and pH modification of the different thermally treated particles, after their immersion in HEPES solution (pH 7.4) at 37 ºC for 5 days (Figure 6). The particles treated below 300 ºC released high initial Ca^{2+} amounts due to the dissolution of the portlandite. We assigned the sustained slope observed afterwards to the more stable amorphous $CaCO_3$, also present in the particles. The decrease in the high initial Ca^{2+} burst between the Ca100ºC and the Ca200ºC particles is related to a slightly higher carbonatation at 200 ºC. We attributed the lower Ca^{2+} burst for the Ca25ºC particles to a purity reduction due to the presence of absorbed moisture at 25 ºC, which we detected in the ATR-FTIR spectrum (Figure 3A).

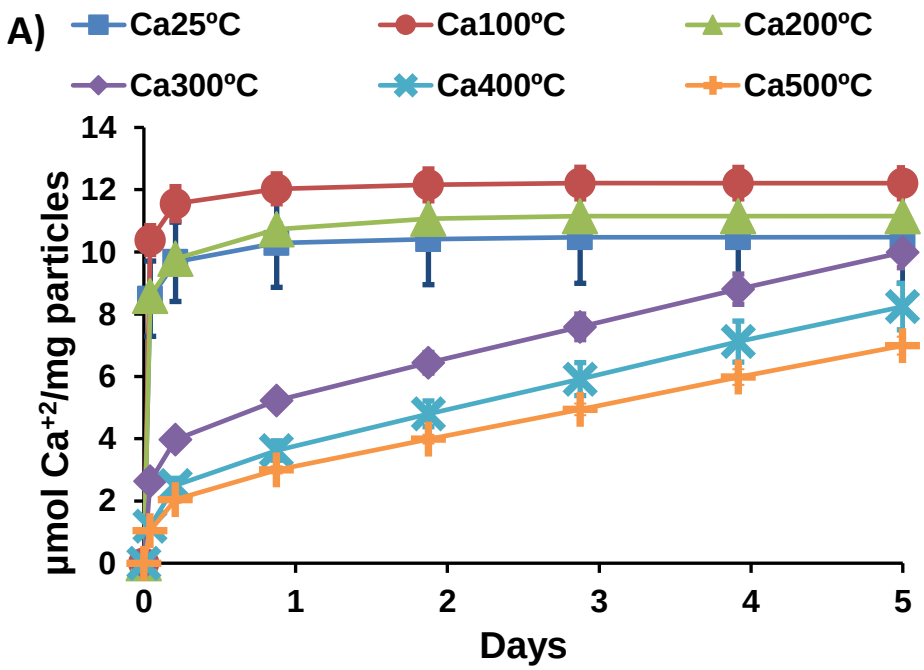

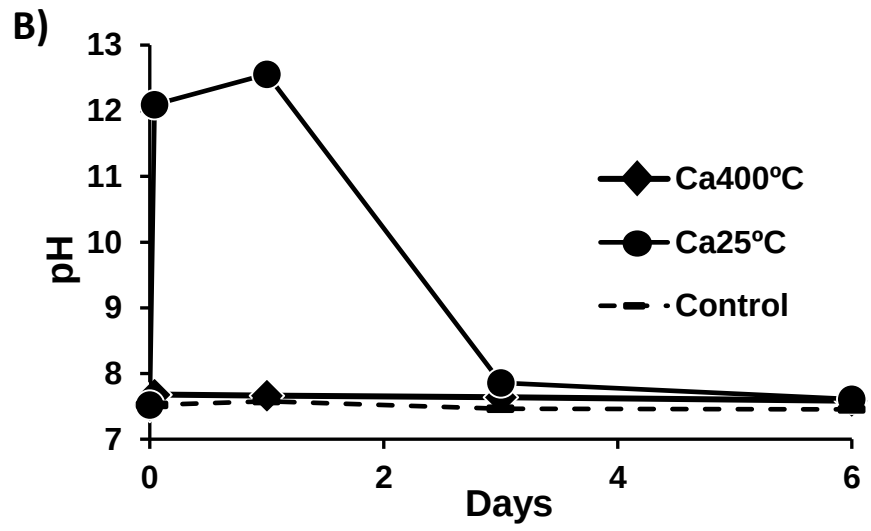

Figure 6. Ca^{2+} release **A)** and pH modification **B)** of the particles treated at the different temperatures, after their immersion in HEPES media at pH=7.4 and 37 ºC.

The Ca^{2+} release was significantly more sustained from 300 to 500 ºC due to most of the portlandite was carbonated to a more stable calcite. We assigned the low initial Ca^{2+} burst of the particles treated at or above 300 ºC to the presence of a small amount of portlandite and/or CaO. The slightly decrease in the $CaCO_3$ dissolution slope from 300 to 500 ºC suggests an increase in calcite crystallinity with the temperature. The pH was very basic for the particles treated below 300 ºC due to the dissolution of the portlandite. On the other hand, the dissolution of the calcite from the Ca400ºC particles did not modify the pH. From these results, we chose a thermal treatment between 300 and 500 ºC to achieve particles with controlled sustained degradability able to release angiogenic Ca^{2+} concentrations over time without significant pH modifications. We discarded the particles treated below 300 ºC as a biological Ca^{2+} source due to the high increase in the pH.

4.3.3. Human dermal fibroblasts (hDFs) viability

The goal in this Chapter was to improve wound healing through the stimulation of vascularization promoted by angiogenic Ca^{2+} concentrations. Since the Ca400ºC particles could maintain significant high Ca^{2+} concentrations over time without pH modifications, we used these particles for the next biological experiments. Human dermal fibroblasts (hDFs) are in charge of maintenance and remodeling of the skin and have a primordial role in would healing [37]. For this reason, we tested the viability of hDFs with extractions of culture media (ECM) in contact with the Ca400ºC particles (Figure 7). The live/dead cell assay (Figure 7A) showed a high amount of alive hDFs (green) with a well-spread morphology after 1 day of culture with the ECM from the Ca400ºC particles. The absence of dead cells (red) indicates that the dissolution of the Ca400ºC particles did not have any cytotoxic effect on hDFs. The results were similar than a positive control of culture media (CM) supplemented with 1 mM of $CaCl_2$, thus validating the biocompatibility of the dissolution of the Ca400ºC particles. We did not observe significant changes in the color of the Ca400ºC ECM indicating pH neutrality (data not shown). We also measured the metabolic activity of the hDFs (Figure 7B). This time, we identified a higher metabolic activity for the hDFs cultured with the ECM in comparison to the 1 mM $CaCl_2$ culture media. This higher metabolic activity suggests a higher number of cells do to a higher cell survival or proliferation promoted by the dissolution of the Ca400ºC particles. Surprisingly, we observed that the Ca^{2+} concentration of the Ca400ºC particles in culture media (Figure 7C) was much lower than the one observed in HEPES solution (Figure 6B). In fact, it has been reported the insolubility of $CaCO_3$ in cell culture conditions [38]. As we stated in Chapter 3, section 3.3.2., we attributed this insolubility to the high $CO_{2(g)}$ levels of the incubator and the presence of HCO_3^- in the media. However, we must consider that such $CO_{2(g)}/HCO_3^-{}_{(aq)}$ levels may be reduced *in vivo* allowing the dissolution of the particles [39]. Moreover, $CaCO_3$ solubility highly increases in slightly acidic environments such as those found in healing wounds [4]. We

considered these reasons as a potential likely cause to expect the dissolution of the particles *in vivo*. Therefore, we decided to check their angiogenic and wound healing capacities in such conditions (see next sections).

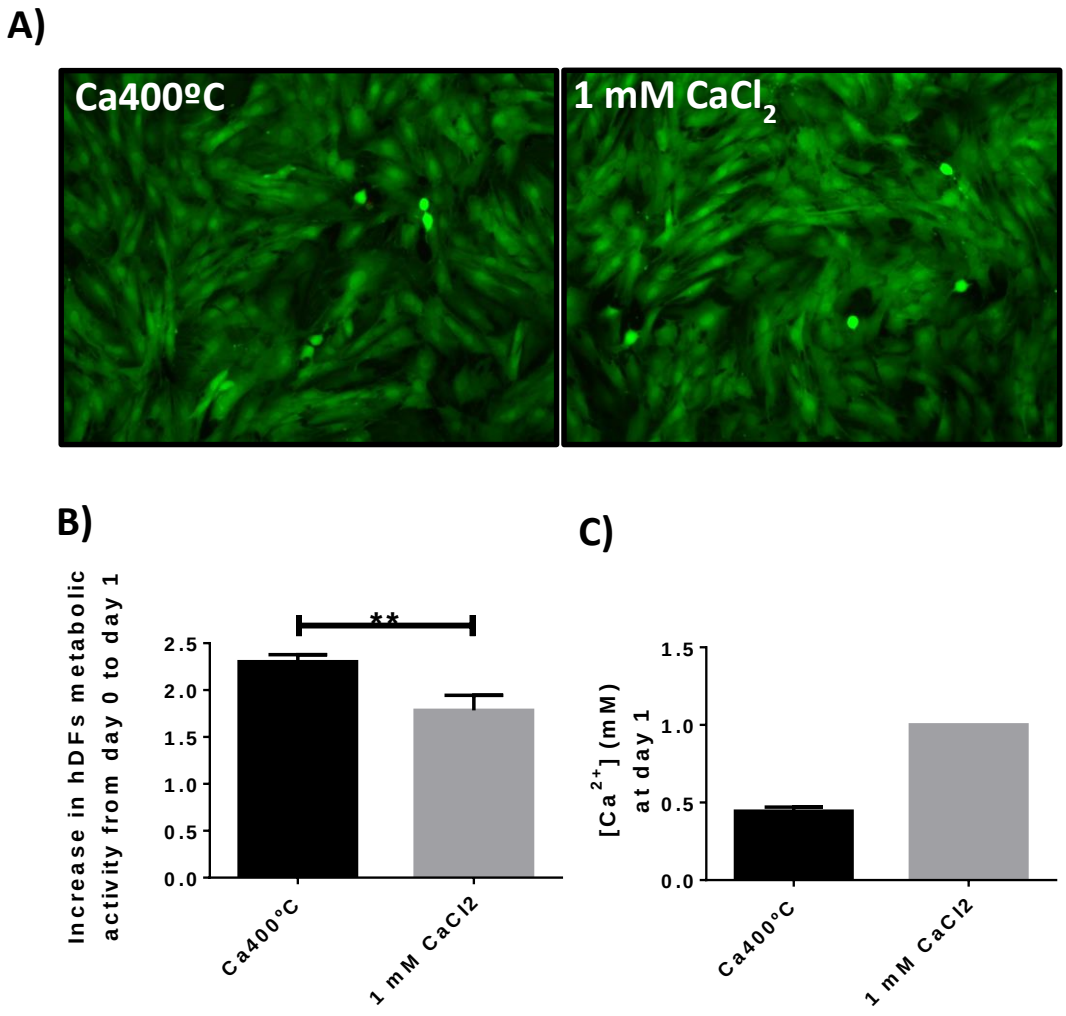

Figure 7. Live/dead staining **A)** and metabolic activity **B)** of hDFs cultured for 1 day with ECM form the Ca400ºC particles or 1mM $CaCl_2$ CM. Ca^{2+} concentration of the different media **C)**.

4.3.4. Formation of blood vessels in the CAM model

We implanted the Ca400ºC particles in the chick choriallantoic membrane (CAM) model and we compared the amount of small blood vessels with a negative control (NC) and a positive VEGF-loaded angiogenic condition, after 3 days of implantation (Figure 8). The *ex-ovo* CAM model is widely used as a preliminary angiogenic test since the direct exposure of blood vessels facilitates their quantification [19]. We evaluated the angiogenic properties of the Ca400ºC particles because the success of healing ischemic wounds mainly rely on the capacity to restore a proper vascularization [5]. Selected images of the different conditions (Figure 8) qualitatively showed a significant higher density of small blood vessels for the Ca400ºC particles and the positive VEGF-loaded control than for the NC. We quantified the area occupied by the small blood vessels using an improved version of the ImageJ macro used in Chapter 3, section 3.3.8. that basically simplified the process of image analysis (Figure 9). We also eliminated the nylon net artifact pattern (see section 4.2.4.2.) from the images by doing a color deconvolution with ImageJ. We found a statistical higher amount of blood vessels due to the presence of the Ca400ºC particles (Figure 8B). The absence of statistical differences with the positive VEGF-loaded control indicates that the Ca400ºC particles had a similar effect than angiogenic VEGF doses. Although the use of angiogenic factors has demonstrated to be effective in the formation of blood vessels, it also implies sever risks, storage difficulties and a high money-cost [15]. These results highlight that the particles could reduce or even substitute the use of angiogenic VEGF doses and avoid these limitations. We did not observe statistical differences between the two Ca400ºC particles loads indicating the requirement of significant small concentrations (for instance a 0.5% w/w) to reach their maximum angiogenic effects.

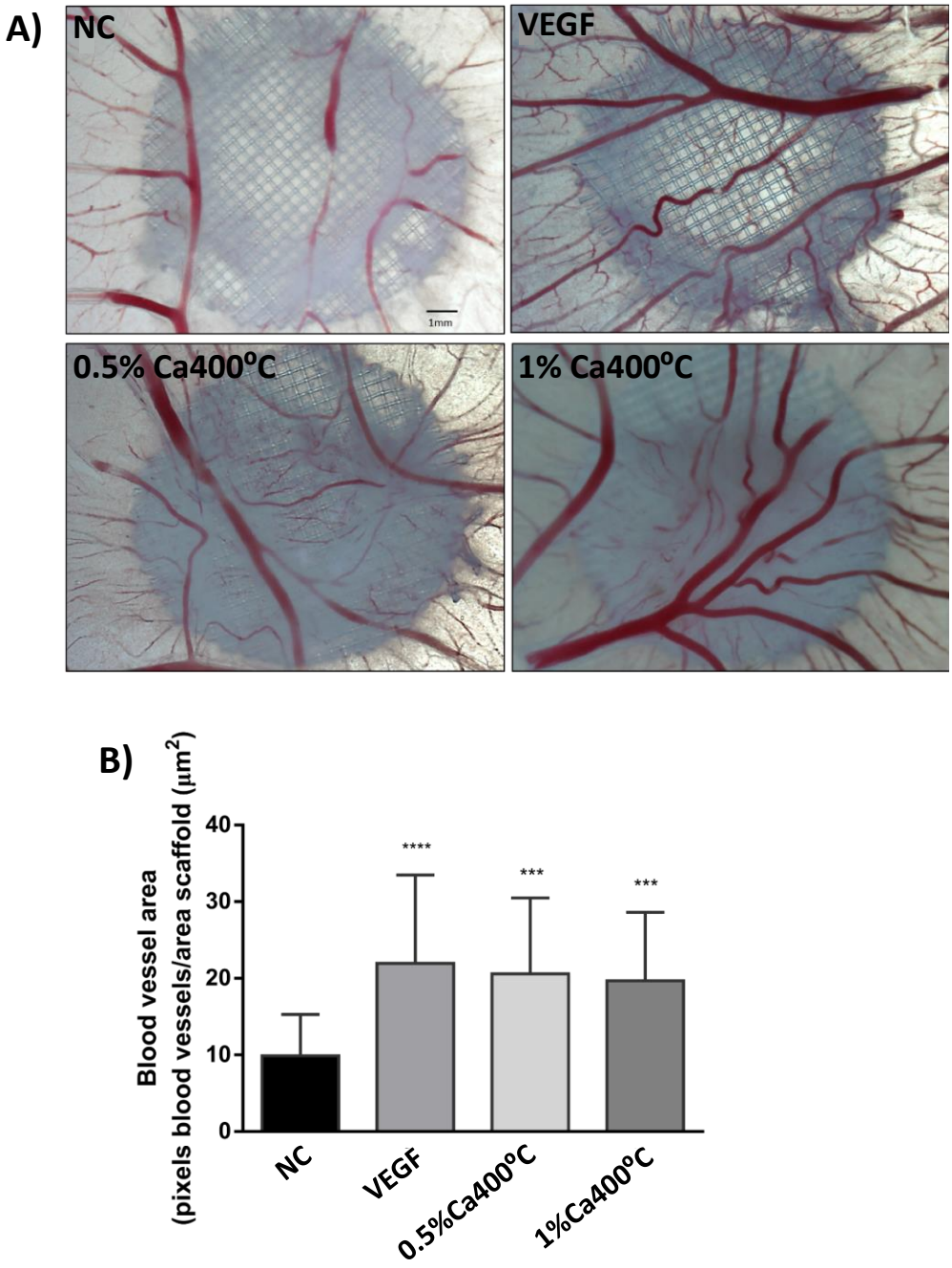

Figure 8. Selected images of the different conditions in the CAM model **A)**. Quantification of the small blood vessels/scaffold area using an own developed ImageJ macro (Figure 9) **B)**.

```
waitForUser("Select your scaffold");
run("Cut");
newImage("Untitled", "8-bit black", 2070, 1548, 1);
run("Paste");
run("Set Scale...", "distance=948 known=50 pixel=1 unit=mm");
run("Measure");
run("Set Scale...", "distance=0 known=0 pixel=1 unit=pixel");
selectWindow("Untitled");
run("Invert");
run("Subtract Background...", "rolling=10");
run("Auto Threshold", "method=Moments white");
run("Duplicate...", " ");
run("Canvas Size...", "width=2070 height=1548 position=Center zero");
run("Gray Morphology", "radius=6 type=circle operator=open");
setOption("BlackBackground", false);
run("Erode");
imageCalculator("Subtract create", "Untitled", "Untitled-1");
run("Invert");
run("Analyze Particles...", "exclude include summarize add");
```

Figure 9. Improved ImageJ macro used to quantify the density of small blood vessels in the CAM model (Figure 8). Before running the macro, we applied a color deconvolution (Image > Color > Color deconvolution>Vectors > From ROI) with the ImageJ software to eliminate the nylon net background (see images form Figure 8A) and quantify only the blood vessels. Macro developed by Irene Cano Torres (PhD candidate in the same research group) with the help of Dr. Lídia Bardia form the Advanced Digital Microscopy department at the Institute for Research in Biomedicine (IRB). For more information about the macro parameters please refer to Chapter 3, Figure 14.

It is difficult to correlate the observed angiogenic results with a release of Ca^{2+} since we could not measure the Ca^{2+} concentration in the CAM model. Remember that the Ca400ºC particles were practically insoluble under cell culture conditions (section 4.3.3.). However, the CAM conditions implied a normal atmospheric $CO_{2(g)}$ level (~0.04 %) much lower than the 5% used in the cell incubator. Furthermore, the collagen type I solution (section 4.2.4.2.) used to implant the particles did not contain HCO_3^-. Since we attributed

these two parameters to be determinant in the insolubility of the Ca400ºC particles [38], we assumed similar Ca^{2+} release rates than in the HEPES buffered medium (Figure 6A). Therefore, we consider the release of significant amounts of Ca^{2+} by the Ca400ºC particles as a potential likely cause of the observed angiogenic improvements.

4.3.5. Wound healing capacity in obese and diabetic mice

The absence of cytotoxicity with hDFS (Figure 7) and the angiogenic improvements in the CAM model (Figure 8) suggested that the Ca400ºC particles had a promising potential to treat ischemic wounds [5]. Therefore, we decided to evaluate their wound healing capacities in generated skin pressure ulcers in obese and diabetic mice. The use of the right animal models (e.g. diabetic and obese animals) is of paramount important since complications arise due to the alteration of the normal skin healing mechanisms in comparison to healthy subjects [2]. We generated ischemic pressure ulcers in the mice back skin by applying a widely used magnet-reperfusion method (section 4.2.4.3.1.) [23–25]. In order to have an implantable dressing that could be easily replaced every day, we electrospun the Ca400ºC particles in PLA nanofibers. FE-SEM images of the dressings (Figure 10) showed random distributed PLA fibers of 2-1 µm of diameter with Ca400ºC particles aggregates of ~1 µm embedded inside. The proper packaging of the particles inside the fibers suggests a good attractive interaction polymer-particles surface, that we attributed to the positive Z-potential of the particles and the negative charge of the PLA (Figure 5B) [35,36].

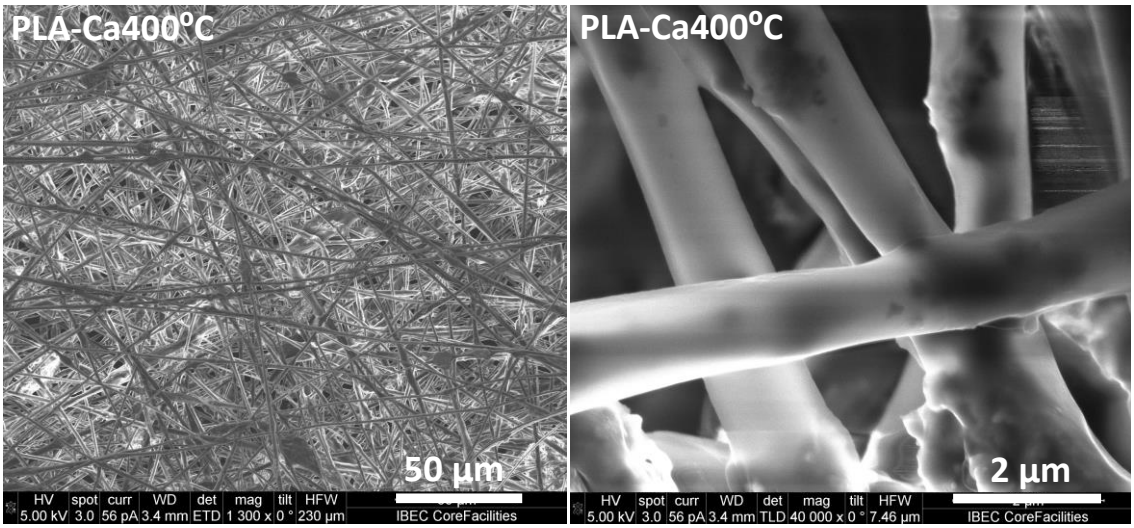

Figure 10. FE-SEM images of the PLA nanofiber dressings containing a 40% (w/w) of the Ca400ºC particles. We used the same FE-SEM conditions than in section 4.2.3.6..

For this study, we decided to decrease de load of particles to a 40% in comparison to the ≥60% used in Chapter 3 section 3.2.3., and therefore achieve higher mechanical properties that withstand better the mechanical stress associated to the mice daily live and further porcine model (see section 4.3.6.). The tensile-strain tests (Figure 11A, Table 1) showed that a 40% of the Ca400ºC particles slightly increased the stiffness (E) of the PLA nanofibers, while maintaining a similar ultimate strength (σ_{max}) and a lower but still high strain to failure (ε_{max}). The improvement in the mechanical properties in comparison to the PLA+P30 and PLA+P30+P55 scaffolds in Chapter 3 Figure 5A was attributed to a significant reduction (from ≥60% to a 40%) of the load of particles, suggesting a 40% to be more suitable to withstand the mechanical stress associated to the implantation process. However, the positive Z-potential of the Ca400ºC particles (Figure 5B) may have also contributed to maintain the mechanical properties of the PLA nanofibers by reinforcing the electrostatic interaction between the polymer (negatively charged) and the particles.

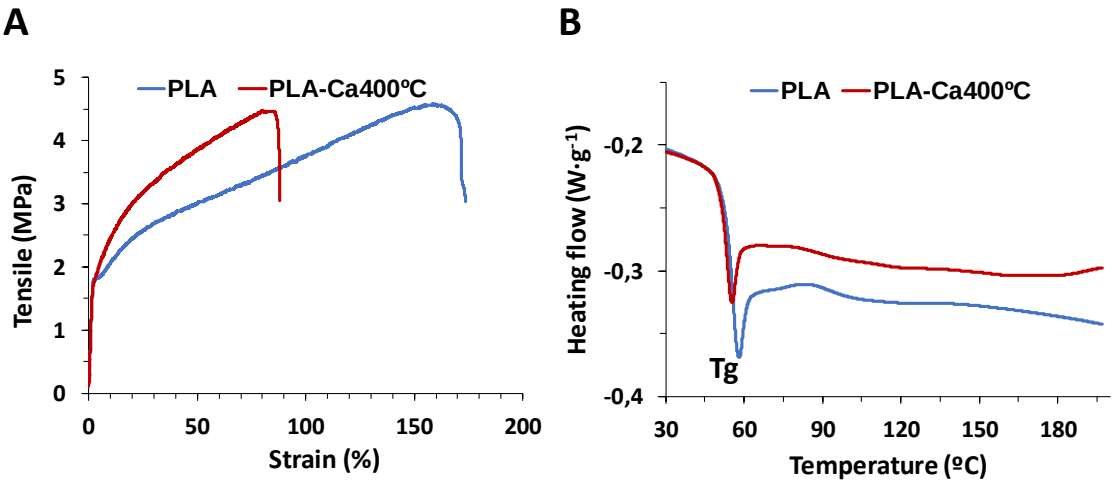

Figure 11. Tensile-strain tests **A)** and differential scanning calorimetry (DSC) **B)** of PLA and PLA-Ca400ºC dressings.

Table 1. Young's modulus (E), ultimate strength (σ_{Max}), strain to failure (ε_{Max}) and PLA glass transition temperature (Tg) of PLA and PLA-Ca400ºC dressings.

	E (Mpa)	σ_{Max} (Mpa)	ε_{Max} (%)	T_g (ºC)
PLA	93.4±2.46	4.56±0.27	172.4±8.6	57.8
PLA-Ca400ºC	110.1±6.9	4.19±0.29	94.1±5.7	49.3

On the other hand, the DSC results (Figure 11B, Table 1) showed a decrease in the PLA glass transition temperature (Tg) due to the presence of the Ca400ºC particles. We attributed this decrease to a possible partial degradation, and therefore a shortening of the PLA molecular chains, during the electrospinning process. Remember that the Ca400ºC particles contained a small proportion of portlandite (Figure 1A), which might have increased the pH in the preparation of the PLA solution prior to the electrospinning process. The partial shortening of the PLA molecules may have also contributed in the observed mechanical changes in Figure 11A. We did not observe any crystallization

temperature (Figure 11B), indicating that the PLA in the PLA-Ca400ºC dressings was completely amorphous even though the partial shortening of the PLA molecules.

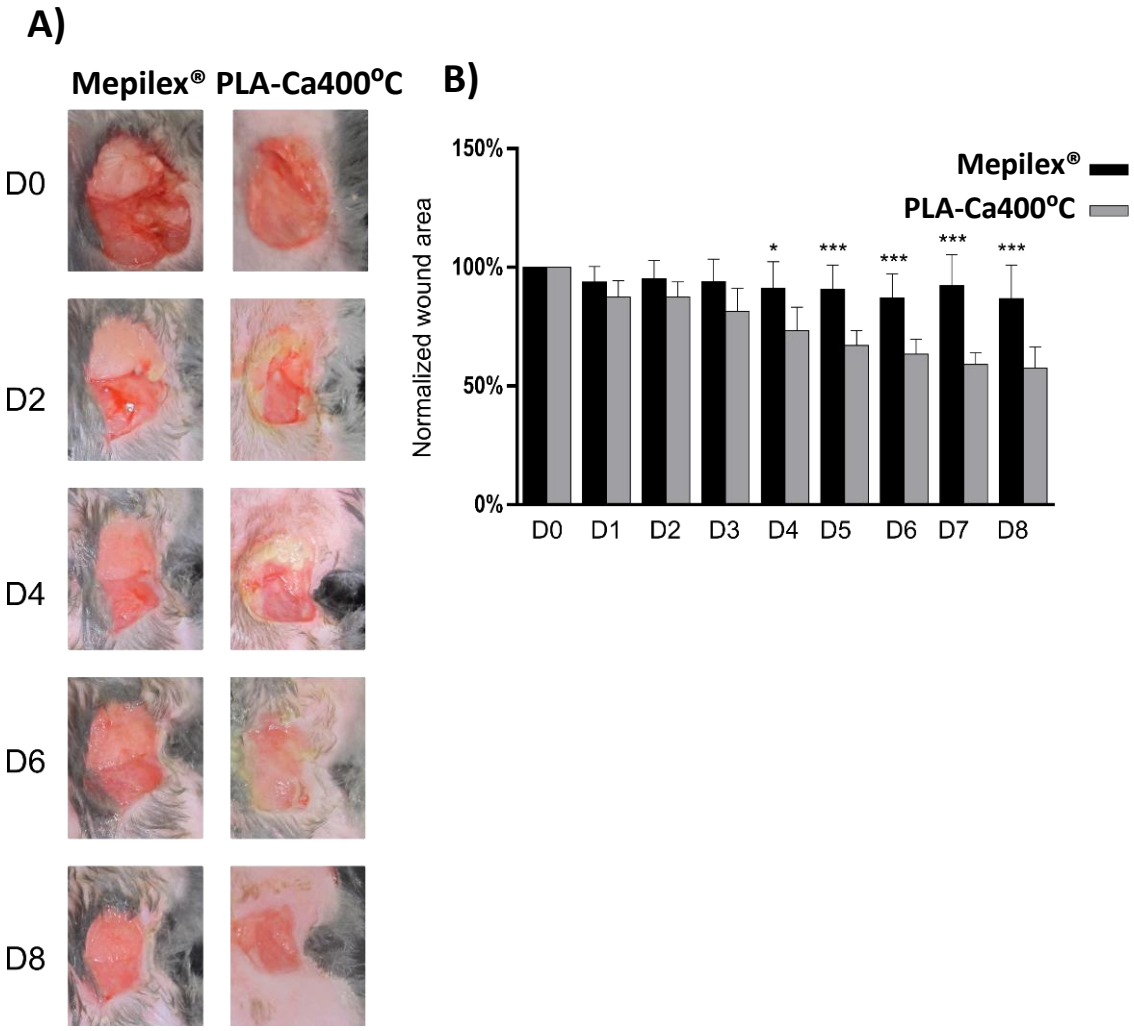

Figure 12. Selected images of the mice pressure ulcers treated with the Mepilex® and PLA-Ca400ºC dressings at different timepoints **A)**. Quantification of the wound area at different timepoints **B)**.

We implanted the PLA-Ca400ºC dressings in the generated pressure ulcers and quantified the wound area reduction over time. We compared the results with Mepilex® positive control dressings already used in the clinics to treat this type of wounds [26,27]. Selected images of the wounds (Figure 12A) qualitatively showed a significant smaller

size when treated with the PLA-Ca400ºC dressings than with the Mepilex® at list at day 7 and 8. We quantified a significant wound reduction (Figure 12B) for the PLACa400ºC dressings from day 1 to day 7, while the Mepilex® did not show wound reduction at any time point. The differences started to be statistically significant at day 4. These results are very promising since we demonstrate that our dressings reduced the wound area to almost a 50% in only 7 days, while the commercially available Mepilex® had no significant effects in the wound reduction of diabetic and obese mice at such short times. Zhang & Xing [26] reported that Mepilex® effectively reduced human diabetic foot ulcers at significant longer times (median 49.9 days). Although the skin healing mechanism of mice cannot be extrapolated to those from humans, which is expected to be much slower [2], our results suggest a quicker recovering using the developed Ca^{2+} releasing dressings.

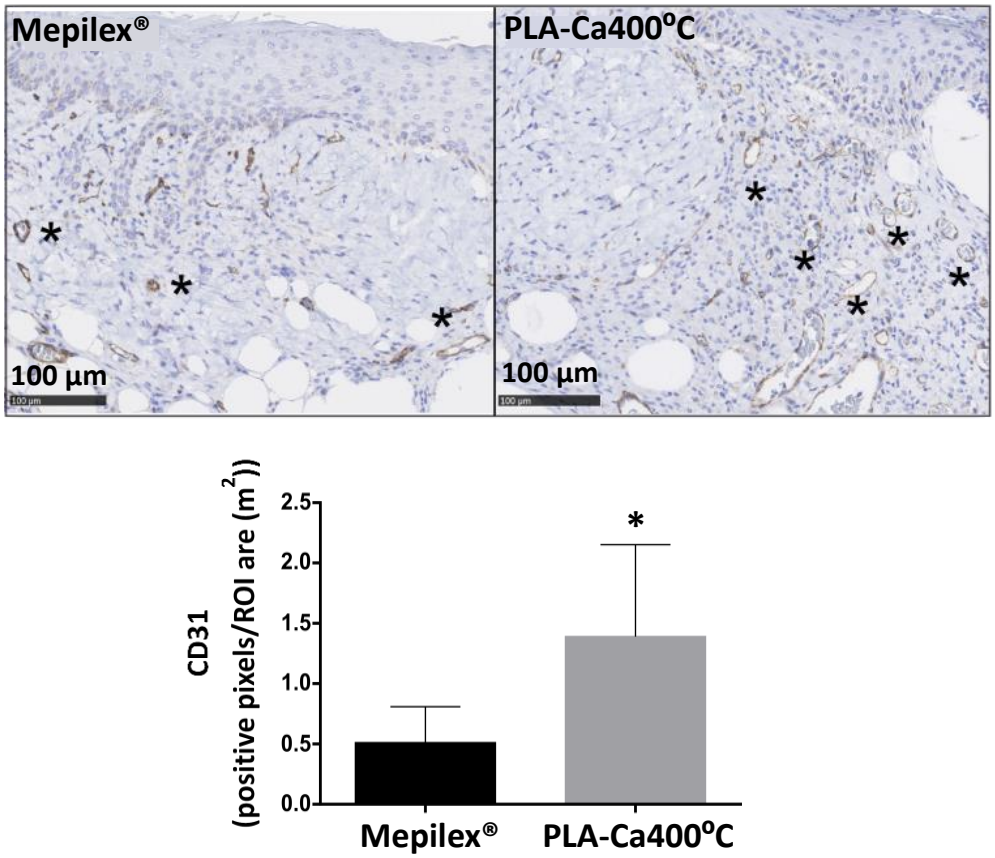

Figure 13. CD31 immunochemistry quantification of the mice wounds at day 8. Stars in the images point blood vessels.

Neovascularization is a key process for the successful healing of wounds. For this reason, we analyzed the amount of blood vessels immunolabelled against cluster of differentiation (CD31) from histological sections of the wounds at day 8 (Figure 13). CD31 also known as platelet endothelial cell adhesion molecule (PECAM-1) is a protein found in endothelial intercellular junctions. Since it is present in blood vessels it is very useful to evaluate the degree of angiogenesis from tissues [9,12,40]. The results (Figure 13) showed a higher vascularization in the dermis and hypodermis of the wounds treated with the PLA-Ca400ºC dressings than with the Mepilex® control, suggesting that the improvements in wound healing were promoted by an increase in vascularization, which is consistent with the assumption that the Ca^{2+} releasing gradients stimulated the formation of blood vessels.

4.3.6. Preliminary *in vivo* experiment in a porcine skin model

We would like to add to this chapter a brief paragraph mentioning a preliminary *in vivo* experiment using the PLA-Ca400ºC dressings in generated skin wounds (2x5 cm^2) in a porcine model. Although we only used one pig with two replicates per condition, we found appropriate to add these results due to its relevance. Interestingly, the results showed a significant reduction for the wounds treated with the PLA-Ca400ºC dressings regarding the absence of dressings (Table 2). The porcine model is very close to the human skin healing conditions and hence it is a very confident method to test the wound healing capacities of different developed therapies [41,42]. Further experiments in diabetic-induced pigs are ongoing in order to have better reproducibility and more accurate results.

Table 2. Wound % reduction of generated skin wounds in a porcine model untreated and treated with the PLA-Ca400ºC dressings. Experiment performed by the Pharmacology, Therapeutics and Toxicology department at the Universitat Autonòma de Barcelona (UAB).

	4 days	8 days	12 days	18 days	22 days
No dressing	-13.9	30.6	53.0	75.0	85.0
No dressing	-8.3	20.6	65.0	78.9	87.2
PLA-Ca400ºC	-17.2	41.1	74.4	85.6	94.4
PLA-Ca400ºC	-20.0	36.1	65.0	90.0	95.6

4.4. Conclusions

We achieved highly degradable nanoparticles whose Ca^{2+} release was sustained and could be tuned by applying different thermal treatments. Such particles only released Ca^{2+} avoiding a possible mineralization of the wound site induced by the release of other ions like PO_4^{3-}. Particle characterization showed the formation of nanocrystalline portlandite and suggested that the control over degradability consisted on the degree of conversion of the portlandite to calcite after the different thermal treatments. The sustained degradation of the Ca400ºC particles did not show cytotoxicity with hDFs or pH modifications, and induced a similar angiogenic response than significant VEGF doses in the CAM model. The implantation of PLA electrospun nanofiber dressings containing the particles in generated skin pressure ulcers in diabetic and obese mice showed a statistical faster wound reduction in comparison to conventional Mepilex®. Moreover, CD31 immunochemistry showed a higher vascularization induced by the PLA-Ca400ºC dressings. A preliminary evaluation (still under development) in a porcine model showed also a faster wound reduction for skin wounds treated with the PLA-Ca400ºC dressings in comparison to their absence. These results are very promising and suggest that the production of Ca^{2+} releasing dressings can be an efficient and cost-effective strategy to improve the current treatment of chronic skin wounds.

4.5. References

[1] S. Böttcher-Haberzeth, T. Biedermann, E. Reichmann, Tissue engineering of skin, Burns. 36 (2010) 450–460. doi:10.1016/j.burns.2009.08.016.

[2] N. Goonoo, A. Bhaw-Luximon, Analyzing polymeric nanofibrous scaffold performances in diabetic animal models for translational chronic wound healing research, Nanotechnol. Rev. 6 (2017) 583–600. doi:10.1515/ntrev-2017-0162.

[3] C. Pham, J. Greenwood, H. Cleland, P. Woodruff, G. Maddern, Bioengineered skin substitutes for the management of burns: A systematic review, Burns. 33 (2007) 946–957. doi:10.1016/j.burns.2007.03.020.

[4] S. Hampton, Understanding the pH balance in wound healing, J. Community Nurs. 22 (2008) 34–38.

[5] H. Chen, L. Guo, J. Wicks, C. Ling, X. Zhao, Y. Yan, J. Qi, W. Cui, L. Deng, Quickly promoting angiogenesis by using a DFO-loaded photo-crosslinked gelatin hydrogel for diabetic skin regeneration, J. Mater. Chem. B. 4 (2016) 3770–3781. doi:10.1039/C6TB00065G.

[6] A. Siebert, I. Goren, J. Pfeilschifter, S. Frank, Anti-inflammatory effects of rosiglitazone in obesity-impaired wound healing depend on adipocyte differentiation, PLoS One. 11 (2016) 1–25. doi:10.1371/journal.pone.0168562.

[7] C. Navarro-Requena, J.D. Weaver, A.Y. Clark, D.A. Clift, S. Pérez-Amodio, Ó. Castaño, D.W. Zhou, A.J. García, E. Engel, PEG hydrogel containing calcium-releasing particles and mesenchymal stromal cells promote vessel maturation, Acta Biomater. (2017). doi:10.1016/j.actbio.2017.12.009.

[8] O.C. Velazquez, Angiogenesis & Vasculogenesis: Inducing the growth of new blood vessels and wound healing by stimulation of Bone Marrow Derived

Progenitor Cell Mobilization and Homing, J Vasc Surg. 45 (2007) 39–47. doi:10.1016/j.jvs.2007.02.068.

[9] X. Ren, Y. Han, J. Wang, Y. Jiang, Z. Yi, H. Xu, Q. Ke, An aligned porous electrospun fibrous membrane with controlled drug delivery – An efficient strategy to accelerate diabetic wound healing with improved angiogenesis, Acta Biomater. 70 (2018) 140–153. doi:10.1016/j.actbio.2018.02.010.

[10] A. Aguirre, A. González, M. Navarro, Ó. Castaño, J.A. Planell, E. Engel, Control of microenvironmental cues with a smart biomaterial composite promotes endothelial progenitor cell angiogenesis, Eur. Cells Mater. 24 (2012) 90–106. doi:10.22203/eCM.v024a07.

[11] A. González-Vázquez, J.A. Planell, E. Engel, Extracellular calcium and CaSR drive osteoinduction in mesenchymal stromal cells, Acta Biomater. 10. 10 (2014) 2824–2833. doi:10.1016/j.actbio.2014.02.004.

[12] H. Oliveira, S. Catros, C. Boiziau, R. Siadous, J. Marti-Munoz, R. Bareille, S. Rey, O. Castano, J. Planell, J. Amédée, E. Engel, The proangiogenic potential of a novel calcium releasing biomaterial: Impact on cell recruitment, Acta Biomater. 29 (2016) 435–445. doi:10.1016/j.actbio.2015.10.003.

[13] H. Oliveira, S. Catros, O. Castano, S. Rey, R. Siadous, D. Clift, J. Marti-Munoz, M. Batista, R. Bareille, J.A. Planell, E. Engel, The proangiogenic potential of a novel calcium releasing composite biomaterial : Orthotopic in vivo evaluation, Acta Biomater. 54 (2017) 377–385. doi:10.1016/j.actbio.2017.02.039.

[14] N. Sachot, O. Castaño, H. Oliveira, J. Martí-Muñoz, A. Roguska, J. Amedee, M. Lewandowska, J.A. Planell, E. Engel, A novel hybrid nanofibrous strategy to target progenitor cells for cost-effective in situ angiogenesis, J. Mater. Chem. B. 4 (2016) 6967–6978. doi:10.1039/C6TB02162J.

[15] A. Malhotra, P. Habibovic, Calcium Phosphates and Angiogenesis: Implications and Advances for Bone Regeneration, Trends Biotechnol. 34 (2016) 983–992. doi:10.1016/j.tibtech.2016.07.005.

[16] Advanced Chemistry Development (ACD), Inc., Toronto, ON, Canada, 2017, (n.d.). http://www.acdlabs.com/.

[17] H.J. Gitelman, An improved automated procedure for the determination of calcium in biological specimens, Anal. Biochem. 18 (1967) 521–531. doi:10.1016/0003-2697(67)90110-8.

[18] E. Gindler, J. King, Rapid colorimetric determination of calcium in biologic fluids with methylthymol blue, Am. J. Clin. Pathol. 58 (1972) 376–382. doi:10.1093/ajcp/58.5.376.

[19] E.I. Deryugina, J.P. Quigley, CHAPTER TWO: Chick Embryo Chorioallantoic Membrane Models to Quantify Angiogenesis Induced by Inflammatory and Tumor Cells or Purified Effector Molecules, Methods Enzym. 444 (2009) 21–41. doi:10.1016/S0076-6879(08)02802-4.

[20] N. Kanda, S. Watanabe, Regulatory roles of sex hormones in cutaneous biology and immunology, J. Dermatol. Sci. 38 (2005) 1–7. doi:10.1016/j.jdermsci.2004.10.011.

[21] S.C. Gilliver, F. Wu, G.S. Ashcroft, Regulatory roles of androgens in cutaneous wound healing, Thromb. Haemost. 90 (2003) 978–985. doi:10.1160/TH-03-05-0302.

[22] S.C. Gilliver, E. Emmerson, J. Bernhagen, M.J. Hardman, MIF: A key player in cutaneous biology and wound healing, Exp. Dermatol. 20 (2011) 1–6. doi:10.1111/j.1600-0625.2010.01194.x.

[23] I. Stadler, R.Y. Zhang, P. Oskoui, M.S. Whittaker, R.J. Lanzafame, Development

of a simple, noninvasive, clinically relevant model of pressure ulcers in the mouse, J. Investig. Surg. 17 (2004) 221–227. doi:10.1080/08941930490472046.

[24] Y. Saito, M. Hasegawa, M. Fujimoto, T. Matsushita, M. Horikawa, M. Takenaka, F. Ogawa, J. Sugama, D.A. Steeber, S. Sato, K. Takehara, The loss of MCP-1 attenuates cutaneous ischemia-reperfusion injury in a mouse model of pressure ulcer, J. Invest. Dermatol. 128 (2008) 1838–1851. doi:10.1038/sj.jid.5701258.

[25] E. Wassermann, M. Van Griensven, K. Gstaltner, W. Oehlinger, K. Schrei, H. Redl, A chronic pressure ulcer model in the nude mouse, Wound Repair Regen. 17 (2009) 480–484. doi:10.1111/j.1524-475X.2009.00502.x.

[26] Y. Zhang, S.Z. Xing, Treatment of diabetic foot ulcers using Mepilex Lite dressings: A pilot study, Exp. Clin. Endocrinol. Diabetes. 122 (2014) 227–230. doi:10.1055/s-0034-1370918.

[27] G. Weaver, K. Crawford, The use of Mepilex on dehisced amputation wounds, Wounds UK. 3 (2007) 70–74.

[28] C. for C.R.& C. Biology, QuPath, (2018). https://qupath.github.io/.

[29] P. Scardi, M. Leoni, K.R. Beyerlein, On the modelling of the powder pattern from a nanocrystalline material, Zeitschrift Fur Krist. 226 (2011) 924–933. doi:10.1524/zkri.2011.1448.

[30] G. Montes-Hernandez, D. Daval, N. Findling, R. Chiriac, F. Renard, Linear growth rate of nanosized calcite synthesized via gas-solid carbonation of Ca(OH)2 particles in a static bed reactor, Chem. Eng. J. 180 (2012) 237–244. doi:10.1016/j.cej.2011.11.020.

[31] M. Galván-Ruiz, J. Hernández, L. Baños, J. Noriega-Montes, M.E. Rodríguez-García, Characterization of Calcium Carbonate, Calcium Oxide, and Calcium Hydroxide as Starting Point to the Improvement of Lime for Their Use in

Construction, J. Mater. Civ. Eng. 21 (2009) 694–698. doi:10.1061/(ASCE)0899-1561(2009)21:11(694).

[32] A.M. Kalinkin, E. V Kalinkina, O.A. Zalkind, T.I. Makarova, Chemical Interaction of Calcium Oxide and Calcium Hydroxide with CO2 during Mechanical Activation, Inorg. Mater. 41 (2005) 1073–1079. doi:10.1007/s10789-005-0263-1.

[33] R.W. O'Brien, B.R. Midmore, A. Lamb, R.J. Hunter, Electroacoustic studies of moderately concentrated colloidal suspensions, Faraday Discuss. Chem. Soc. 90 (1990) 301–312. doi:10.1039/dc9909000301.

[34] D. Hanaor, M. Michelazzi, C. Leonelli, C.C. Sorrell, The effects of carboxylic acids on the aqueous dispersion and electrophoretic deposition of ZrO2, J. Eur. Ceram. Soc. 32 (2012) 235–244. doi:10.1016/j.jeurceramsoc.2011.08.015.

[35] E. Sánchez-López, M. Ettcheto, M.A. Egea, M. Espina, A. Cano, A.C. Calpena, A. Camins, N. Carmona, A.M. Silva, E.B. Souto, M.L. García, Memantine loaded PLGA PEGylated nanoparticles for Alzheimer's disease: In vitro and in vivo characterization, J. Nanobiotechnology. 16 (2018) 1–16. doi:10.1186/s12951-018-0356-z.

[36] B. Tang, J.L. Zaro, Y. Shen, Q. Chen, Y. Yu, P. Sun, Y. Wang, W.C. Shen, J. Tu, C. Sun, Acid-sensitive hybrid polymeric micelles containing a reversibly activatable cell-penetrating peptide for tumor-specific cytoplasm targeting, J. Control. Release. 279 (2018) 147–156. doi:10.1016/j.jconrel.2018.04.016.

[37] R.R. Driskell, F.M. Watt, Understanding fibroblast heterogeneity in the skin, Trends Cell Biol. 25 (2015) 92–99. doi:10.1016/j.tcb.2014.10.001.

[38] C.B.S.S. Danoux, D.C. Bassett, Z. Othman, A.I. Rodrigues, R.L. Reis, J.E. Barralet, C.A. Van Blitterswijk, P. Habibovic, Elucidating the individual effects of calcium and phosphate ions on hMSCs by using composite materials, Acta

Biomater. 17 (2015) 1–15. doi:10.1016/j.actbio.2015.02.003.

[39] T. Hickish, A.D. Farmery, Acid-base physiology : new concepts, Anaesth. Intensive Care Med. 13 (2012) 567–572. doi:10.1016/j.mpaic.2012.09.003.

[40] T. Shimo, T. Nakanishi, T. Nishida, M. Asano, M. Kanyama, T. Kuboki, T. Tamatani, K. Tezuka, M. Takemura, T. Matsumura, M. Takigawa, Connective Tissue Growth Factor Induces the Proliferation, Migration, and Tube Formation of Vascular Endothelial Cells In Vitro, and Angiogenesis In Vivo, J. Biochem. 126 (1999) 137–145. doi:10.1093/oxfordjournals.jbchem.a022414.

[41] T.P. Sullivan, W.H. Eaglstein, S.C. Davis, P. Mertz, The pig as a model for human wound healing, Wound Repair Regen. 9 (2001) 66–76. doi:10.1046/j.1524-475x.2001.00066.x.

[42] M. Seaton, A. Hocking, N.S. Gibran, Porcine models of cutaneous wound healing, ILAR J. 56 (2015) 127–138. doi:10.1093/ilar/ilv016.

General conclusions

Following the hypothesis that the release of specific Ca^{2+} concentrations in the body will stimulate the formation of blood vessels, we developed a system that modulated the bioactive release of Ca^{2+} for biointegrative purposes. Such system consisted of the sol-gel synthesis of binary (P_2O_5:CaO) calcium phosphate glasses (CPg) in the form of nanoparticles. We used calcium 2-methoxyethoxide and mono/diethylphosphate as sol-gel precursors and we controlled the ion release of the particles by modifying their Ca/P ratio and applying moderately low thermal treatments. We characterized by NMR spectroscopy and other complementary techniques the formation of amorphous calcium MEP (CMEP) for the particles before thermal treatment, with the formation of portlandite or $NH_4H_2PO_4$ when there was an excess or the absence of Ca respectively. After thermal treatment, the organic CMEP was converted into inorganic ACTMP, ACPP, ACP and calcite as the Ca content increase respectively. The solubility of the particles before thermal treatment was very high releasing high amounts of Ca^{2+} and MEP in short periods without significant pH modifications. After thermal treatment, the degradability of the particles was sustained, releasing for more than two weeks, substantial amounts of Ca^{2+} and Pi without significant pH modifications. To date, there are not studies about binary CPg synthesized by the sol-gel method, whose advantages, regarding more complex CPg systems (e.g. ternary, quaternary systems), include a straightforward synthesis and the absence of extra ions (e.g. SiO_4^{4-}, Ti^{4+}) with unknown metabolization. We used some of the particles to achieve fast or sustained Ca^{2+} releases *in vitro*. We combined the particles with electrospun polylactic acid (PLA) nanofibers as a platform for implantable scaffolds that mimicked the morphology of the natural extracellular matrix. The scaffolds induced several angiogenic responses including a higher VEGF synthesis by hMSCs and a similar formation of blood vessels in the CAM model than angiogenic VEGF doses. The simultaneous release of inorganic phosphate (Pi) by the

particles had positive results in the mineralization and osteogenic differentiation of hMSCs, suggesting a high potential for bone regenerative applications. Parallelly, we used some of the particles to treat chronic skin wounds. Such approach has been protected by means of patent (Ref. N. PCT/EP2018/064378). This time, we prescinded from the Pi to avoid mineralization in the wound site. We observed that the pure Ca^{2+} releasing nanoparticles combined with PLA nanofiber dressings induced a higher blood vessel formation and a significant faster wound reduction in the skin of diabetic and obese mice than standard Mepilex® already used in the clinics. These results highlight the use Ca^{2+} releasing dressings as an alternative to the current inefficient chronic skin wounds therapies. Concluding, we developed in this thesis an easygoing system that induced a proper angiogenic response for tissue regeneration that could minimize the use of more sophisticated, expensive and risky strategies like cell therapy or the implantation of growth factors.

Future work

A small size and a proper dispersion of the particle filler in a polymer composite is essential for a good distribution of properties. The described CPg synthesis method in Chapter 2 resulted in the agglomeration of nanoparticles into bigger microaggregates of different sizes. A novel sol-gel synthesis method combining an electrospray technique has shown to minimize nanoparticle aggregation, resulting in the synthesis of well-dispersed CPg nanoparticles with a homogeneous size distribution [1]. This method consists of electrospraying the sol-gel precursors in a heated silicon bath. The bath high temperature (up to 200 ºC) induces the immediate condensation of the precursors into solid inorganic nanoparticles. The direct obtention of inorganic nanoparticles minimizes aggregation and simplifies the method of synthesis. Moreover, the silicon bath may act as a repellent of electrostatic interactions. Modification of parameters like the sol-gel precursors concentration suggests a control over the particles size. This method could be easily adapted to the CPg formulation presented in this thesis and would simplify the obtention of inorganic nanoparticles. However, lower temperature baths should be used for the obtention of the organically modified CPg nanoparticles with higher degradability.

Another parameter affecting in the properties (e.g. mechanical) distribution in a composite is the interaction between the filler and the polymer matrix. One of the strongest interactions in chemistry is the covalent bonding. Modification of the CPg nanoparticle surface with certain molecules can introduce specific functional groups that can be used for covalent attachment with biocompatible polymers. For instance, as we demonstrated in previous studies [2], the primary amine groups introduced by the functionalization of CPg nanoparticles with APTES were linked to the EDC/NHS activated carboxylate groups of the PLA. The covalent interaction between polymer and filler would improve the mechanical resistance of the developed scaffolds and minimize particle detachment after implantation.

A different advantage of introducing primary amines in the CPg nanoparticles is their functionalization with active molecules like proteins, peptides, polysaccharides, etc. Although the use of such molecules can difficult their translation to the market due to strict regulations and problems on overdoses, a proper combination of synthetic and biological compounds, as well as, a better understanding of their biology is essential for the improvement of biomaterials. Biocompatible polymers have served as templates to introduce biological molecules, using the reactivity of different functional groups [3]. The APTES surface modified CPg nanoparticles will allow their functionalization with active molecules [4], translating their use to a wide range of applications such as the delivery of growth factors, reduction of inflammatory responses, specific body recognition, DNA vectors, etc. On the other hand, doping of the CPg nanoparticles with different ions (e.g. Cu^{2+}, Zn^{2+}, Co^{2+}, Ag^{+}) is another alternative to introduce specific bioactivity such as antimicrobial properties or a higher angiogenesis. This approach would avoid the strict regulations related to biological molecules. However, some of these ions may induce cytotoxicity at moderately low doses, as well as, they can reduce the degradability of the particles.

The introduction of the CPg nanoparticles in other scaffolds apart from PLA electrospun nanofibers is also another path to explore. It has been demonstrated that the addition of CPg nanoparticles increased the survival of embedded hMSCs in a PEG hydrogel [5]. The introduction of the developed CPg nanoparticles in cell containing hydrogel like for example cross-linked hyaluronic acid could improve cell survival in cartilage regeneration applications.

Regarding Chapter 3, it is evident that the next logical step would be to perform *in vivo* experiments to check the osteogenic capacity of the developed scaffolds. A coherent experiment would be their implantation in rat condylar defects, as we did with similar scaffolds [6], obtaining positive results. On the other hand, further porcine experiments

need to be done with the developed scaffolds in Chapter 4, in other to have a better reproducibility in the obtained results and support the developed patent.

[1] F. Foroutan, J. V. Jokerst, S.S. Gambhir, O. Vermesh, H.W. Kim, J.C. Knowles, Sol-gel synthesis and electrospraying of biodegradable (P2O5)55-(CaO)30-(Na2O)15 glass nanospheres as a transient contrast agent for ultrasound stem cell imaging, ACS Nano. 9 (2015) 1868–1877. doi:10.1021/nn506789y.

[2] N. Sachot, M.A. Mateos-Timoneda, J.A. Planell, A.H. Velders, M. Lewandowska, E. Engel, O. Castaño, Towards 4th generation biomaterials: a covalent hybrid polymer–ormoglass architecture, Nanoscale. 7 (2015) 15349–15361. doi:10.1039/C5NR04275E.

[3] A. Monnier, E. Al Tawil, Q.T. Nguyen, J.M. Valleton, K. Fatyeyeva, B. Deschrevel, Functionalization of poly(lactic acid) scaffold surface by aminolysis and hyaluronan immobilization: How it affects mesenchymal stem cell proliferation, Eur. Polym. J. 107 (2018) 202–217. doi:10.1016/j.eurpolymj.2018.08.011.

[4] B. Acharya, S.Y. Chun, S.Y. Kim, C. Moon, H.I. Shin, E.K. Park, Surface immobilization of MEPE peptide onto HA/b-TCP ceramic particles enhances bone regeneration and remodeling, J. Biomed. Mater. Res. - Part B Appl. Biomater. 100 B (2012) 841–849. doi:10.1002/jbm.b.32648.

[5] C. Navarro-Requena, J.D. Weaver, A.Y. Clark, D.A. Clift, S. Pérez-Amodio, Ó. Castaño, D.W. Zhou, A.J. García, E. Engel, PEG hydrogel containing calcium-releasing particles and mesenchymal stromal cells promote vessel maturation, Acta Biomater. (2017). doi:10.1016/j.actbio.2017.12.009.

[6] H. Oliveira, S. Catros, O. Castano, S. Rey, R. Siadous, D. Clift, J. Marti-Munoz, M. Batista, R. Bareille, J.A. Planell, E. Engel, The proangiogenic potential of a novel calcium releasing composite biomaterial : Orthotopic in vivo evaluation, Acta Biomater. 54 (2017) 377–385. doi:10.1016/j.actbio.2017.02.039.